



**HAL**  
open science

# High Frequency MEMS Sensor for Aero-acoustic Measurements

Zhijian J. Zhou

► **To cite this version:**

Zhijian J. Zhou. High Frequency MEMS Sensor for Aero-acoustic Measurements. Micro and nanotechnologies/Microelectronics. Université de Grenoble, 2013. English. NNT: . tel-00838736

**HAL Id: tel-00838736**

**<https://theses.hal.science/tel-00838736>**

Submitted on 26 Jun 2013

**HAL** is a multi-disciplinary open access archive for the deposit and dissemination of scientific research documents, whether they are published or not. The documents may come from teaching and research institutions in France or abroad, or from public or private research centers.

L'archive ouverte pluridisciplinaire **HAL**, est destinée au dépôt et à la diffusion de documents scientifiques de niveau recherche, publiés ou non, émanant des établissements d'enseignement et de recherche français ou étrangers, des laboratoires publics ou privés.

## THÈSE

Pour obtenir le grade de

### DOCTEUR DE L'UNIVERSITÉ DE GRENOBLE

Spécialité : NANO ELECTRONIQUE NANO TECHNOLOGIES

Arrêté ministériel : 7 août 2006

Et de

### DOCTEUR DE THE HONG KONG UNIVERSITY OF SCIENCE AND TECHNOLOGY

Spécialité : ELECTRONIC AND COMPUTER ENGINEERING

Présentée par

«**Zhijian ZHOU**»

Thèse dirigée par «**Libor RUFER**» et  
codirigée par «**Man WONG**»

préparée au sein du **Laboratoire TIMA**  
dans l'**École Doctorale Electronique, Electrotechnique, Automatique et  
Traitement du Signal**  
et **Electronic and Computer Engineering Department**

# Microcapteurs de Hautes Fréquences pour des Mesures en Aéroacoustique

Thèse soutenue publiquement le «**01/21/2013**»,  
devant le jury composé de :

**M. David COOK**

Professeur Associé, Hong Kong University of Science & Technology, Président

**M. Philippe, BLANC-BENON**

Directeur de Recherche, CNRS, Ecole Centrale de Lyon, Rapporteur

**M. Philippe COMBETTE**

Professeur, Université Montpellier II, Rapporteur

**M. Skandar BASROUR**

Professeur, Université Joseph Fourier, Grenoble, Examineur

**Mme Wenjing YE**

Professeur Associé, Hong Kong University of Science & Technology, Examineur

**M. Levent YOBAS**

Professeur Assistant, Hong Kong University of Science & Technology, Examineur

**M. Man WONG**

Professeur, Hong Kong University of Science & Technology, Co-Directeur de thèse

**M. Libor RUFER**

Chercheur, Université Joseph Fourier, Grenoble, Directeur de thèse



# **High Frequency MEMS Sensor for Aero-acoustic Measurements**

By

**ZHOU, Zhijian**

A Thesis Submitted to

The Hong Kong University of Science and Technology

in Partial Fulfillment of the Requirements for

the Degree of Doctor of Philosophy

in the Department of Electronic and Computer Engineering

and

Université de Grenoble

in Partial Fulfillment of the Requirements for

the Degree of Docteur de l' Université de Grenoble

in the Ecole Doctorale Electronique, Electrotechnique, Automatique & Traitement du Signal

February 2013, Hong Kong

## **Authorization**

I hereby declare that I am the sole author of the thesis.

I authorize the Hong Kong University of Science and Technology and Université de Grenoble to lend this thesis to other institutions or individuals for the purpose of scholarly research.

I further authorize the Hong Kong University of Science and Technology and Université de Grenoble to reproduce the thesis by photocopying or by other means, in total or in part, at the request of other institutions or individuals for the purpose of scholarly research.

---

**ZHOU, Zhijian**

February 2013

# **High Frequency MEMS Sensor for Aero-acoustic Measurements**

By

**ZHOU, Zhijian**

This is to certify that I have examined the above Ph.D thesis and have found that it is complete and satisfactory in all respects, and that any and all revisions required by the thesis examination committee have been made.

---

Prof. Man WONG

Department of Electronic and Computer Engineering, HKUST, Hong Kong

Thesis Supervisor

---

Prof. Libor RUFER

Université de Grenoble, France

Thesis Co-Supervisor

---

Prof. David COOK

Department of Economics, HKUST, Hong Kong

Thesis Examination Committee Member (Chairman)

---

Prof. Skandar BASROUR

Université de Grenoble, Grenoble, France

Thesis Examination Committee Member

---

Prof. Wenjing YE

Department of Mechanical Engineering, HKUST, Hong Kong

Thesis Examination Committee Member

---

Prof. Levent YOBAS

Department of Electronic and Computer Engineering, HKUST, Hong Kong

Thesis Examination Committee Member

---

Prof. Ross MURCH

Department of Electronic and Computer Engineering, HKUST, Hong Kong

Department Head

Department of Electronic and Computer Engineering

The Hong Kong University of Science and Technology

February 2013

## Acknowledgments

I would like to give my deepest appreciation first and foremost to Professor Man WONG and Professor Libor RUFER, my supervisors, for their constant encouragement, guidance and support though my Ph.D study at HKUST and Université de Grenoble. Without their consistent and illuminating instructions, this thesis could not have reached its present form.

Also, I want to thank Professor David COOK for agreeing to chair my thesis examination and Professor Skandar BASROUR, Dr. Philippe BLANC-BENON, Professor Philippe COMBETTE, Professor Wenjing YE and Professor Levent YOBAS for agreeing to serve as members of my thesis examination committee.

I would like to thank Dr. Sébastien OLLIVIER, Dr. Edouard SALZE and Dr. Petr YULDASHEV, who are from Laboratoire de Mécanique des Fluides et d'Acoustique (LMFA, Ecole Centrale de Lyon) and Dr. Olivier LESAIN, who is from Grenoble Génie Electrique (G2E lab); the group of Professor Pascal NOUET, who is from Laboratoire d'Informatique, de Robotique et de Microélectronique de Montpellier (LIRMM, l'Université Montpellier 2); and Dr. Didace EKEOM, who is from the Microsonics company (<http://www.microsonics.fr/>), for their help in guiding the microphone dynamic calibration experiment, offering the first prototype of the amplification card and teaching the ANSYS simulation software under the project *Microphone de Mesure Large Bande en Silicium pour l'Acoustique en Hautes Fréquences* (SIMMIC), which is financially supported by French National Research Agency (ANR) Program BLANC 2010 SIMI 9.

I have appreciated the help of the staffs from the nanoelectronics fabrication facility (NFF) and materials characterization and preparation facility (MCPF) of HKUST and the technicians from the Department of Electronic and Computer Engineering and the Department of Mechanical Engineering of HKUST. Also I have appreciated the help of the engineers from the campus d'innovation pour les micro et nanotechnologies (MINATEC).

Through my Ph.D study period, much assistance has been given by my colleagues and friends at HKUST. I appreciate their kindly help and support and would like to thank them all, especially Ruiqing ZHU, Zhi YE, Thomas CHOW, Dongli ZHANG, Parco WONG, Zhaojun LIU, Shuyun ZHAO, He LI, Fan ZENG and Lei LU.

During my periods of stay in Grenoble, many friends helped me to quickly settle in and integrate into the French culture. I would like to thank them all, especially Hai YU, Wenbin YANG, Ke HUANG, Yi GANG, Richun FEI, Nan YU, Zuheng MING, Haiyang DING, Weiyuan NI, Hao GONG, Zhongyang LI, Bo WU, Josue ESTEVES, Yoan CIVET, Maxime DEFOSSEUX, Matthieu CUEFF and Mikael COLIN.

Last but not least, I devote my deepest gratitude to my parents for their immeasurable support over the years.



**To my family**

# Table of Contents

High Frequency MEMS Sensor for Aero-acoustic Measurements .....	ii
Authorization.....	iii
Acknowledgments .....	vi
Table of Contents .....	ix
List of Figures .....	xii
List of Tables.....	xvii
Abstract .....	xviii
Résumé.....	xx
Publications .....	xxi
Chapter 1: Introduction .....	1
1.1 Introduction of the Aero-Acoustic Microphone .....	1
1.1.1 Definition of Aero-Acoustics and Research Motivation .....	1
1.1.2 Wide-Band Microphone Performance Specifications .....	3
1.2 A Comparative Study of Current State-of-the-art MEMS Capacitive and Piezoresistive Microphones.....	5
1.3 Existing Fabrication Techniques for Piezoresistive Aero-Acoustic Microphones .....	10
1.4 Summary .....	12
1.5 References .....	13
Chapter 2: MEMS Sensor Design and Finite Element Analysis.....	16
2.1 Key Material Properties .....	16
2.1.1 Diaphragm Material Residual Stress.....	16
2.1.2 Diaphragm Material Density and Young’s Modulus.....	20
2.2 Design Considerations.....	24
2.3 Mechanical Structure Modeling .....	28
2.4 Summary .....	36
2.5 References .....	37
Chapter 3: Fabrication of the MEMS Sensor .....	38

3.1 Review of Metal-induced Laterally Crystallized Polycrystalline Silicon Technology	38
3.2 Surface Micromachining Process	44
3.2.1 Sacrificial Materials and Cavity Formation Technology	44
3.2.2 Contact and Metallization Technology	54
3.2.3 Details of Fabrication Process Flow	58
3.3 Silicon Bulk Micromachining Process	65
3.3.1 Comparison of Bulk Silicon Wet Etching and Dry Etching Techniques	65
3.3.2 Details of Fabrication Process Flow	68
3.4 Summary	72
3.5 References	73
Chapter 4: Testing of the MEMS Sensor	77
4.1 Sheet Resistance and Contact Resistance	77
4.2 Static Point-load Response	80
4.3 Dynamic Calibration	84
4.3.1 Review of Microphone Calibration Methods	84
4.3.1.1 Reciprocity Method	84
4.3.1.2 Substitution Method	86
4.3.1.3 Pulse Calibration Method	88
4.3.2 The Origin, Characterization and Reconstruction Method of N Type Acoustic Pulse Signals	90
4.3.2.1 The Origin and Characterization of the N-wave	91
4.3.2.2 N-wave Reconstruction Method	96
4.3.3 Spark-induced Acoustic Response	99
4.3.3.1 Surface Micromachined Devices	102
4.3.3.2 Bulk Micromachined Devices	105
4.4 Sensor Array Application as an Acoustic Source Localizer	108
4.5 Summary	116
4.6 References	117
Chapter 5: Summary and Future Work	119
5.1 Summary	119

5.2 Future Work.....	122
5.3 References.....	123
Appendix I: Co-supervised Ph.D Program Arrangement.....	124
Appendix II: Extended Résumé .....	125

# List of Figures

Figure 1.1: Schematic of a typical capacitive microphone. ....	6
Figure 1.2: Schematic of a typical piezoresistive microphone.....	7
Figure 1.3: Process flow of the fusion bonding technique.....	10
Figure 1.4: Process flow of the low temperature direct bonding with smart-cut technique. ...	11
Figure 2.1: Bending of the film-substrate system due to the residual stress.....	17
Figure 2.2: Layout of a single die. ....	18
Figure 2.3: Layout of the rotational beam structure.....	19
Figure 2.4: Microphotography of two typical rotational beams after releasing.....	20
Figure 2.5: Layout of the doubly-clamped beams.....	21
Figure 2.6: Resonant frequency measurement setup.....	22
Figure 2.7: Typical measurement result of the laser vibrometer. ....	22
Figure 2.8: Surface micromachining technique. ....	24
Figure 2.9: Bulk micromachining technique.....	25
Figure 2.10: Schematic of the microphone physical structure using the surface micromachining technique. ....	27
Figure 2.11: Schematic of the microphone physical structure using the bulk micromachining technique. ....	27
Figure 2.12: Layout of a fully clamped square diaphragm. ....	29
Figure 2.13: ANSYS first mode resonant frequency simulation of a square diaphragm. ....	30
Figure 2.14: Sensor analogies. ....	31
Figure 2.15: Mechanical frequency response of a square diaphragm. ....	32
Figure 2.16: Layout of a beam supported diaphragm (reference resistors are not shown). ....	33
Figure 2.17: Cross-sectional view of coupled acoustic-mechanical FEA model. ....	34
Figure 2.18: Mechanical frequency response of a beam supported square diaphragm.....	35
Figure 3.1: Ni/Si equilibrium free-energy diagram.....	43
Figure 3.2: Cross-sectional view of microphone before release. ....	45
Figure 3.3: Cross-sectional view of microphone after first TMAH etching. ....	45

Figure 3.4: Amorphous silicon etching rate at 60°C TMAH.....	45
Figure 3.5: Cross-sectional view of microphone after BOE etching. ....	46
Figure 3.6: Cross-sectional view of microphone after second TMAH etching.....	46
Figure 3.7: Sacrificial oxide layer etching profile.....	47
Figure 3.8: Sacrificial oxide layer lateral etching rate. ....	47
Figure 3.9: Detail of the etching profile due to the dimple mold.....	49
Figure 3.10: AFM measurement of the substrate sc-silicon etching profile due to the dimple mold in room temperature TMAH solution. ....	52
Figure 3.11: Silicon lateral etching rate of the TMAH solution at room temperature. ....	53
Figure 3.12: Silicon vertical etching rate of the TMAH solution at room temperature. ....	53
Figure 3.13: Metal peel-off due to large residual stress. ....	54
Figure 3.14: Reverse trapezoid shape of the dual tone photoresist.....	55
Figure 3.15: Cross-sectional view of microphone after Ti sputtering.....	56
Figure 3.16: Cross-sectional view of microphone after the silicidation process. ....	56
Figure 3.17: Contact resistance comparison (different HF pre-treatment time). ....	57
Figure 3.18: Contact resistance comparison (with/without silicidation).....	57
Figure 3.19: Thermal oxide hard mask. ....	58
Figure 3.20: Photolithography for dimple mold.....	58
Figure 3.21: Etching of thermal oxide hard mask.....	58
Figure 3.22: Etching of the reverse dimple mold.....	58
Figure 3.23: Deposition of sacrificial layers. ....	59
Figure 3.24: Diaphragm area photolithography. ....	59
Figure 3.25: Diaphragm area etching.....	59
Figure 3.26: Piezoresistor material deposition.....	60
Figure 3.27: Define piezoresistor shape.....	60
Figure 3.28: LTO deposition. ....	61
Figure 3.29: Open induce hole. ....	61
Figure 3.30: Ni evaporation. ....	61
Figure 3.31: Microphotography of amorphous silicon after re-crystallization.....	61
Figure 3.32: Remove Ni and high temperature annealing. ....	61

Figure 3.33: Boron doping and activation.....	62
Figure 3.34: Second low stress nitride layer deposition.....	62
Figure 3.35: Open contact hole.....	63
Figure 3.36: Open release hole.....	64
Figure 3.37: Metallization after lift-off process.....	64
Figure 3.38: Microphotography of a wide-band high frequency microphone fabricated using the surface micromachining technique.....	64
Figure 3.39: Etching profile of the KOH/TMAH solutions.....	66
Figure 3.40: Top view of an arbitrary backside opening etching shape.....	67
Figure 3.41: Diaphragm layers deposition.....	68
Figure 3.42: Piezoresistor forming.....	68
Figure 3.43: Piezoresistor protection and backside hard mask deposition.....	69
Figure 3.44: Metallization.....	69
Figure 3.45: Diaphragm area patterning.....	70
Figure 3.46: Cross-sectional view of the microphone device after dry etching release.....	70
Figure 3.47: Microphotography of a wide-band high frequency microphone fabricated using bulk micromachining technique.....	70
Figure 3.48: Cross-sectional view microphotography of the cut die edge.....	71
Figure 4.1: Layout of the Greek cross structure.....	77
Figure 4.2: Layout of the Kelvin structure.....	78
Figure 4.3: Static measurement setup.....	80
Figure 4.4: Cross-sectional view of the probe applying the point-load.....	80
Figure 4.5: Wheatstone bridge configuration.....	81
Figure 4.6: Typical measurement result with a diaphragm length of 115 $\mu$ m and thickness of 0.5 $\mu$ m (fabricated using the surface micromachining technique).....	81
Figure 4.7: Typical measurement result with a diaphragm length of 210 $\mu$ m and thickness of 0.5 $\mu$ m (fabricated using the bulk micromachining technique).....	82
Figure 4.8: Point-load vs. displacement relationships of sensors fabricated using two different micromachining techniques.....	83
Figure 4.9: Equivalent pressure vs. displacement relationships of sensors fabricated using two	

different micromachining techniques.....	83
Figure 4.10: Principle of Pressure Reciprocity Calibration. The three microphones (A, B and C) are coupled two at a time together by the air (or gas) enclosed in a cavity while the three ratios of output voltage and input current are measured. Each ratio equals the Electrical Transfer Impedance valid for the respective pair of microphones. ....	86
Figure 4.11: Pulse signals and their corresponding spectrums. ....	89
Figure 4.12: An ideal N-wave in 10 $\mu$ s duration and its corresponding frequency spectrum. .	90
Figure 4.13: N-wave near projectile (a) Cone-cylinder, (b) Sphere.....	91
Figure 4.14: N-wave generation process.....	92
Figure 4.15: Schematic of the shock tube. ....	93
Figure 4.16: High voltage capacitor discharge scheme.....	94
Figure 4.17: Schematic of an ideal N-wave. ....	96
Figure 4.18: Real N-wave shape. ....	97
Figure 4.19: Shadowgraph experiment setup (1. spark source, 2. microphone in a baffle, 3. nanolight flash lamp, 4 focusing lens, 5. camera, 6. lens). ....	98
Figure 4.20: Comparison between the optically measured rise time and the predicted rise time by using the acoustic wave propagation at different distances from the spark source.....	98
Figure 4.21: Schematic of the amplifier. ....	100
Figure 4.22: Frequency response of the amplification card. ....	100
Figure 4.23: Spark calibration test setup.....	101
Figure 4.24: Baffle design.....	101
Figure 4.25: Typical spark measurement result of a microphone sample fabricated using the surface micromachining technique (3V DC bias, with amplification gain 1000 and source to microphone distance is 10cm).....	103
Figure 4.26: FFT single-sided amplitude spectra of the measured signals from a surface micromachined microphone and from optical method. ....	103
Figure 4.27: Frequency response of the calibrated microphone (3V DC bias, with amplification gain 1000, averaged signal), compared with FEA result. ....	104
Figure 4.28: Acoustic short circuit induced leakage pressure $P_s$ . ....	104
Figure 4.29: Typical spark measurement result of a microphone sample fabricated using the	



bulk micromachining technique (3V DC bias, with amplification gain 1000 and source to microphone distance is 10cm).....	105
Figure 4.30: FFT single-sided amplitude spectra of the measured signals from a bulk micromachined microphone and from optical method. ....	105
Figure 4.31: Frequency response of the calibrated microphone (3V DC bias, with amplification gain 1000, averaged signal), compared with lumped-element modeling result. ....	106
Figure 4.32: Comparison of the spark measurement results of microphones fabricated by two different techniques (spark source to microphone distance is 10cm). ....	107
Figure 4.33: Comparison of the frequency responses of microphones fabricated by two different techniques. ....	107
Figure 4.34: Cartesian coordinate system for acoustic source localization. ....	108
Figure 4.35: Sensor array coordinates.....	109
Figure 4.36: Sound velocity calibration setup.....	110
Figure 4.37: Sound velocity extrapolation. ....	110
Figure 4.38: Acoustic source localization setup.....	111
Figure 4.39: GUI initialization for sound velocity input.....	111
Figure 4.40: Localization GUI main window.....	112
Figure 4.41: Localization test Z coordinate system. ....	113
Figure 4.42: Sound source position definition. ....	113
Figure 4.43: Coordinates comparisons between the pre-measured values and the calculated values, (a): X coordinates; (b) Y coordinates and (c) Z coordinates. ....	114
Figure 4.44: Y coordinates differences between the pre-measured values and the calculated values due to unlevel ground surface. ....	115

## List of Tables

Table 1.1: Current state-of-the-art of developed MEMS aero-acoustic microphones. ....	8
Table 1.2: Scaling properties of MEMS microphones. ....	9
Table 1.3: Scaling example. ....	9
Table 2.1: Curvature method measurement parameters and results. ....	17
Table 2.2: Rotational beam design parameters. ....	19
Table 2.3: Dimension of different beams (length×width [ $\mu\text{m}\times\mu\text{m}$ ]). ....	21
Table 2.4: First mode resonant frequencies of different beams (1 $\mu\text{m}$ thick). ....	23
Table 2.5: Square diaphragm modeling parameters. ....	29
Table 2.6: Variable analogy. ....	30
Table 2.7: Element analogy. ....	31
Table 2.8: Coupled acoustic-mechanical modeling parameters. ....	35
Table 4.1: Summary of different microphone calibration methods. ....	90
Table 4.2: Distance between table surface and ground surface at different positions. ....	115
Table 5.1: Comparisons of current work and state-of-the-art. ....	121

# High Frequency MEMS Sensor for Aero-acoustic Measurements

By **ZHOU, Zhijian**

Electronic and Computer Engineering

The Hong Kong University of Science and Technology

and

Ecole Doctorale Electronique, Electrotechnique, Automatique & Traitement du Signal

Université de Grenoble

## Abstract

Aero-acoustics, a branch of acoustics which studies noise generation via either turbulent fluid motion or aerodynamic forces interacting with surfaces, is a growing area and has received fresh emphasis due to advances in air, ground and space transportation. While tests of a real object are possible, the setup is usually complicated and the results are easily corrupted by the ambient noise. Consequently, testing in relatively tightly-controlled laboratory settings using scaled models with reduced dimensions is preferred. However, when the dimensions are reduced by a factor of  $M$ , the amplitude and the bandwidth of the corresponding acoustic waves are increased by  $10\log M$  in decibels and  $M$ , respectively. Therefore microphones with a bandwidth of several hundreds of kHz and a dynamic range covering 40Pa to 4kPa are needed for aero-acoustic measurements.

Micro-Electro-Mechanical-system (MEMS) microphones have been investigated for more than twenty years, and recently, the semiconductor industry has put more and more concentration on this area. Compared with all other working principles, due to their scaling

characteristic, piezoresistive type microphones can achieve a higher sensitivity bandwidth (SBW) product, and in turn they are well suited for aero-acoustic measurements. In this thesis, two metal-induced-lateral-crystallized (MILC) polycrystalline silicon (poly-Si) based piezoresistive type MEMS microphones are designed and fabricated using surface micromachining and bulk micromachining techniques, respectively. These microphones are calibrated using an electrical spark generated shockwave (N-wave) source. For the surface micromachined sample, the measured static sensitivity is  $0.4\mu\text{V/V/Pa}$ , dynamic sensitivity is  $0.033\mu\text{V/V/Pa}$  and the frequency range starts from 100kHz with a first mode resonant frequency of 400kHz. For the bulk micromachined sample, the measured static sensitivity is  $0.28\mu\text{V/V/Pa}$ , dynamic sensitivity is  $0.33\mu\text{V/V/Pa}$  and the frequency range starts from 6kHz with a first mode resonant frequency of 715kHz.

## Résumé

L'aéroacoustique est une filière de l'acoustique qui étudie la génération de bruit par un mouvement fluide turbulent ou par les forces aérodynamiques qui interagissent avec les surfaces. Ce secteur en pleine croissance a attiré des intérêts récents en raison de l'évolution de la transportation aérienne, terrestre et spatiale. Alors que les tests sur un objet réel sont possibles, leur implantation est généralement compliquée et les résultats sont facilement corrompus par le bruit ambiant. Par conséquent, les tests plus strictement contrôlés au laboratoire utilisant les modèles de dimensions réduites sont préférables. Toutefois, lorsque les dimensions sont réduites par un facteur de  $M$ , l'amplitude et la bande passante des ondes acoustiques correspondantes se multiplient respectivement par  $10\log M$  en décibels et par  $M$ . Les microphones avec une bande passante de plusieurs centaines de kHz et une plage dynamique couvrant de 40Pa à 4 kPa sont ainsi nécessaires pour les mesures aéroacoustiques.

Les microphones MEMS ont été étudiés depuis plus de vingt ans, et plus récemment, l'industrie des semiconducteurs se concentre de plus en plus sur ce domaine. Par rapport à tous les autres principes de fonctionnement, grâce à la caractéristique de minimisation, les microphones de type piézorésistif peuvent atteindre une bande passante de sensibilité (SBW) plus élevée et sont ainsi bien adaptés pour les mesures aéroacoustiques. Dans cette thèse, deux microphones MEMS de type piézorésistif à base de silicium polycristallin (poly-Si) latéralement cristallisé par l'induction métallique (MILC) sont conçus et fabriqués en utilisant respectivement les techniques de microfabrication de surface et de volume. Ces microphones sont calibrés à l'aide d'une source d'onde de choc (N-wave) générée par une étincelle électrique. Pour l'échantillon fabriqué par le micro-usinage de surface, la sensibilité statique mesurée est  $0.4\mu\text{V/V/Pa}$ , la sensibilité dynamique est  $0.033\mu\text{V/V/Pa}$  et la plage fréquentielle couvre à partir de 100 kHz avec une fréquence du premier mode de résonance à 400kHz. Pour l'échantillon fabriqué par le micro-usinage de volume, la sensibilité statique mesurée est  $0.28\mu\text{V/V/Pa}$ , la sensibilité dynamique est  $0.33\mu\text{V/V/Pa}$  et la plage fréquentielle couvre à partir de 6 kHz avec une fréquence du premier mode de résonance à 715kHz.

## Publications

1. Zhou, Z. J., Rufer, L. and Wong, M., "Aero-Acoustic Microphone with Layer-Transferred Single-Crystal Silicon Piezoresistors," The 15th Int. Conf. on Solid-State Sensors, Actuators and Microsystems, Denver, USA, June 21-25, pp. 1916-1919, 2009.
2. Zhou, Z. J., Wong, M. and Rufer, L., "The Design, Fabrication and Characterization of a Piezoresistive Tactile Sensor for Fingerprint Sensing," The 9th Annual IEEE Conference on Sensors, Hawaii, USA, Nov. 1-4, pp. 2589-2592, 2010.
3. Z. Zhou, M. Wong and L. Rufer, "Wide-band piezoresistive aero-acoustic microphone," in VLSI and System-on-Chip (VLSI-SoC), 2011 IEEE/IFIP 19th International Conference, Hong Kong, Oct. 3-5, pp. 214-219, 2011.
4. Zhou, Z. J., Rufer, L., Wong, M., Salze, E., Yuldashev, P. and Ollivier, S., "Wide-Band Piezoresistive Microphone for Aero-Acoustic Applications," The 11th Annual IEEE Conference on Sensors, Taipei, Taiwan, Oct. 28-31, pp. 818-821, 2012.
5. Zhou, Z. J., Rufer, L., Salze, E., Ollivier, S and Wong, M, "Wide-Band Aero-Acoustic Microphone With Improved Low-Frequency Characteristics," The 17th Int. Conf. on Solid-State Sensors, Actuators and Microsystems, Barcelona, SPAIN, June. 16-20, 2013 (accepted).

# Chapter 1: Introduction

For clarity and ease of understanding, in this thesis, the high frequency MEMS sensor will also be called the wide-band MEMS aero-acoustic microphone. And in this chapter, the definition of the aero-acoustic microphone will be introduced first. Following that will be the performance specification requirements of the wide-band aero-acoustic microphone. In the second part of this chapter, a comparative study of the two main current state-of-the-art MEMS type microphones, capacitive and piezoresistive, will be presented, and reasons will be given to demonstrate the advantages of using the piezoresistive sensing technique.

## 1.1 Introduction of the Aero-Acoustic Microphone

### 1.1.1 Definition of Aero-Acoustics and Research Motivation

Aero-acoustics, a branch of acoustics which studies noise generation via either turbulent fluid motion or aerodynamic forces interacting with surfaces, is a growing area and has received fresh emphasis due to advances in air, ground and space transportation. Even though no complete scientific theory of the generation of noise by aerodynamic flows has been established, most practical aero-acoustic analyses rely on the so-called acoustic analogy, whereby the governing equations of the motion of the fluid are coerced into a form reminiscent of the wave equation of classical (linear) acoustics.

In accordance with the above definition, research is mainly focused on three aero-acoustic areas. Firstly, significant advances in aero-acoustics are required for reducing community and cabin noise from subsonic aircraft and to prepare for the possible large scale entry of supersonic aircraft into civil aviation. The use of high thrust producing engines in military aircraft has raised numerous concerns about the exposure of aircraft carrier personnel and sonic fatigue failure of aircraft structures. Secondly, in the ground transportation arena, efforts

are currently underway to minimize the aerodynamic noise from automobiles and high speed trains. Finally, space launch vehicle noise, if uncontrolled, can cause serious structural damage to the spacecraft and payload. In addition, with the proliferation of space flight, launch vehicle noise can also become a significant environmental issue. It has become increasingly important to address all of the above noise issues in order to minimize the noise impact of advances in transportations.

While tests/measurements of an object in a real situation are possible, the expense is too high, the setup is usually complicated and the results are easily corrupted by the ambient noise and environmental parameters changes, such as fluctuations of temperature and humidity. Consequently, testing in relatively tightly-controlled laboratory settings using scaled models with reduced dimensions is preferred.

Although in some scaled model aero-acoustic measurements, the optical method could get a result that matches well with the theoretical estimation, the setup itself is complicated and the estimation of the pressure from the optical measurements is limited to particular cases (plane or spherical waves). So a microphone is still required by acoustic researchers in aero-acoustic and other fields for various applications, including experimental investigation of sound propagation based on laboratory experiments where wavelengths, distances and other lengths are scaled down with factors of 1:20 to 1:1000 (applications are the modeling of sound propagation in halls, in streets, or outdoor long range sound propagation in a complex atmosphere) and metrology problems where knowledge of the sound field is critical (e.g. determination of gas parameters [1]).

In a scaled model, when the dimensions are reduced by a factor of  $M$ , the amplitude and the bandwidth of the corresponding acoustic waves are increased by  $10\log M$  in decibels and  $M$ , respectively. There are some publications that include the words “aero-acoustic microphone” in their titles; however, they are mostly focused on the measurement of aircraft airframe noise [2], landing gear noise [3], and wind turbine noise [4], etc. in a wind tunnel, with a scaling factor  $M$  no larger than 10. In contrast, our research is focused on applications with a much



larger scaling factor ( $M$  larger than 20). A typical example is that, for a Titan IV rocket with a characteristic length of 44m travelling at Mach 7, a shockwave with a rise time of  $\sim 0.1$ ms (or  $\sim 10$ kHz) and an over-pressure of  $\sim 180$ Pa (or  $\sim 139$ dB Sound Pressure Level) [5] can be measured at a distance of  $\sim 1.1$ km from the exhaust. If this were studied using a scaled model with  $M = 100$ , the corresponding characteristics of the shockwave would be  $\sim 1$ MHz and  $\sim 159$ dB (or  $\sim 1.8$ kPa) at a distance of  $\sim 11$ m from the source.

Advances in wide-band aero-acoustic metrology could contribute significantly to the above mentioned research and application topics. These advances could result in progress in the understanding of some noise generation and the modeling of noise propagation, and thus could have significant industrial/commercial (supersonic aviation development, defense applications) and environmental/social (noise reduction) impacts. The understanding of sonic boom generation and propagation in atmospheric turbulence is for example a critical point in the development of future supersonic civil aircraft. The availability of wide-band microphones should also allow for some new, emerging applications, like individual gunshot detection tools. The new sensor would also meet the requirements of some other markets in the field of ultrasound application, such as non-destructive control, ultrasonic imaging, ultrasonic flow meters, etc.

### 1.1.2 Wide-Band Microphone Performance Specifications

Most of the previous works on MEMS microphones have concerned the design of low-cost audio microphones for mobile phone applications. In contrast, the goal of this thesis is clearly focused on metrology applications in airborne acoustics and more particularly on acoustic scaled model applications where accurate measurements of wide-band pressure waves with frequency ranges of hundreds of kHz and pressure levels up to 4kPa are critical. The frequency range from 20Hz to 140kHz and the pressure range from  $20\mu$ Pa to 2kPa is well covered with standard 1/8" condenser microphones, and some research has been done to design MEMS measuring microphones [6]. However, the sensitivity of such microphones in

(mV/Pa) above 50kHz is not accurately known and the validity of available calibration methods has not been assessed. Research on MEMS resonant narrowband ultrasound sensors has also been done [7]. But there are currently no calibrated sensors specifically designed for wide-band aero-acoustic measurements.

Researchers from Université du Maine went another way. They tried to model the high frequency vibration properties of a microphone which was originally designed for low frequency applications (such as B&K 4134) and prepared to use such a low frequency microphone for high frequency measurements [8]. However, from the diaphragm vibration displacement measurement result, there were differences between the analytical modeling and the measurements from the laser vibrometer, which limits the application of this idea.

## 1.2 A Comparative Study of Current State-of-the-art MEMS Capacitive and Piezoresistive Microphones

To cover a wide frequency range, electro-acoustic transducers for acoustic signal generation and detection in the air traditionally use piezoelectric elements. The conventional piezoelectric bulk transducers vibrating in thickness or flexural modes have been widely used as pressure sensors [9]. One of the drawbacks of these systems is the necessity of using matching layers on the transducer active surface that minimize a substantive difference between the acoustic impedances of the transducer and the propagating medium. The efficiency of these layers is frequency dependent and process dependent. Although these transducers can work in the range of several hundreds of kHz, they suffer from a narrow frequency band (due to their resonant behaviour) and a relatively low sensitivity, resulting in low signal dynamics.

Other most commonly used electro-acoustic transducers are capacitive type and piezoresistive type microphones. In the capacitive type microphone, the diaphragm acts as one plate of a capacitor, and the vibrations produce changes in the distance between the plates. A typical bulk-micromachined condenser microphone is shown in Figure 1.1 [10]. With a DC-bias, the plates store a fixed charge ( $Q$ ). According to the capacitance Equation 1.1, where  $C$  is the capacitance and  $V$  is the potential difference. The capacitance,  $C$ , of a parallel plate capacitor is also inversely proportional to the distance between plates (Equation 1.2), where  $\epsilon$  is the permittivity of the medium in the gap (normally air),  $A$  is the area of the plates and  $d$  is the separation between plates. With fixed charge, plates' areas and gap medium, the voltage maintained across the capacitor plates changes with the separation fluctuation, which is caused by the air vibration (Equation 1.3).

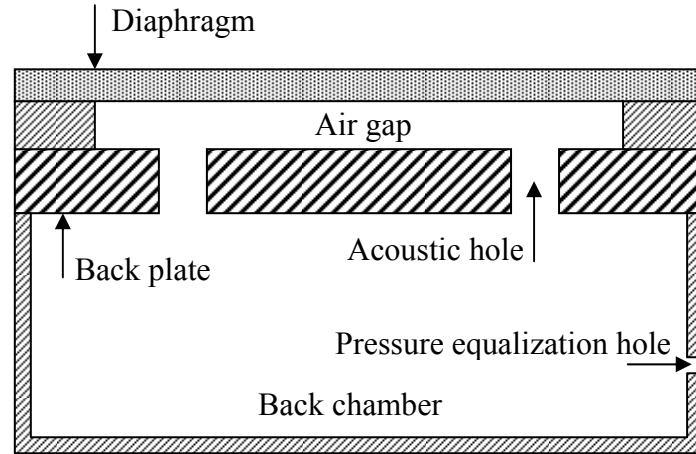


Figure 1.1: Schematic of a typical capacitive microphone.

$$C = \frac{Q}{V} \quad (1.1)$$

$$C = \frac{\varepsilon A}{d} \quad (1.2)$$

$$V = \frac{Q}{\varepsilon A} d \quad (1.3)$$

The piezoresistive type microphone consists of a diaphragm that is provided with four piezoresistors in a Wheatstone bridge configuration (Figure 1.2) [11]. Piezoresistors function based on the piezoresistive effect, which describes the changing electrical resistance of a material due to applied mechanical stress. This effect in semiconductor materials can be several orders of magnitudes larger than the geometrical piezoresistive effect in metals and is present in materials like germanium, poly-Si, amorphous silicon (*a*-Si), silicon carbide, and single-crystalline silicon (sc-Si). The resistance of silicon changes not only due to the stress dependent change of geometry, but also due to the stress dependent resistivity of the material. The resistance of n-type silicon mainly changes due to a shift of the three different conducting valley pairs. The shifting causes a redistribution of the carriers between valleys with different mobilities. This results in varying mobilities, dependent on the direction of the current flow. A minor effect is due to the effective mass change related to the changing shapes of the valleys. In p-type silicon, the phenomena are more complex and also result in mass changes and hole transfer. For thin diaphragms and small deflections, the resistance change is linear with applied pressure.

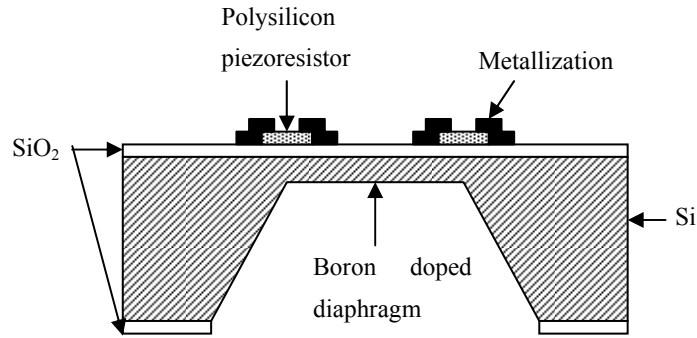


Figure 1.2: Schematic of a typical piezoresistive microphone.

Table 1.1 presents the current state-of-the-art of several developed MEMS aeroacoustic microphones compared with a traditional B&K condenser microphone. To make the microphone suitable for wide-band high frequency measurement, a key point is the device scaling issue. For the piezoresistive type microphone, the stress in the diaphragm is proportional to  $(a/h)^2$  [12], where  $a$  is the diaphragm dimension and  $h$  is the diaphragm thickness. This stress creates a change in resistance through the piezoresistive transduction coefficients. Thus, the sensitivity will not be reduced as the area is reduced as long as the aspect ratio remains the same. The bandwidth of the microphone is dominated by the resonant frequency of the diaphragm, which scales as  $h/a^2$ ; thus, as the diaphragm size is reduced, the bandwidth will increase [13]. On the other hand, the scaling analysis for the capacitive type microphone is more complicated. The sensitivity depends on both the compliance of the diaphragm and the electric field in the air gap [10]. The sensitivity is proportional to the electric field,  $V_B/g$ , the aspect ratio of the diaphragm,  $(a/h)^2$ , and the ratio of the diaphragm area to the diaphragm thickness,  $(A/h)$ , where  $V_B$  is the bias voltage,  $g$  is the gap thickness and  $A$  is the diaphragm surface area. Thus, the sensitivity will be reduced as the area is reduced, even if the aspect ratio is kept as a constant. If the electric field,  $V_B/g$ , remains constant, this component of the sensitivity will not be affected by scaling. However, there is an upper limit to the bias voltage that can be used with capacitive microphones due to electrostatic collapse of the diaphragm, which is known as pull-in voltage. This pull-in voltage is proportional to  $g^{3/2}$  [14]. Thus, the electric field will scale as  $g^{1/2}$  and will be negatively affected by a reduction in microphone size. Table 1.2 [15] summarizes the scaling properties of MEMS capacitive type and piezoresistive type microphones, in which the SBW is defined to be the

product of the sensitivity and the bandwidth of the microphone. From Table 1.2 we find that, assuming the diaphragm aspect ratio is not changed, as the microphone dimensions are reduced, the overall performance of the piezoresistive microphone will increase, while the performance of the capacitive microphone will decrease. Table 1.3 uses work done by Hansen [16] and Arnold [17] to demonstrate the better scaling property of the piezoresistive sensing mechanism.

Microphone	Type	Radius (mm)	Max pressure (dB)	Noise floor (dB)	Sensitivity	Bandwidth (predicted)
B&K 4138	capacitive	1.6	168	43dB(A)	5 $\mu$ V/V/Pa (200V)	6.5Hz ~ 140kHz
Martin et al. [15]	capacitive	0.23	164	41	21 $\mu$ V/V/Pa (18.6V)	300Hz ~ 25.4kHz (~100kHz)
Hansen et al. [16]	capacitive	0.07 $\times$ 0.19	NA	63.6dB(A)	9.3 $\mu$ V/V/Pa (5.8V)	0.1Hz ~ 100kHz
Arnold et al. [17]	piezoresistive	0.5	160	52	0.6 $\mu$ V/V/Pa (3V)	10Hz ~ 19kHz (~100kHz)
Sheplak et al. [18]	piezoresistive	0.105	155	92	2.2 $\mu$ V/V/Pa (10V)	200Hz ~ 6kHz (~300kHz)
Horowitz et al. [19]	piezoelectric (PZT)	0.9	169	48	1.66 $\mu$ V/Pa	100Hz ~ 6.7kHz (~50.8 kHz)
Williams et al. [20]	piezoelectric (AlN)	0.414	172	40.4	39 $\mu$ V/Pa	69Hz ~20kHz (>104kHz)
Hillenbrand et al. [21]	piezoelectric (Cellular PP)	0.3cm <sup>2</sup>	164	37dB(A)	2mV/Pa	10Hz ~ 10kHz (~140kHz)
Kadirvel et al. [22]	optical	0.5	132	70	0.5mV/Pa	300Hz ~ 6.5kHz (100kHz)

Table 1.2: Scaling properties of MEMS microphones.				
Microphone type	Sensitivity	Bandwidth	SBW	Summary
Piezoresistive	$V_B \cdot \frac{a^2}{h^2}$	$\frac{h}{a^2}$	$\frac{V_B}{h}$	S -, BW ↑, SBW ↑
Capacitive	$\frac{V_B}{g} \cdot \frac{A}{h} \cdot \frac{a^2}{h^2}$	$\frac{h}{a^2}$	$\frac{V_B}{g} \cdot \frac{a^2}{h^2}$	S ↓, BW ↑, SBW ↓

Table 1.3: Scaling example.				
	Piezoresistive		Capacitive	
	Sensitivity	Bandwidth	Sensitivity	Bandwidth
Scaling equation	$V_B \cdot \frac{a^2}{h^2}$	$\frac{h}{a^2}$	$\frac{V_B}{g} \cdot \frac{A}{h} \cdot \frac{a^2}{h^2}$	$\frac{h}{a^2}$
Original value	1.8μV/Pa	100kHz	53.94μV/Pa	100kHz
Scale by BW ( $a$ ↓ 6 times, keep $a/h$ constant)	1.8μV/Pa	600kHz	$\frac{V_B}{g} \propto g^{\frac{1}{2}}$	$\frac{A}{h}$
			$C = \epsilon A/g$ constant -> $g \downarrow 36$ times	↓ 6 times
			1.5μV/Pa	
Scaled SBW	1080		900	

### 1.3 Existing Fabrication Techniques for Piezoresistive Aero-Acoustic Microphones

Single crystalline silicon was mainly used for the piezoresistive aero-acoustic microphone fabrication due to its high gauge factor [18, 23]. Bonding techniques were used, including the high temperature fusion bonding technique and plasma enhanced low temperature direct bonding technique. Figure 1.3 presents the simplified process flow of the fusion bonding technique. The handle wafer was firstly patterned to form the cavity shape and the SOI wafer was deposited with silicon nitride (SiN) material. Then, these two wafers were fusion bonded together and the top SOI wafer was etched back to the top silicon layer. Finally, this silicon layer was used as the piezoresistive sensing layer to fabricate the piezoresistors.

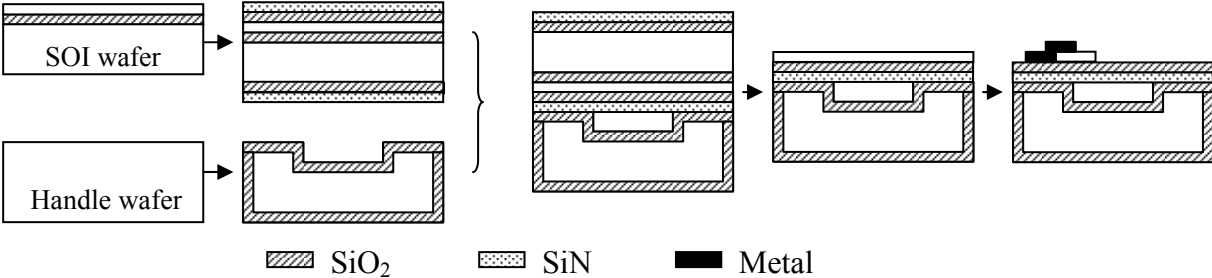


Figure 1.3: Process flow of the fusion bonding technique.

Figure 1.4 presents the simplified process flow of the low temperature direct bonding with smart-cut technique. The handle wafer was firstly patterned with sacrificial layers and covered with silicon nitride material. The implantation wafer was heavily doped with hydrogen. After plasma surface activation, these two wafers were bonded together at room temperature and annealed at 300°C to increase the bonding strength. Then, a higher temperature annealing at 550°C was carried out. The heavily doped hydrogen formed gas bubbles at this temperature, and this led to micro-cracks in the doping areas. Finally, a thin silicon layer was separated and transferred to the handle wafer. This transferred silicon layer was used as the piezoresistive sensing material, and finally, the diaphragm was released using the surface micromachining technique.



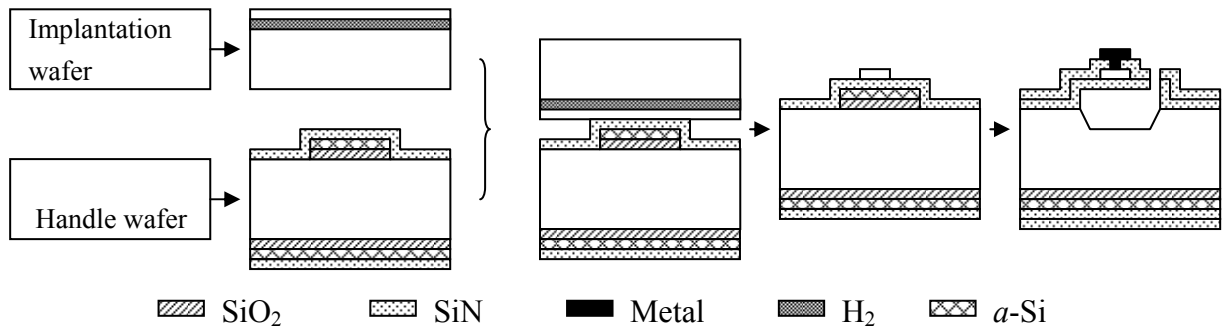


Figure 1.4: Process flow of the low temperature direct bonding with smart-cut technique.

Although the single crystalline silicon material has a large gauge factor, the bonding process complicates the process flow and the bonding technique does not offer a high yield. Later in this thesis, re-crystallized polycrystalline silicon material will be introduced to replace the single crystalline silicon material to fabricate the piezoresistors.

## 1.4 Summary

The clear goal of this thesis is proposed in this chapter. The wide-band MEMS aero-acoustic microphone discussed in this thesis is defined to have a large bandwidth of several hundreds of kHz and dynamic range up to 4kPa. After comparison with other sensing mechanisms such as the piezoelectric and capacitive types, a piezoresistive sensing mechanism is chosen based on the SBW scaling properties.

## 1.5 References

- [1] B. Baligand and J. Millet, "Acoustic Sensing for Area Protection," in *Battlefield Acoustic Sensing for ISR Applications*, pp. 4-1-4-12, 2006.
- [2] S. Oerlemans, L. Broersma, and P. Sijtsma, "Quantification of airframe noise using microphone arrays in open and closed wind tunnels," National Aerospace Laboratory NLR, Report, 2007.
- [3] M. Remillieux, "Aeroacoustic Study of a Model-Scale Landing Gear in a Semi-Anechoic Wind-Tunnel," MSc Thesis, Department of Mechanical Engineering, Virginia Polytechnic Institute and State University, 2007.
- [4] A. Bale, "The Application of MEMS Microphone Arrays to Aeroacoustic Measurements, MASc Thesis, Department of Mechanical Engineering, University of Waterloo, 2011.
- [5] S. A. McNerny and S. M. Olcmen, "High-intensity rocket noise: Nonlinear propagation, atmospheric absorption, and characterization," *The Journal of the Acoustical Society of America*, vol. 117, pp. 578-591, February 2005.
- [6] P. R. Scheeper, B. Nordstrand, J. O. Gullv, L. Bin, T. Clausen, L. Midjord, and T. Storgaard-Larsen, "A new measurement microphone based on MEMS technology," *Microelectromechanical Systems, Journal of*, vol. 12, pp. 880-891, 2003.
- [7] S. Hansen, N. Irani, F. L. Degertekin, I. Ladabaum, and B. T. Khuri-Yakub, "Defect imaging by micromachined ultrasonic air transducers," in *Ultrasonics Symposium Proceedings*, pp. 1003-1006 vol.2, 1998.
- [8] T. Lavergne, S. Durand, M. Bruneau, N. Joly, and D. Rodrigues, "Dynamic behavior of the circular membrane of an electrostatic microphone: Effect of holes in the backing electrode," *The Journal of the Acoustical Society of America*, vol. 128, pp. 3459-3477, 2010.
- [9] V. Magori and H. Walker, "Ultrasonic Presence Sensors with Wide Range and High Local Resolution," *Ultrasonics, Ferroelectrics and Frequency Control, IEEE Transactions on*, vol. 34, pp. 202-211, 1987.
- [10] P. R. Scheeper, A. G. H. D. v. der, W. Olthuis, and P. Bergveld, "A review of silicon microphones," *Sensors and Actuators A: Physical*, vol. 44, pp. 1-11, 1994.

- [11] R. Schellin and G. Hess, "A silicon subminiature microphone based on piezoresistive polysilicon strain gauges," *Sensors and Actuators A: Physical*, vol. 32, pp. 555-559, 1992.
- [12] M. Sheplak and J. Dugundji, "Large Deflections of Clamped Circular Plates Under Initial Tension and Transitions to Membrane Behavior," *Journal of Applied Mechanics*, vol. 65, pp. 107-115, March 1998.
- [13] M. Rossi, "Chapter 5, 6," in *Acoustics and Electroacoustics*, Artech House, Inc., 1988.
- [14] S. D. Senturia, "Chapter 1, 17," in *Microsystem Design*, Kluwer Academic Publishers, 2001.
- [15] D. Martin, "Design, fabrication, and characterization of a MEMS dual-backplate capacitive microphone," Ph.D Thesis, Department of Electrical and Computer Engineering, University of Florida, 2007.
- [16] S. T. Hansen, A. S. Ergun, W. Liou, B. A. Auld, and B. T. Khuri-Yakub, "Wideband micromachined capacitive microphones with radio frequency detection," *The Journal of the Acoustical Society of America*, vol. 116, pp. 828-842, August 2004.
- [17] D. P. Arnold, S. Gururaj, S. Bhardwaj, T. Nishida, and M. Sheplak, "A piezoresistive microphone for aeroacoustic measurements," in *Proceedings of International Mechanical Engineering Congress and Exposition*, pp. 281-288, 2001.
- [18] M. Sheplak, K. S. Breuer, and Schmidt, "A wafer-bonded, silicon-nitride membrane microphone with dielectrically-isolated, single-crystal silicon piezoresistors," in *Technical Digest. Solid-State Sensor and Actuator Workshop . Transducer Res*, Cleveland, OH, USA, pp. 23-26, 1998.
- [19] S. Horowitz, T. Nishida, L. Cattafesta, and M. Sheplak, "A micromachined piezoelectric microphone for aeroacoustics applications," in *Proceedings of Solid-State Sensor and Actuator Workshop*, 2006.
- [20] M. D. Williams, B. A. Griffin, T. N. Reagan, J. R. Underbrink, and M. Sheplak, "An AlN MEMS Piezoelectric Microphone for Aeroacoustic Applications," *Microelectromechanical Systems, Journal of*, vol. 21, pp. 270-283, 2012.
- [21] J. Hillenbrand and G. M. Sessler, "High-sensitivity piezoelectric microphones based on stacked cellular polymer films (L)," *The Journal of the Acoustical Society of America*, vol. 116, pp. 3267-3270, 2004.

- [22] K. Kadirvel, R. Taylor, S. Horowitz, L. Hunt, M. Sheplak, and T. Nishida, "Design and Characterization of MEMS Optical Microphone for Aeroacoustic Measurement," in *42nd Aerospace Sciences Meeting & Exhibit*, Reno, NV, 2004.
- [23] Z. J. Zhou, L. Rufer, and M. Wong, "Aero-acoustic microphone with layer-transferred single-crystal silicon piezoresistors," in *Solid-State Sensors, Actuators and Microsystems Conference, TRANSDUCERS 2009. International*, pp. 1916-1919, 2009.

# Chapter 2: MEMS Sensor Design and Finite Element

## Analysis

For MEMS sensor design, basic material properties, such as Young's modulus, density and residual stress, are important. The density decides the total mass of the sensing diaphragm, and Young's modulus and residual stress decide the effective spring constant of the sensing diaphragm. The total mass and the effective spring constant then fix the first mode resonant frequency of the sensor. In this chapter, first, techniques and methods to accurately measure these material properties are introduced. Then, design considerations based on different fabrication techniques are described, and finally, the design parameters are presented and each design is simulated using the finite element analysis (FEA) method.

### 2.1 Key Material Properties

#### 2.1.1 Diaphragm Material Residual Stress

After the thin film deposition process, normally, the film will contain residual stress, which is mostly caused either by the difference of the thermal expansion coefficient between the thin film and the substrate or by the material property differences within the interface between the thin film and the substrate, such as the lattice mismatch. The first of these is called thermal stress and the latter is called intrinsic stress.

In 1909, Stoney [1] found that after deposition of a thin metal film on the substrate, the film-substrate system would be bent due to the residual stress of the deposited film (Figure 2.1). Then he gave the well-known formula in Equation 2.1 to calculate the thin film stress based on the measurement of the bending curvature of the substrate, where  $\sigma$  is the thin film residual stress,  $E_s$  is the substrate material Young's modulus,  $d_s$  is the substrate thickness,  $d_f$  is the thin film thickness,  $\nu_s$  is the substrate material Poisson's ratio and  $R$  is the bending

curvature.

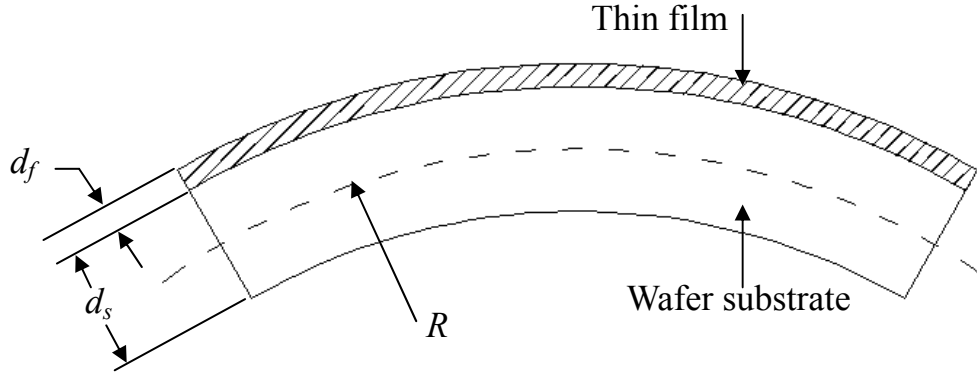


Figure 2.1: Bending of the film-substrate system due to the residual stress.

$$\sigma = \frac{E_s d_s^2}{6R(1-\nu_s)d_f} \quad (2.1)$$

For the stress measurement experiment, before the thin film deposition process, the initial curvatures of two P-type (100) bare silicon wafers are measured as  $R_i$ . As will be described in Chapter three, the sensing diaphragm material used in the fabrication process is low-stress silicon nitride (LS-SiN) film. So, on one wafer, a  $0.5\mu\text{m}$  thick LS-SiN film is deposited, and on the other wafer, a  $1\mu\text{m}$  thick film is deposited. The backside nitride materials on both wafers are etched away through a reactive ion etching (RIE) process. Then the bending curvature of the wafer after thin film deposition is measured as  $R_d$ . The curvature  $R$  in Equation 2.1 is calculated by  $R = R_d - R_i$ . Table 2.1 presents the value used in Equation 2.1 for calculation and the result of the calculated residual stress.

$E_s$ (GPa)	$\nu_s$	$d_s$ ( $\mu\text{m}$ )	$d_f$ ( $\mu\text{m}$ )	$R$ (m)	$\sigma$ (MPa)
185	0.28	525	0.5	143.1	165
185	0.28	525	1	55.2	214

Stoney formula is based on the assumption that  $d_f \ll d_s$ , and the calculated result is an average value of the stress within the whole wafer. Rotational beam method [2] is another

commonly used technique to measure the thin film residual stress, and the advantage of this method is that the stress value can be measured locally. Figure 2.2 presents the layout of a single die of the microphone chip. At the center of the die, two rotational beam structures (marked within the black dashed line) are placed perpendicularly to measure the residual stress in both the x and y directions.

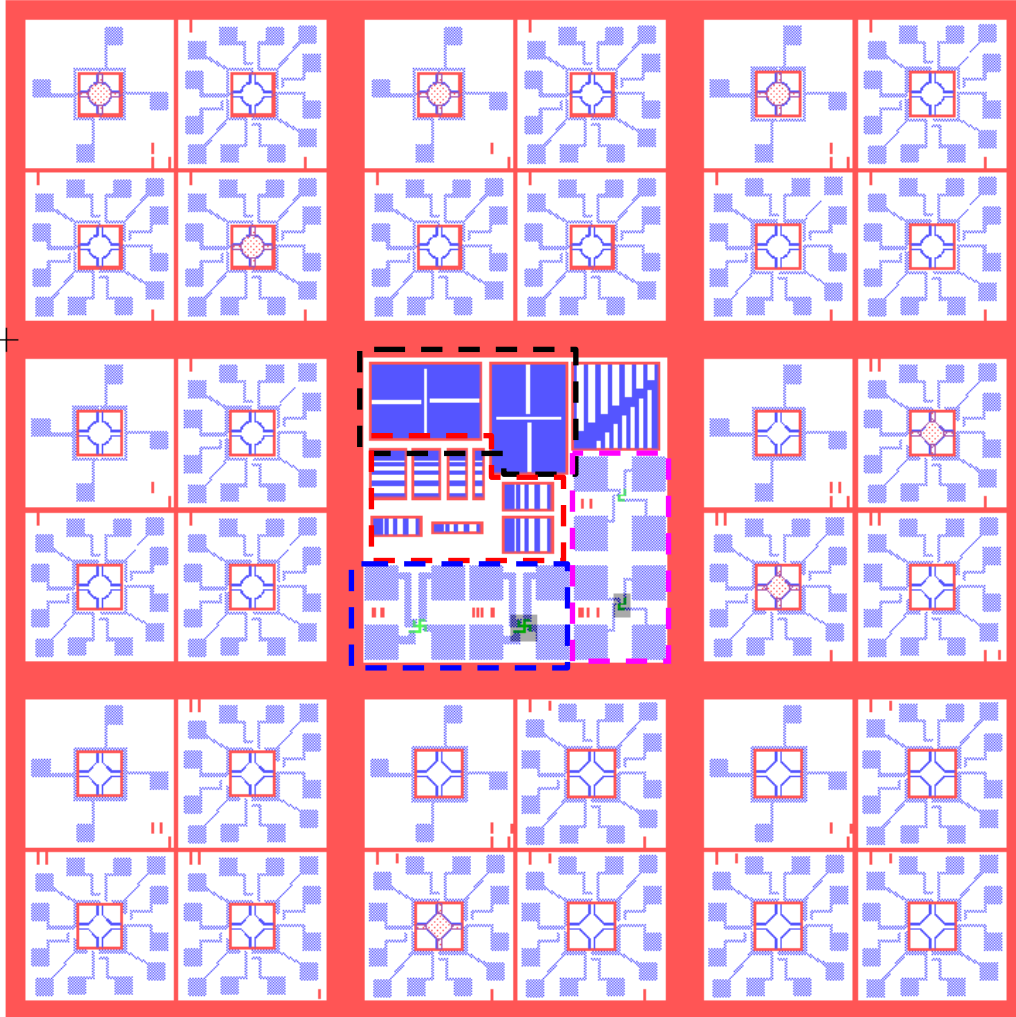


Figure 2.2: Layout of a single die.

The details of the rotational beam structures are shown in Figure 2.3. With the design parameters listed in Table 2.2, the residual stress calculation equation is

$$\sigma = \frac{E\delta}{6490} (MPa), \quad (2.2)$$

where  $E$  is the beam material Young's modulus and  $\delta$  is the beam rotation distance under



stress. The drawback of this method is obviously that unless we know the beam material Young's modulus very well, the calculated residual stress value is not accurate. In section 2.1.2, the method to measure the material Young's modulus will be introduced and here we will directly use the measured value 207 GPa to calculate the residual stress. Figure 2.4(a and b) presents two typical results of two structures rotated after releasing. The rotation distances are 5.5 and 4 $\mu\text{m}$  and the corresponding residual stresses are 175MPa and 128MPa for 1 $\mu\text{m}$  and 0.5 $\mu\text{m}$  thick LS-SiN material, respectively. The residual stress values measured by rotational beam method are about 20% less than the values measured by the curvature method. This phenomenon is also observed by Mueller et al. [3], and the reason for it is the stiction between the indicating beam of the rotating structure and the substrate, which causes the beams to not be in their equilibrium state when they are stuck down.

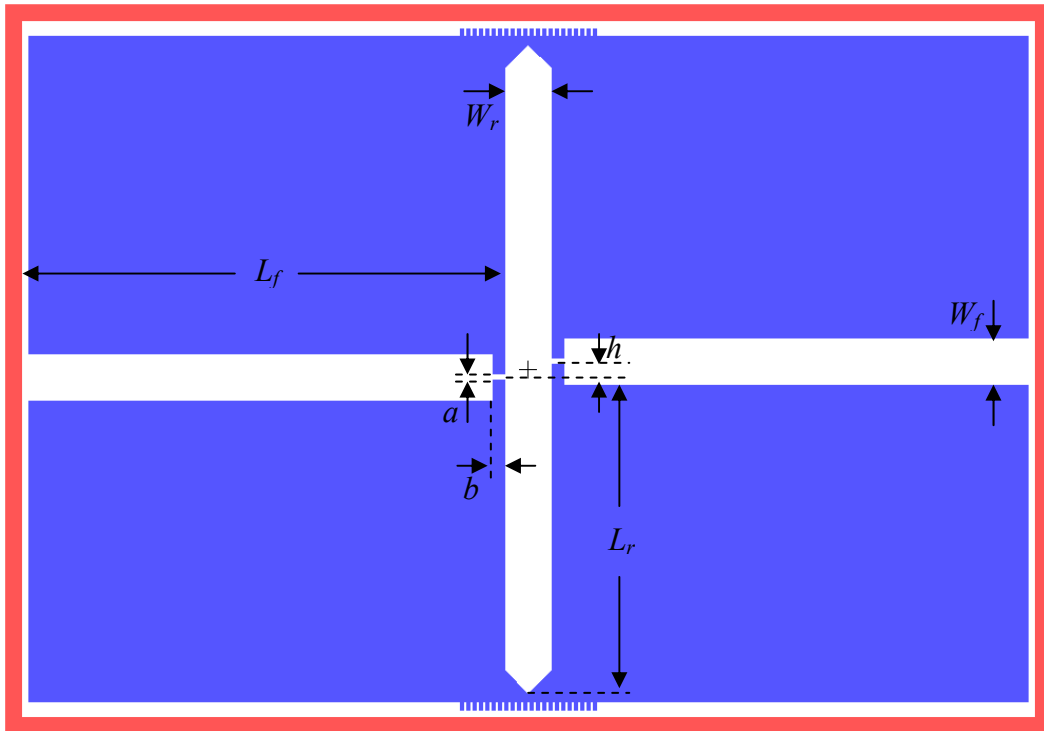
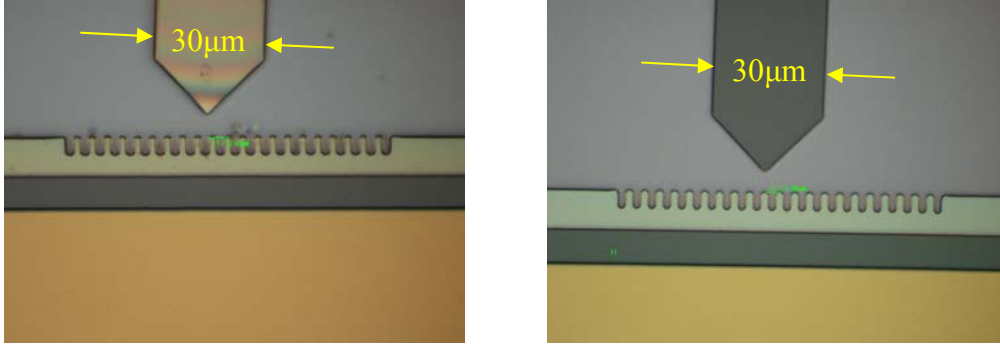


Figure 2.3: Layout of the rotational beam structure.

$W_r$ ( $\mu\text{m}$ ):	30	$W_f$ ( $\mu\text{m}$ ):	30
$L_f$ ( $\mu\text{m}$ ):	300	$L_r$ ( $\mu\text{m}$ ):	200
$a$ ( $\mu\text{m}$ ):	4	$b$ ( $\mu\text{m}$ ):	7.5
$h$ ( $\mu\text{m}$ ):	10		



(a): Rotational beam (film thickness 1.1 $\mu\text{m}$ )    (b): Rotational beam (film thickness 0.5 $\mu\text{m}$ )  
 Figure 2.4: Microphotography of two typical rotational beams after releasing.

### 2.1.2 Diaphragm Material Density and Young's Modulus

Diaphragm material density and Young's modulus are important for mechanical vibration performance estimation. The density will determine the total mass of the diaphragm and the Young's modulus will determine the spring constant. Both of these two values are indirect calculation results from the measurement of first mode resonant frequencies of doubly-clamped beam structures with different lengths.

Equation 2.3 is used to calculate the first mode resonant frequency of a doubly-clamped beam structure based on the Rayleigh–Ritz method, where  $\omega$  is the resonant frequency in the unit of rad/s;  $t$  and  $L$  are the thickness and length of the beam; and  $E$ ,  $\rho$  and  $\sigma$  are the Young's modulus, density and residual stress of the beam material, respectively [4]. As we already know the residual stress from using the methods described in the previous section, especially the average value from the curvature method, by measuring the first mode resonant frequencies  $\omega_1$  and  $\omega_2$  of two doubly-clamped beams with same cross-sectional area but different lengths  $L_1$  and  $L_2$ , the Young's modulus and density of the beam material can be expressed by Equations 2.4 and 2.5. Figure 2.5 presents the layout of different doubly-clamped beams (also marked within the red dashed line in Figure 2.2) and Table 2.3 presents the dimension of these beams.

$$\omega^2 = \frac{4\pi^4 t^2 E}{9L^4 \rho} + \frac{2\pi^2 \sigma}{3L^2 \rho} \quad (2.3)$$

$$E = \frac{3\sigma \left( \frac{1}{L_2^2} - \frac{1}{L_1^2} \frac{\omega_2^2}{\omega_1^2} \right)}{2t^2 \left( \frac{1}{L_1^4} \frac{\omega_2^2}{\omega_1^2} - \frac{1}{L_2^4} \right)} \quad (2.4)$$

$$\rho = \frac{2\sigma\pi^2}{3} \frac{L_2^2 - L_1^2}{L_2^4\omega_2^2 - L_1^4\omega_1^2} \quad (2.5)$$

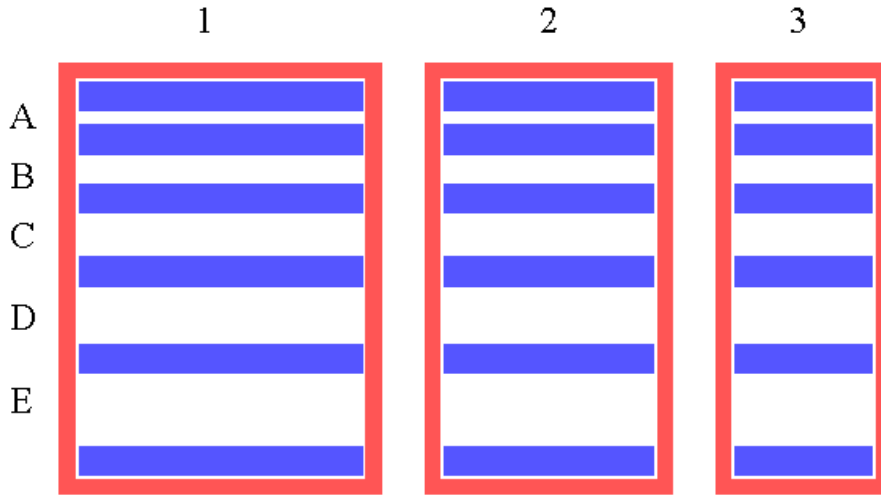


Figure 2.5: Layout of the doubly-clamped beams.

	1	2	3
A	200×10	150×10	100×10
B	200×20	150×20	100×20
C	200×30	150×30	100×30
D	200×40	150×40	100×40
E	200×50	150×50	100×50

The resonant frequency of the doubly-clamped beam is measured by a Fogale Laser vibrometer, and the setup is shown in Figure 2.6. The sample die is stuck to a piezoelectric plate with silicone (RHODORSIL™), and the piezoelectric plate is glued to a small printed circuit board (PCB) with silver conducting glue. This prepared sample is fixed to a vibration free stage using a vacuum. During the measurement, a sinusoid signal is connected to the

piezoelectric plate and the input frequency is swept within a large bandwidth from 10kHz up to 2MHz. The laser point of the vibrometer is focused at the center of the beam and the corresponding vibration displacement amplitude is recorded. A typical recorded signal is shown in Figure 2.7. The red line is the signal measured at the center of the beam and the blue line is the signal measured at the fixed point on the substrate near the beam. All measured data are shown in Table 2.4.

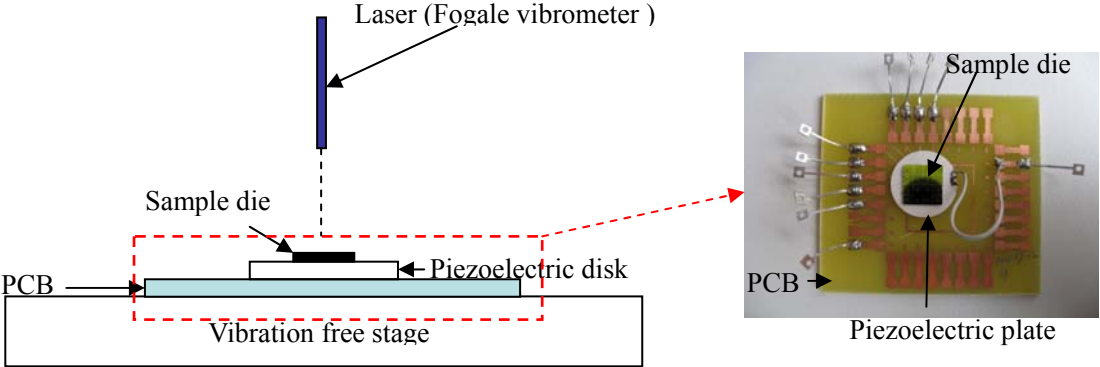


Figure 2.6: Resonant frequency measurement setup.

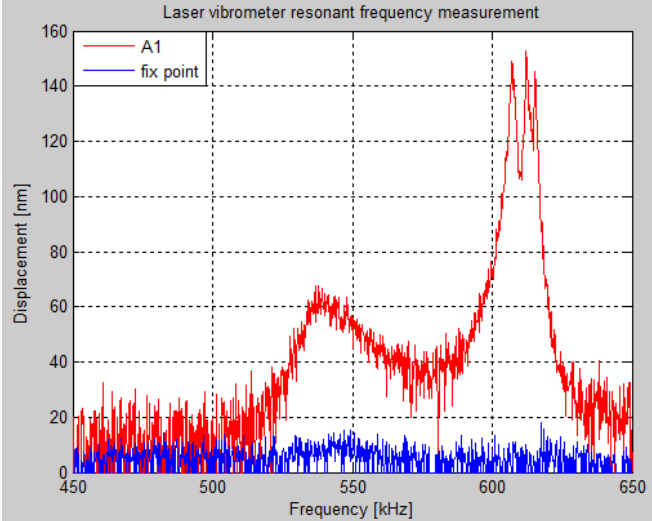


Figure 2.7: Typical measurement result of the laser vibrometer.

Table 2.4: First mode resonant frequencies of different beams (1 $\mu$ m thick).			
	1	2	3
A	607.0kHz	855.6kHz	1.511MHz
B	601.8kHz	844.4kHz	1.476MHz
C	597.6kHz	835.6kHz	1.450MHz
D	594.0kHz	833.4kHz	1.459MHz
E	596.0kHz	832.4kHz	1.449MHz

Substituting the variables in Equation 2.4 and 2.5 by using the data in Table 2.3 and Table 2.4, the calculated average density and Young's modulus of the deposited LS-SiN material are 3002kg/m<sup>3</sup> and 207GPa, respectively.

## 2.2 Design Considerations

To design a wide-band high frequency microphone, not only should the device performance specifications mentioned in Chapter one (considering the mechanical and acoustic performances) and the material properties mentioned in this chapter be considered, but also the device fabrication process's feasibility. The design of the physical structure should also accompany the design of the fabrication process.

To achieve a suspending diaphragm on top of an air cavity, generally, there exist two methods. One is to use the surface micromachining technique in which the thin film sacrificial layers are used (Figure 2.8). The diaphragm material is deposited on top of the sacrificial layers, and finally, by etching away the sacrificial layers, the diaphragm is released and suspended in the air. Another method is based on the bulk micromachining technique in which the backside silicon substrate etching is involved (Figure 2.9). Depending on whether the dry etching method or wet etching method is used, the sidewall of the backside cavity will be perpendicular to the diaphragm surface or be on an angle to the diaphragm surface.

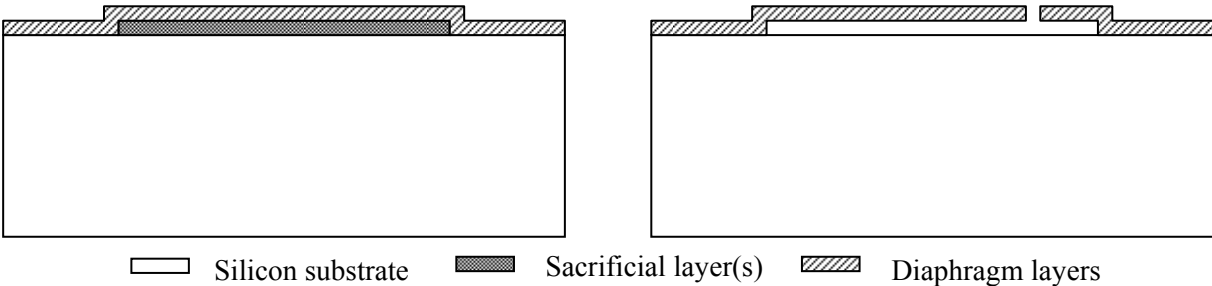


Figure 2.8: Surface micromachining technique.

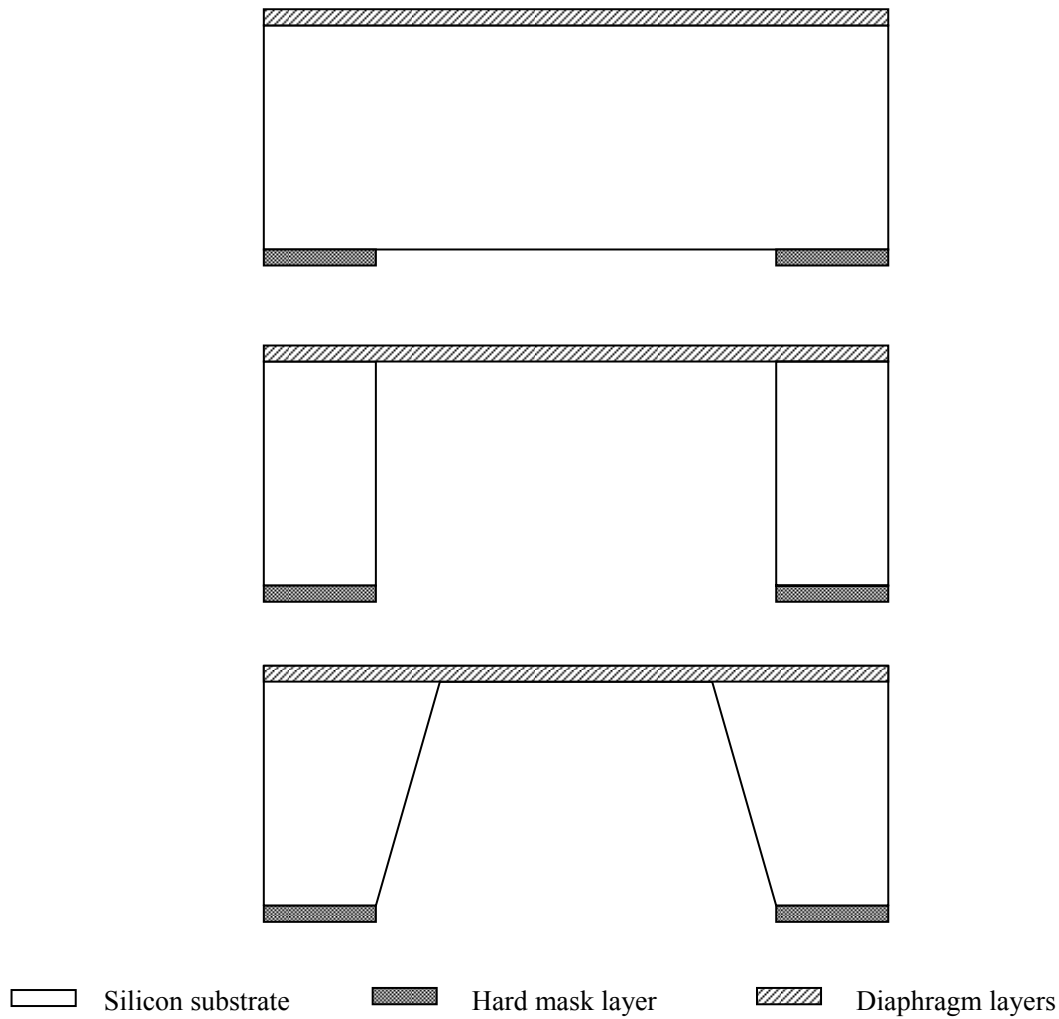


Figure 2.9: Bulk micromachining technique.

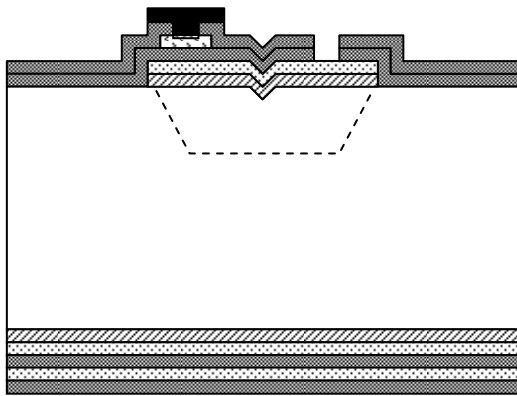
The surface micromachining and bulk micromachining techniques have their different achievable aspects and limitations for the microphone design. Figure 2.10 demonstrates a cross-section view of the physical structure of the wide-band high frequency microphone device that will be fabricated by using the surface micromachining technique. The achievable aspects are the following: (1) The dimension of the suspended sensing diaphragm could be independent with the air gap thickness below itself (the diaphragm dimension is controlled to achieve the required resonant frequency and acoustic sensitivity, and the air gap thickness is chosen to modulate the squeeze film damping effect to achieve a flat frequency response within the interested frequency bandwidth). (2) The reverse pyramidal dimple structure (the effective contact area between the diaphragm and the cavity surface is shrunk) is introduced into the sensing diaphragm to prevent the common stiction problem in the surface

micromachining fabrication process. The limitations of this technique are the following: (1) Release holes/slots will be opened on the sensing diaphragm, which leads to an acoustic short path between the ambient space and the cavity underneath the diaphragm. This acoustic short path will limit the low frequency performance of the microphone because at low frequency, any change in the pressure of the ambient space (upper-side of the sensing diaphragm) will propagate quickly into the cavity under the sensing diaphragm through the release holes/slots. Then the pressure difference is equalized. (2) Due to the possible attacking of the front-side metallization by the etching solutions, the process compatibility should be well designed. We have two choices to achieve this fabrication process: one is to form the cavity first and then do the metallization, and the other is to do the metallization first and form the cavity last. The first method would not need the consideration of the compatibility of the etching solution and the metallization system. But after forming the cavity, either photolithography or the wafer dicing would be very difficult since both of them would affect the device yield dramatically. Using the second method, the device could be released at the final stage, even after the wafer dicing, but the key point would be to find a way either to protect the metallization during the etching or make the metallization itself resistant to the etching solutions.

Figure 2.11 demonstrates a cross-section view of the physical structure of the wide-band high frequency microphone device that will be fabricated using the bulk micromachining technique. The achievable aspects are the following: (1) It is a relatively simple process, and there are less compatibility issues between the front-side metallization and the releasing chemicals. (2) Because there is a full diaphragm without holes/slots, which prevents the acoustic short path effect, the low frequency property of the microphone will be improved. The limitations of this technique are the following: (1) Due to the backside etching characteristic, the air cavity under the sensing diaphragm will be very large (air cavity thickness equal to the substrate thickness). In this situation, the squeeze film damping effect of the air cavity can be ignored and this means that the sensing diaphragm will not be damped. A high resonant peak will exist in the microphone frequency response spectrum. (2) No matter which kind of bulk micromachining technique is used (dry etching or wet etching), the lateral etching length will be proportional to the vertical etching time. This means that the non-uniformity of the

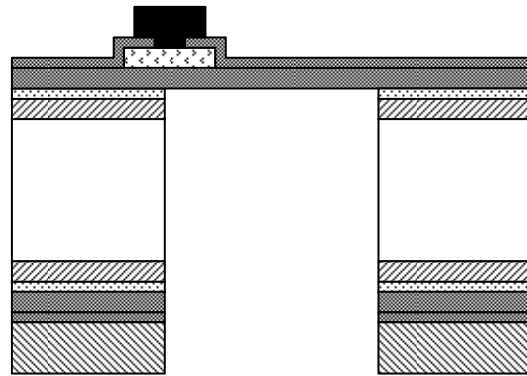


substrate thickness will lead to a diaphragm dimension variation.



- Thermal oxide
- Amorphous silicon
- MILC poly-Si
- Low stress nitride
- TiSi
- Metallization

Figure 2.10: Schematic of the microphone physical structure using the surface micromachining technique.



- P-type (100) double-side polished ~300µm wafer
- Wet oxide 0.5µm
- LS-SiN
- LTO 2µm
- a*-Si 0.1µm
- Al:Si 0.5µm
- MILC poly-Si 0.6µm

Figure 2.11: Schematic of the microphone physical structure using the bulk micromachining technique.

## 2.3 Mechanical Structure Modeling

In this section, we will discuss different mechanical structure designs and corresponding structure modeling of the aero-acoustic microphone in response to the attributes and limitations of the different fabrication techniques mentioned in the previous section.

A fully clamped square diaphragm will be adopted using the bulk micromachining technique (Figure 2.12). To model its vibration characteristics, there are two methods that can be used. One is based on the analytical calculation of the following differential equation (Equation 2.6) [5], which governs the relationship of the diaphragm displacement  $w(x, y)$  and a uniform loading pressure  $P$  :

$$D \frac{\partial^4 w}{\partial x^4} + 2H \frac{\partial^4 w}{\partial x^2 \partial y^2} + D \frac{\partial^4 w}{\partial y^4} + \sigma h \left( \frac{\partial^2 w}{\partial x^2} + \frac{\partial^2 w}{\partial y^2} \right) = P, \quad (2.6)$$

where  $D = \frac{Eh^3}{12(1-\nu^2)}$  is the flexural rigidity,  $E$  is the Young's modulus of the diaphragm,

$h$  is the diaphragm thickness,  $\nu$  is the Poisson's ratio,  $G = \frac{E}{2(1+\nu)}$  is the shear modulus,

$H = \nu D + 2 \times \frac{Gh^3}{12}$  and  $\sigma$  is the in-plane residual stress. Unfortunately, for a rigidly and fully

clamped square diaphragm, Equation 2.6 can only be solved numerically. So the second method, which is based on the FEA method will be more suitable. For a square diaphragm with a length of  $210\mu\text{m}$ , using the modeling parameters listed in Table 2.5, the simulated vibration lumped mass is  $3.95 \times 10^{-11} \text{ kg}$  and the first mode resonant frequency is  $\sim 840 \text{ kHz}$ , which is shown in Figure 2.13.

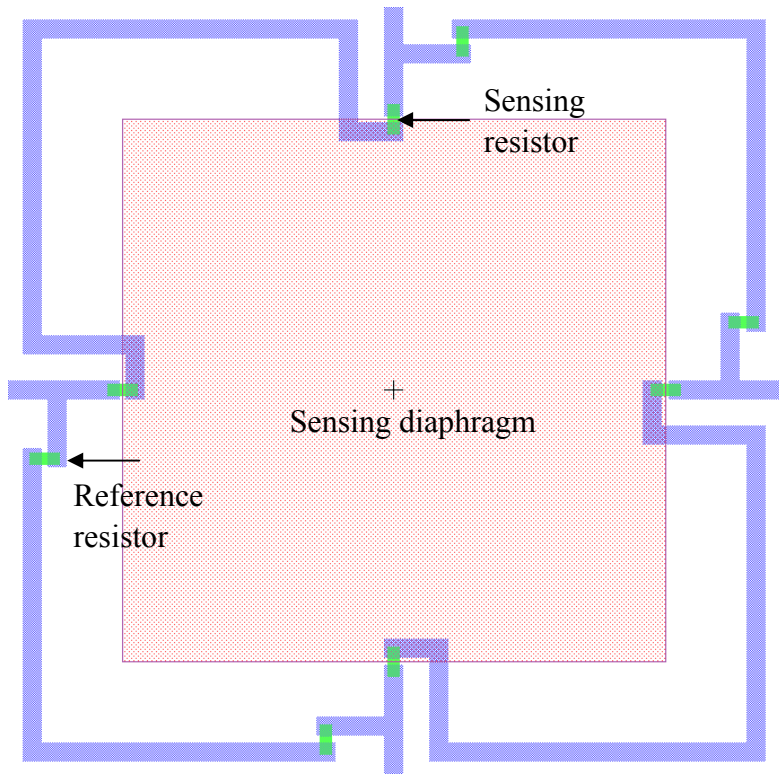


Figure 2.12: Layout of a fully clamped square diaphragm.

Table 2.5: Square diaphragm modeling parameters.			
Diaphragm length ( $\mu\text{m}$ )	210	Diaphragm thickness ( $\mu\text{m}$ )	0.5
Diaphragm density (SiN) ( $\text{kg}/\text{m}^3$ )	3002	Diaphragm Young's modulus (SiN) (GPa)	207
Poisson ratio	0.27	Residual stress (MPa)	165

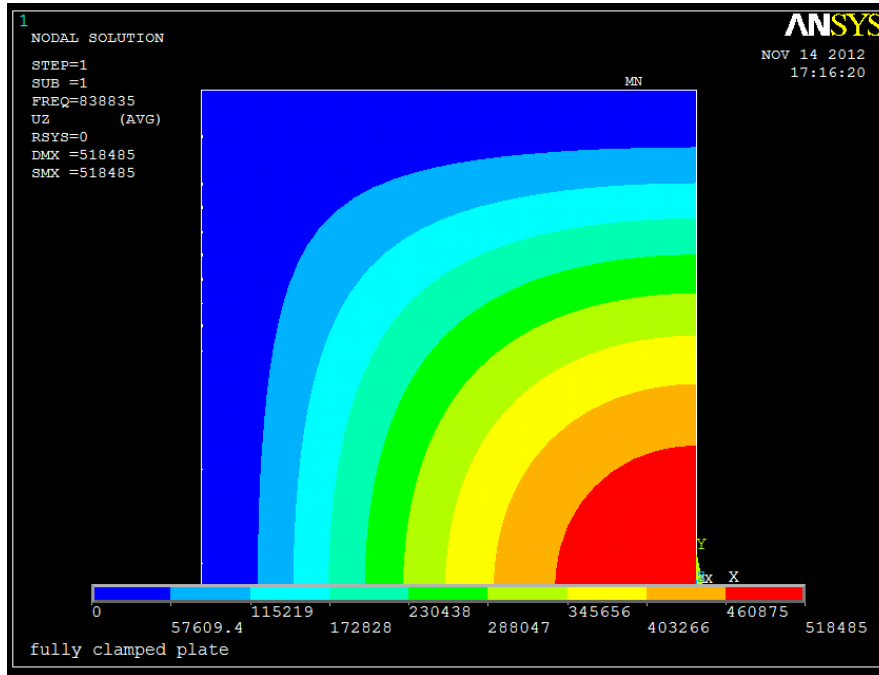


Figure 2.13: ANSYS first mode resonant frequency simulation of a square diaphragm.

Using the following equation

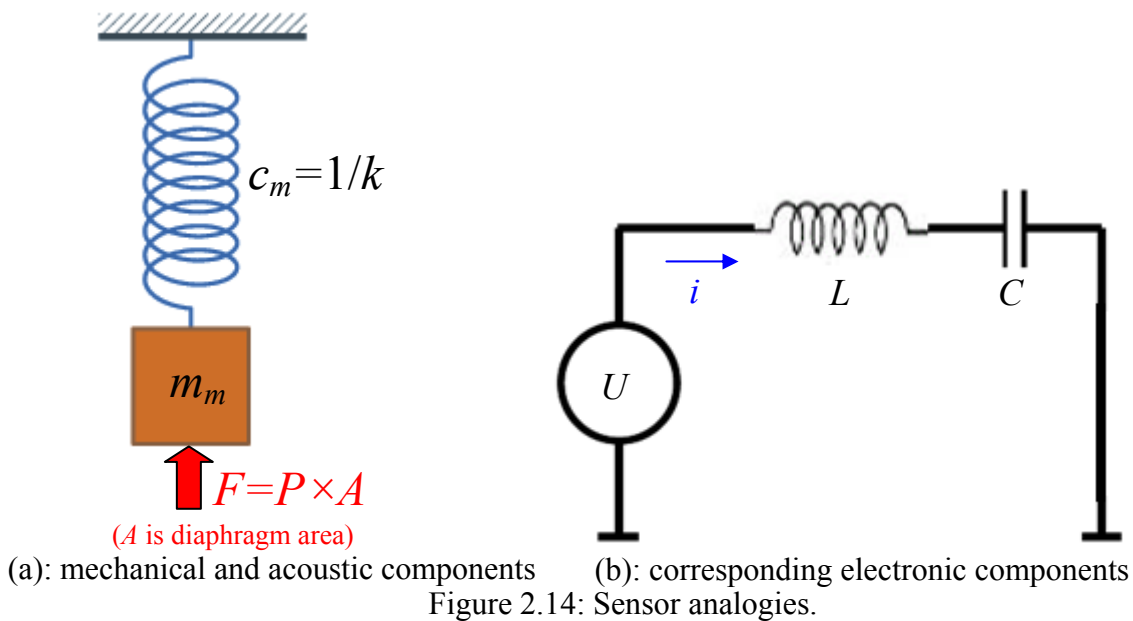
$$f_r = \frac{1}{2\pi} \sqrt{\frac{k}{m}}, \quad (2.7)$$

where  $f_r$  is the resonant frequency,  $k$  is the diaphragm effective spring constant and  $m$  is the diaphragm effective mass, the  $k$  is calculated to be 1100N/m. The mechanical frequency response of the diaphragm can be modeled by a simple one degree of freedom spring-mass system. Using electro-mechanical and electro-acoustic analogies, which are shown in Table 2.6 and Table 2.7, mechanical and acoustic variables and elements can be translated into the corresponding electronic counterparts. Then, using traditional electric circuit theory, the mechanical frequency response of the sensor can be analyzed.

Table 2.6: Variable analogy.		
Electrical	Mechanical	Acoustic
Voltage ( $U$ )	Force ( $F$ )	Pressure ( $P$ )
Current ( $i$ )	Velocity ( $v$ )	Volume velocity ( $q$ )

Table 2.7: Element analogy.		
Electrical	Mechanical	Acoustic
Inductance ( $L$ [H])	Mass ( $m_m$ [kg])	Acoustic mass ( $m_a$ [kg/m <sup>4</sup> ])
Capacitance ( $C$ [F])	Compliance ( $c_m$ [m/N])	Acoustic compliance ( $c_a$ [m <sup>5</sup> /N])
Resistance ( $R$ [ $\Omega$ ])	Mechanical resistance ( $r_m$ [kg/s])	Acoustic resistance ( $r_a$ [kg/(m <sup>4</sup> s)])

The mechanical and acoustical interpretation of the sensor is shown in Figure 2.14(a) and the corresponding electronic analogy is shown in Figure 2.14(b). When using the SI unit system,  $L = m_m$ ,  $C = c_m$  and  $U = F$ . The sensor mechanical transfer function (mechanical sensitivity in the unit of m/Pa) is defined by Equation 2.8 and using the analogies listed in Table 2.6, the mechanical transfer function can be re-written in Equation 2.9.



$$H = \frac{\text{Displacement}}{\text{Pressure}} = \frac{\int v dt}{P} = \frac{A \cdot \int v dt}{F} \quad (2.8)$$

$$H = \frac{\text{Displacement}}{\text{Pressure}} = \frac{A \cdot \int v dt}{F} = \frac{A \cdot \int i dt}{U} = A \cdot \int \frac{i}{U} dt = A \cdot \int \frac{1}{R} dt \quad (2.9)$$

Next, classical Fourier transform is applied to Equation 2.9. The integration function in the time domain is replaced by multiplying  $1/(j\omega)$  in frequency domain, where  $\omega$  is the angular frequency in the unit of rad/s and therefore, Equation 2.9 is transformed into Equation 2.10. Using this equation, the calculated mechanical frequency response of a fully clamped square diaphragm with the parameters shown in Table 2.5 is presented in Figure 2.15.

$$H(j\omega) = A \cdot \frac{1}{j\omega} \cdot \frac{1}{R} = A \cdot \frac{1}{j\omega} \cdot \frac{1}{\frac{1}{j\omega C} + j\omega L} \tag{2.10}$$

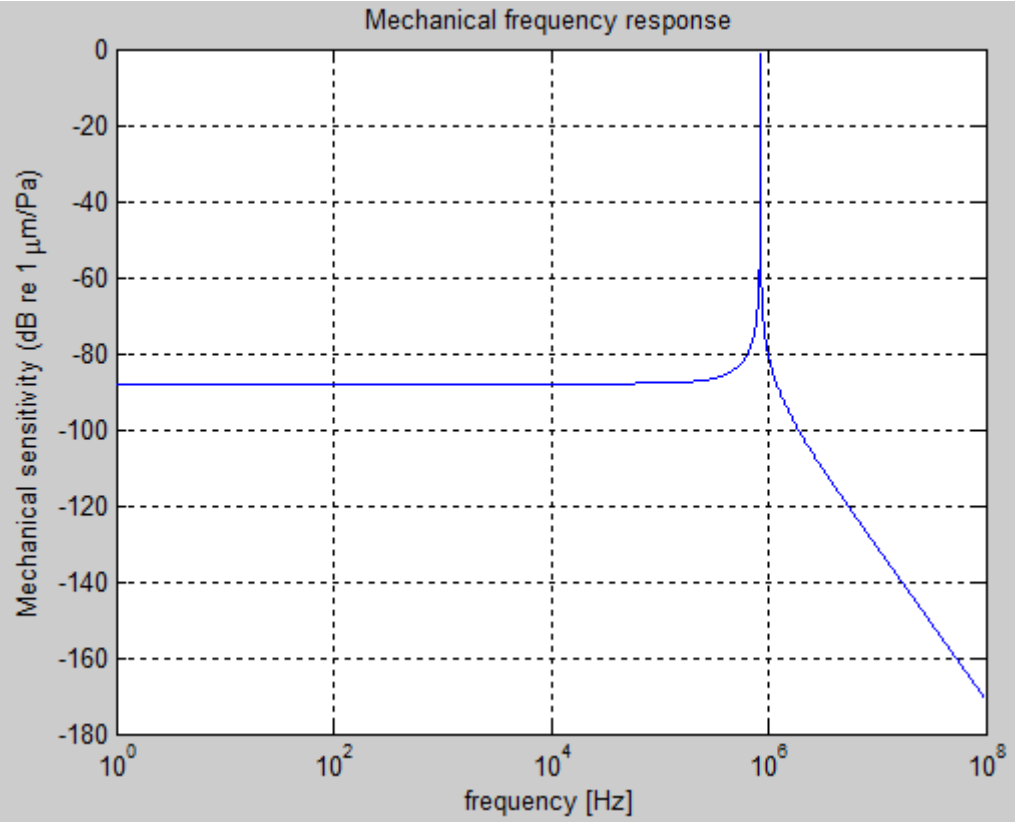


Figure 2.15: Mechanical frequency response of a square diaphragm.

Considering the surface micromachining technique, due to the required release etching slot, a square diaphragm with four supporting beam structures is used, and the etching slot surrounds the supporting beam and the diaphragm (Figure 2.16). As described in the previous section, due to the releasing slot acoustic short path effect, it is difficult to analytically model the coupled acoustic-mechanical response. In this situation, only the FEA method is applicable to modeling this complicating effect. In ANSYS, 3-D acoustic fluid element FLUID30 is used to model the fluid medium, air in our case, and the interface in the fluid-structure interaction problems; 3-D infinite acoustic fluid element FLUID130 is used to simulate the absorbing effects of a fluid domain that extends to infinity beyond the boundary of the finite element domain that is made of FLUID30 elements; and 3-D 20-node structural solid element SOLID186 is used to model the mechanical structure deformation and vibration properties.

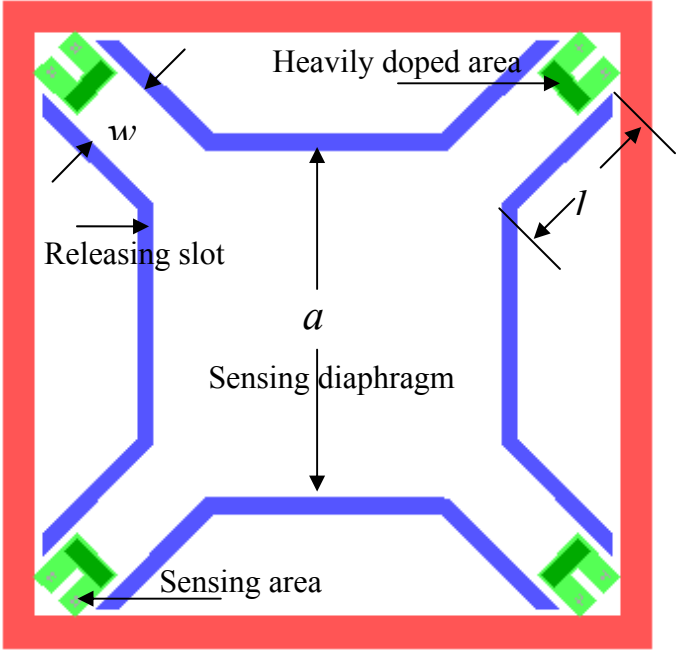


Figure 2.16: Layout of a beam supported diaphragm (reference resistors are not shown).

The detailed modeling schematic in a cross-sectional view is shown in Figure 2.17. The mechanical diaphragm is clamped at one end of the supporting beams, which are marked by the dashed red line. The clamping boundary conditions in ANSYS are set to be that the displacement in  $X$ ,  $Y$  and  $Z$  directions are all fixed to be zero. The mechanical structure is surrounded by air and the interfaces between the air and the structure (marked by the blue line)

are associated with the fluid-structure interaction boundary condition, using the ANSYS SF command with the second value being FSI. The radius of the spherical absorption surface (marked by the dashed black line) is set to be three times the diaphragm half length. And finally, the acoustic load is applied, as marked by the green line. Because the structure shape with the acoustic volume is very complicated, an automatic element sizing command SMRTSIZE is used to define the element size and, later, for automatic mesh.

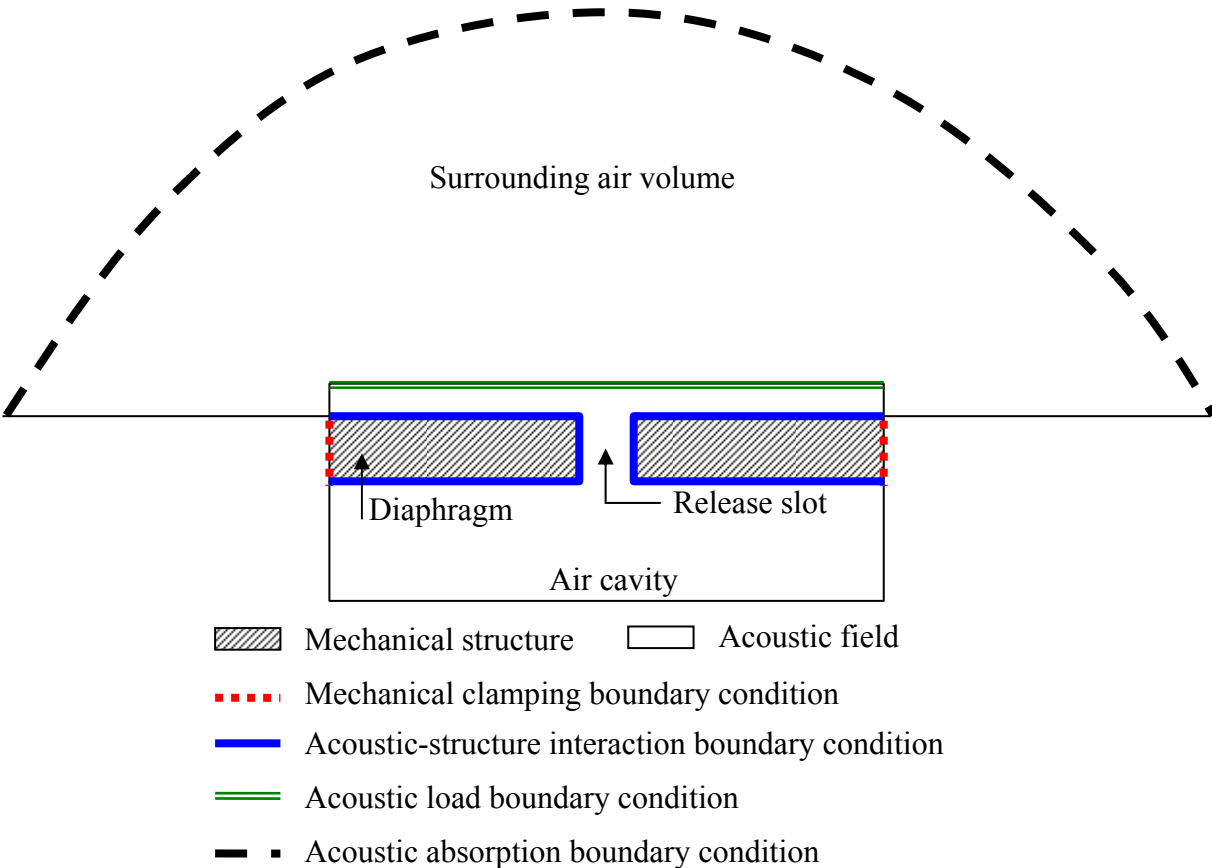


Figure 2.17: Cross-sectional view of coupled acoustic-mechanical FEA model.

The modeling parameters are listed in Table 2.8. Harmonic analysis is applied to the model by sweeping the frequency from 10Hz to 1MHz. The simulated mechanical frequency response, which shows that the first mode resonant frequency is 400kHz, is shown in Figure 2.18. Because the simulation includes the interaction between the structure and the air, part of the mechanical vibration energy is transferred to the air. This energy transfer functions like a small damper to the mechanical structure, so the structure resonant peak in Figure 2.18 is not infinity. The detailed fluid-structure interaction governing equations can be found in the



Diaphragm length ( $\mu\text{m}$ )	115	Diaphragm thickness ( $\mu\text{m}$ )	0.5
Supporting beam length ( $\mu\text{m}$ )	55	Supporting beam width ( $\mu\text{m}$ )	25
Air cavity depth ( $\mu\text{m}$ )	9	Acoustic absorption shell radius ( $\mu\text{m}$ )	345
Release slot length ( $\mu\text{m}$ )	700	Release slot width ( $\mu\text{m}$ )	5
Diaphragm density (SiN) ( $\text{kg}/\text{m}^3$ )	3002	Diaphragm Young's modulus (SiN) (GPa)	207
Poisson ratio	0.27	Residual stress (MPa)	165
Sound velocity (m/s)	340	Air density ( $\text{kg}/\text{m}^3$ )	1.225

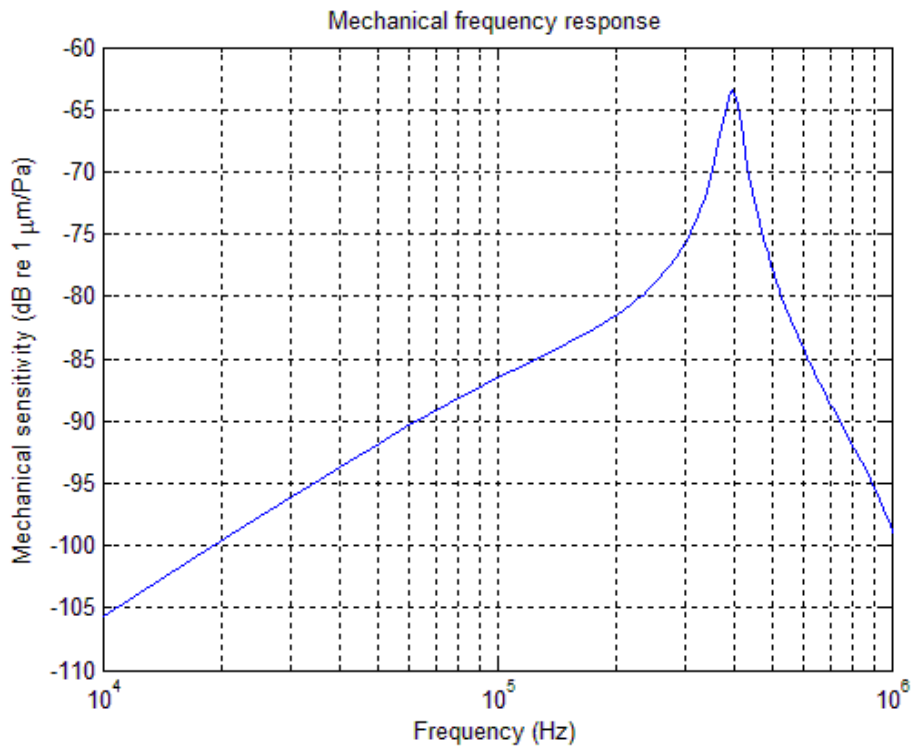


Figure 2.18: Mechanical frequency response of a beam supported square diaphragm.

## 2.4 Summary

In this chapter, firstly, techniques to measure fundamental material properties, such as residual stress, density and Young's modulus are presented. These measured values are important for the continuing design and modeling steps. Secondly, different design considerations in response to the different micromachining techniques and acoustic requirements are discussed, then, two structures, a fully clamped square diaphragm and a beam supported diaphragm, are introduced, to be fabricated by the bulk micromachining technique and the surface micromachining technique, respectively. Finally, the FEA method is used to simulate the mechanical structure vibration properties and the acoustic-structure interaction characteristics.

## 2.5 References

- [1] G. G. Stoney, "The Tension of Metallic Films Deposited by Electrolysis," *Proceedings of the Royal Society of London. Series A*, vol. 82, pp. 172-175, May 06 1909.
- [2] X. Zhang, T.-Y. Zhang, and Y. Zohar, "Measurements of residual stresses in thin films using micro-rotating-structures," *Thin Solid Films*, vol. 335, pp. 97-105, 11/19 1998.
- [3] A. J. Mueller and R. D. White, "Residual Stress Variation in Polysilicon Thin Films," *ASME Conference Proceedings*, vol. 2006, pp. 167-173, January 1, 2006.
- [4] J. Wylde and T. J. Hubbard, "Elastic properties and vibration of micro-machined structures subject to residual stresses," in *Electrical and Computer Engineering, IEEE Canadian Conference on*, pp. 1674-1679 vol.3, 1999.
- [5] R. Szilard, *Theory and Analysis of PLATES*. Engelwood Cliffs. NJ: Prentice-Hall, 1974.

## Chapter 3: Fabrication of the MEMS Sensor

MEMS microphone devices are fabricated using two techniques: surface micromachining technique and bulk micromachining technique. In this chapter, we will separately discuss these two techniques in detail. At the beginning, MILC poly-Si technology, which is used to build the piezoresistive sensing elements, will be reviewed. Then, for the surface micromachining technique, the concept of forming the cavity below the suspending sensing diaphragm will be described, and the corresponding sacrificial layers technique will be introduced. The cavity shape transition during the release process will also be analyzed. To maintain the release at the last step characteristic, a specific metallization system will be chosen and the metal to MILC poly-Si contact analysis will be described. Next, the detailed surface micromachining fabrication process for the wide-band high frequency microphone device will be presented with a cross-section view transition demonstration. Following this, the bulk micromachining technique will be introduced. Firstly, comparisons between the wet bulk micromachining technique and the dry bulk micromachining technique will be described. Then, the detailed bulk micromachining fabrication process, which is based on the deep-reactive-ion-etching (DRIE) technique, will be presented along with a cross-section view transition demonstration.

### 3.1 Review of Metal-induced Laterally Crystallized Polycrystalline Silicon Technology

Sc-Si is a very mature material in the semiconductor industry. However, due to limitations of the material and the technology, such as lattice mismatch, different thermal expansion coefficients and bonding yield, it is quite difficult or costly to integrate sc-Si material on foreign substrates, such as glass for flat panel display applications [1], or to integrate them into 3-D integrated circuits, such as in a 3-D VLSI fabrication process [2]. Sc-Si material will sometimes degrade the performance of modern MEMS devices or micro-systems, such as the

PN junction leakage problem [3].

Instead of sc-Si, *a*-Si, fabricated by low-pressure chemical-vapor-deposition (LPCVD) or plasma-enhanced chemical-vapor-deposition (PECVD) techniques is used for fabricating the thin-film-transistor (TFT) driving circuits for liquid crystal displays and photovoltaic cells integrated on glass substrate or plastic substrates. These *a*-Si deposition techniques have extended the process variety and brought new commercial products in the display and photovoltaic industries. The main drawback of the *a*-Si material is its poor field-effect mobility ( $<1\text{cm}^2/\text{V}\cdot\text{s}$  for *a*-Si:H material used in TFT-LCD application [1]). Therefore the technique to deposit crystalline silicon onto amorphous type materials has become more and more important for the semiconductor industry, and the deposited silicon grain size is a particularly pertinent consideration for the process because grain size itself may dominate electrical properties for low grain size materials [4].

In between sc-Si and *a*-Si, poly-Si is made up of small crystals, known as crystallites. It is believed to be a more desirable material compared with *a*-Si due to its much higher carrier mobility (larger than  $10\text{cm}^2/\text{V}\cdot\text{s}$ ) [5, 6]. Poly-Si material has been widely used in building the TFT circuits for large area displays; memory devices, such as dynamics random access memory (DRAM) and static random access memory (SRAM); linear image sensors; photo-detector amplifiers; printer heads and artificial fingerprints. In the 1970s, the discovery of the piezoresistive effect in poly-Si material also facilitated its application in sensing devices [7, 8]. Besides its good electrical performance, poly-Si also has good mechanical properties, which make it suitable for building mechanical structures in micro-systems [9, 10].

Poly-Si material can be deposited directly from an LPCVD furnace, a PECVD platform or re-crystallized from the *a*-Si deposited by the same techniques mentioned above. The quality of crystallized poly-Si thin films has a large effect on the performance of poly-Si devices. The defect density is generally a gauge for assessing the quality of the poly-Si material, and reducing the defect density in polycrystalline material will lead to a better performance of polycrystalline devices. In the polycrystalline material, most of the defects are generated in

the grain boundaries. Essentially, enlarging the grain size can reduce the quantity of grain boundaries and hence, can effectively promote the quality of the poly-Si material. As-deposited poly-Si generally exhibits smaller grain size than re-crystallized poly-Si and results in inferior characteristics of poly-Si devices. In the last two decades, various technologies have been proposed for *a*-Si re-crystallization on foreign materials, including solid phase crystallization (SPC), excimer laser crystallization (ELC) and metal-induced lateral crystallization (MILC).

In the SPC process, thermal annealing provides the energy required for grain nucleation and growth. In general, intrinsic solid phase crystallization needs a long duration to fully crystallize *a*-Si at a high temperature, and large defect density always exists in crystallized poly-Si. The structure of crystallized silicon film is related to the structural disorder of the amorphous state during initial deposition, and by increasing the initial disorder of the silicon network, a significant enlargement of the grain size can be achieved. Amorphous silicon deposited by using Si<sub>2</sub>H<sub>6</sub>, instead of SiH<sub>4</sub>, under the conditions of a lower temperature and higher deposition rate, observably increases the disorder of the underlying *a*-Si network. Therefore, after the SPC process, a larger grain size of the poly-Si film can be obtained by using Si<sub>2</sub>H<sub>6</sub> as a gas precursor [11]. For the intra-granular defects structure, the grains resulting from the SPC process are generally elliptical in shape and grow preferentially parallel to the <112> direction with many twins along (111) boundaries and stacking faults [12, 13].

Laser crystallization is another presently widely used method to prepare poly-Si on foreign substrates. It is a much faster process than SPC and MIC/MILC and can produce large grained poly-Si with a low dislocation density. The basic principle of laser crystallization is the transformation from amorphous to crystalline silicon by melting the silicon for a very short time. Poly-Si with large grains results from the subsequent solidification [14]. The short wavelength in the ultraviolet (output wavelengths 193, 248, and 308 nm for ArF, KrF and XeCl gas mixtures, respectively) ensures that the high laser energy will be absorbed in the thin silicon film but not in the substrate since the absorption depth is much less than the film

thickness (about 7 nm for a XeCl excimer laser radiation). In addition, due to the short excimer laser pulse length (about 30~50ns), the silicon thin film is rapidly heated above the melting point and solidifies quickly, with the heat flowing to the unheated substrate. Typical solidification time is in the order of 100ns. The time is sufficiently short that low melting substrates, such as glass (~600°C), do not have enough time to flow. Thus, ELC provides a process that is compatible with a low-temperature glass substrate as well as other temperature sensitive materials, such as plastics. Additionally, it can crystallize the film selectively by partially irradiating the film surface, so both polycrystalline state material and amorphous state material can be formed on the same substrate. Most importantly of all, the poly-Si film obtained by this technology demonstrates excellent crystallinity with few intra-granular defects due to the melt and re-growth process.

In general, the ELC process is capable of producing high-quality materials, but it suffers from low throughput and high equipment cost. On the other hand, while SPC is an inexpensive batch process, the improvement in material quality is insufficient for realizing high performance electronic devices [3]. To maintain both a high throughput and a large grain size, the seeded crystallization method was invented and can be divided into two main categories: those using semiconductor seeds, such as germanium [15, 16] and those using metals, such as Al [17], Au [18], Ag [19], Pd [20], Co [21] and Ni [22]. The metals are deposited on *a*-Si first. Then the *a*-Si is re-crystallized to poly-Si at a lower temperature than its SPC temperature. This phenomenon has been reported to contain two kinds of induced mechanism. One involves forming metal eutectic with silicon [23] and the other involves forming metal silicide [24]. For the former case, it is known that metal atoms, such as Au, Al, Sb, and In, dissolving in *a*-Si may weaken silicon bonds and so enhance the nucleation of *a*-Si. For the latter case, metals such as Pd, Ti, and Ni form a thin epitaxial metal silicide film with silicon atoms, which can act as a template for crystalline silicon (*c*-Si) nucleation. As for Ni deposited on *a*-Si, a nickel silicide (NiSi<sub>2</sub>) layer will be formed at about 400°C [25] and the inducing process started at above 450°C. The lattice constant mismatch between the NiSi<sub>2</sub> and silicon is only 0.4%, and as a result, the epitaxial NiSi<sub>2</sub> layer can easily perform as a template nucleation site for *c*-Si. Selective deposition of nickel on *a*-Si film by defining a rectangular

and circular window before depositing nickel has been investigated to induce crystallization of *a*-Si outside the metal coverage area [26]. The *a*-Si thin film right under the nickel metal was crystallized to poly-Si by a metal-induced-crystallization (MIC) process at the initial stage of annealing. Then these crystalline seeds grew laterally into the metal-free area and made large area crystallization. It has been shown that the poly-Si thin films produced by the MILC process perform largely free of residual nickel contamination and have better crystallinity, which result in an excellent electronic performance for these TFT devices.

Recently, Ni MILC has attracted lots of attention, and three stages have been identified in its crystallization process: (1) the formation of NiSi<sub>2</sub> precipitates, (2) the nucleation of *c*-Si on {111} faces of the octahedral NiSi<sub>2</sub> precipitates and (3) the subsequent migration of NiSi<sub>2</sub> precipitates and crystallization (growth) of needle-like silicon grains [1]. First the crystallization of *a*-Si is mediated by the migration of the NiSi<sub>2</sub> precipitates. In the initial stage, nucleation of *c*-Si occurs randomly at the {111} faces of an individual octahedral NiSi<sub>2</sub> precipitate. The orientation of the NiSi<sub>2</sub> precipitates within the *a*-Si determines both the orientation of the initial crystalline structure and the subsequent growth direction of the needle-like crystallites. All kinds of crystallites grow in the <111> directions, which are normal to NiSi<sub>2</sub> {111} planes. The growth of {111} faces can be explained by the fact that the surface free energy of the {111} plane in Si is lower than that of any other orientation. Also, the small lattice mismatch (0.4%) between NiSi<sub>2</sub> and silicon facilitates the formation of epitaxial *c*-Si on the {111} faces of the NiSi<sub>2</sub> precipitates. Following nucleation of crystallites on the NiSi<sub>2</sub> precipitates, needle-like *c*-Si grows at the NiSi<sub>2</sub>/*c*-Si interface as the NiSi<sub>2</sub> precipitates migrate through the *a*-Si.

The NiSi<sub>2</sub> precipitate acts as a good nucleus of silicon, which has a similar crystalline structure (the fluorite type, CaF<sub>2</sub>) to silicon and a small lattice mismatch of 0.4% with silicon. The lattice constant of NiSi<sub>2</sub>, 5.406Å, is nearly equal to that of silicon, 5.430Å. The formation process of the NiSi<sub>2</sub> precipitate strongly depends on the sample conditions, such as the Ni/silicon ratio. When a Ni film is deposited on silicon and annealed, the inter-reaction follows this sequence: Ni<sub>2</sub>Si -> NiSi -> NiSi<sub>2</sub>. The silicide formation performs sequentially,



not simultaneously, which means that the metal/silicon diffusion leads to the successive formation of the silicides, starting from the metal-rich silicide and ending up at the silicon-rich silicide.

The driving force behind precipitate migration and silicon crystallization can be described by the equilibrium free-energy diagram shown in Figure 3.1 [27]. The molar free energy curves for *a*-Si, *c*-Si and NiSi<sub>2</sub> have been drawn. The driving force for phase transformation is the reduction of free energy associated with the transformation of meta-stable *a*-Si to stable *c*-Si. The tie line drawn from both *a*-Si and *c*-Si to the NiSi<sub>2</sub> shows that, in equilibrium, NiSi<sub>2</sub> in contact with *a*-Si is expected to be silicon rich in comparison with NiSi<sub>2</sub> in contact with *c*-Si. The intersection of the tie lines with the energy axes yields the chemical potentials for Ni and silicon at the NiSi<sub>2</sub>/*c*-Si and NiSi<sub>2</sub>/*a*-Si interfaces. The chemical potential of Ni in the interfaces of NiSi<sub>2</sub>/*c*-Si is higher than that in the NiSi<sub>2</sub>/*a*-Si interfaces. This means that the Ni atoms diffused spontaneously from *c*-Si to *a*-Si.

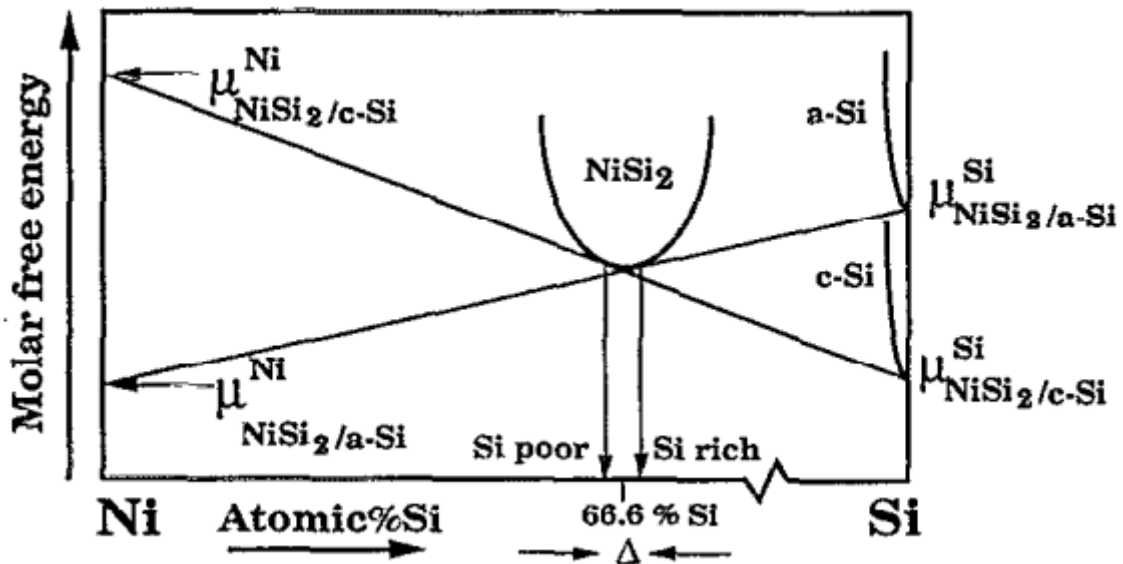
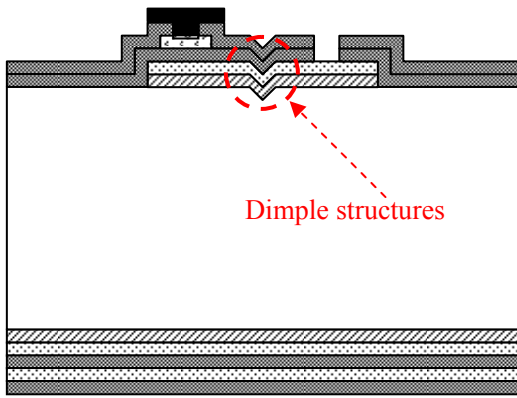


Figure 3.1: Ni/Si equilibrium free-energy diagram.

## 3.2 Surface Micromachining Process

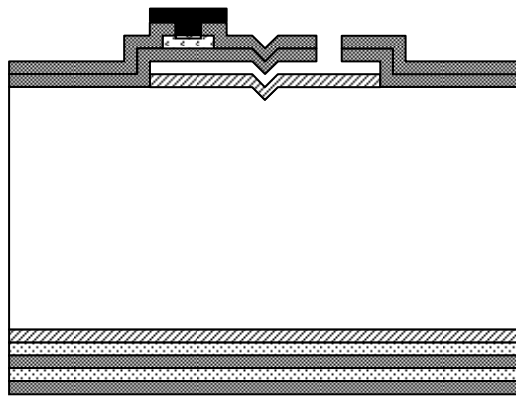
### 3.2.1 Sacrificial Materials and Cavity Formation Technology

The structure of the microphone presented in Figure 2.10 shows that under the suspending sensing diaphragm, there is an air cavity and the cavity depth should be able to be controlled separately, which means that the cavity depth is independent of the diaphragm dimension. Here, a double sacrificial layer technique was used to achieve this characteristic (Figure 3.2). The sacrificial layer system contained one layer of silicon dioxide and one layer of amorphous silicon material. During the release, the first etched sacrificial layer was the amorphous silicon material. By using the Tetramethylammonium hydroxide (TMAH) solution, which has a very high selectivity between the silicon material and the silicon dioxide material [28], after this etching, the solution will selectively stopped at the oxide layer (Figure 3.3). The TMAH solution is in the weight percentage of 20% and was heated up to 60°C in a water bath. This heating temperature was chosen to prevent diaphragm damage due to the bubbles generated during the etching reaction, but keeping as high a temperature as possible to achieve a high etching rate. The measured etching rate for amorphous silicon is  $\sim 12.7\mu\text{m}/\text{hour}$  (Figure 3.4). Then, the buffered oxide etchant (BOE) solution was used to remove the oxide sacrificial layer at room temperature. BOE solution also has a high selectivity between the silicon dioxide material and silicon material, and after this etching, the solution stopped at the substrate surface, which is the sc-Si material (Figure 3.5). Finally, the second TMAH solution was used to form the cavity shape. Due to the selectivity of the TMAH solution between the (100) and (111) crystalline facets, the etching selectively stopped at the (111) facet (Figure 3.6), and if the etching time was long enough, a reverse pyramidal cavity shape was formed.



Thermal oxide    Amorphous silicon  
 MILC poly-Si    Low stress nitride  
 TiSi    Metallization

Figure 3.2: Cross-sectional view of microphone before release.



Thermal oxide    Amorphous silicon  
 MILC poly-Si    Low stress nitride  
 TiSi    Metallization

Figure 3.3: Cross-sectional view of microphone after first TMAH etching.

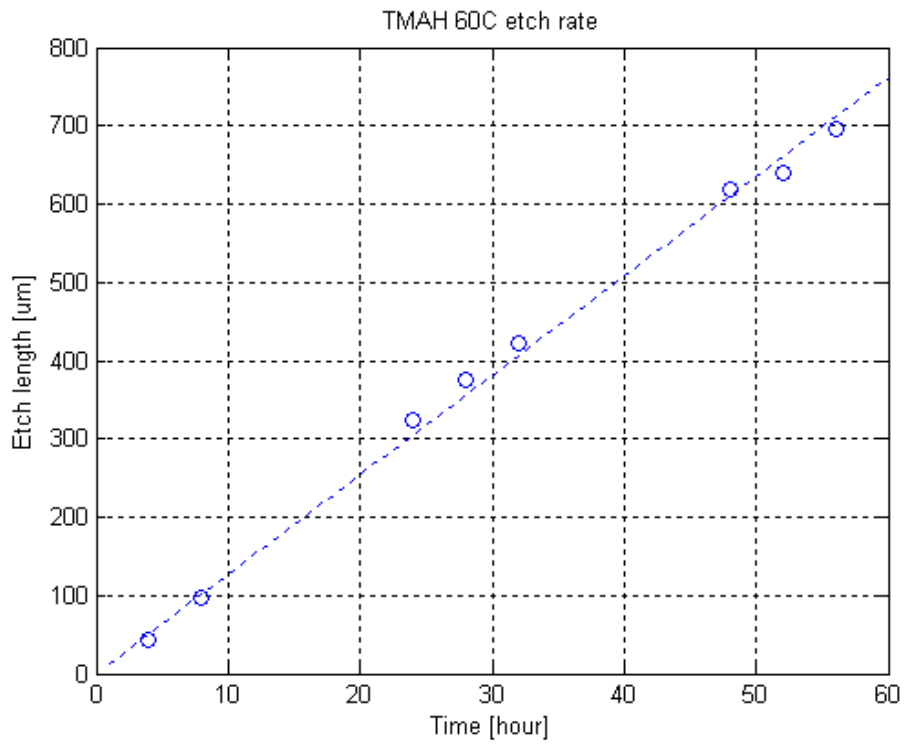
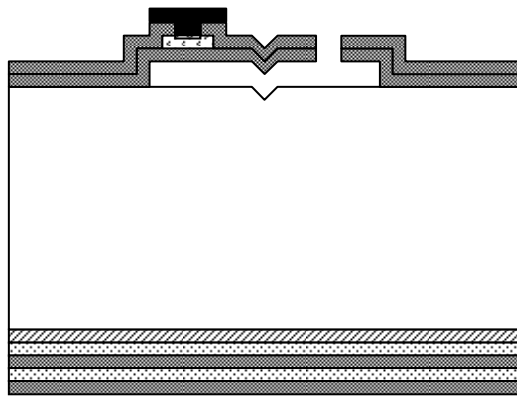


Figure 3.4: Amorphous silicon etching rate at 60°C TMAH.



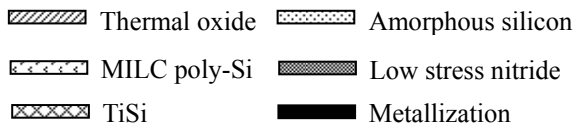
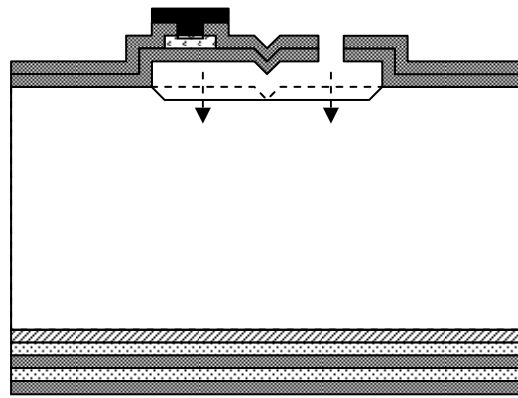


Figure 3.5: Cross-sectional view of microphone after BOE etching.






Figure 3.6: Cross-sectional view of microphone after second TMAH etching.

Room temperature BOE solution etching was not performed as what we considered that the solution will go into the chamber and etch the oxide from top to bottom quickly. The gap between the diaphragm (LS-SiN) and the oxide sacrificial layer was quite small, equal to the thickness of the amorphous silicon sacrificial layer (100nm). So the BOE solution was diffused into the space accompanied with etching the oxide layer away. Figure 3.7 is the surface profiler measurement result of the oxide sacrificial layer shape change during the BOE solution etching. Because each measurement was carried out by one specific sample and it could not be reused, since during the measurement, the diaphragm stuck to the oxide layer and could not be released any longer, the measurement result has some inconsistency. But the trend of the shape change is easy to characterize. If we define the length between the edge of the diaphragm and the edge of the remaining oxide layer to be  $L$  in Figure 3.7, then the etching length versus the etching time can be shown as in Figure 3.8.

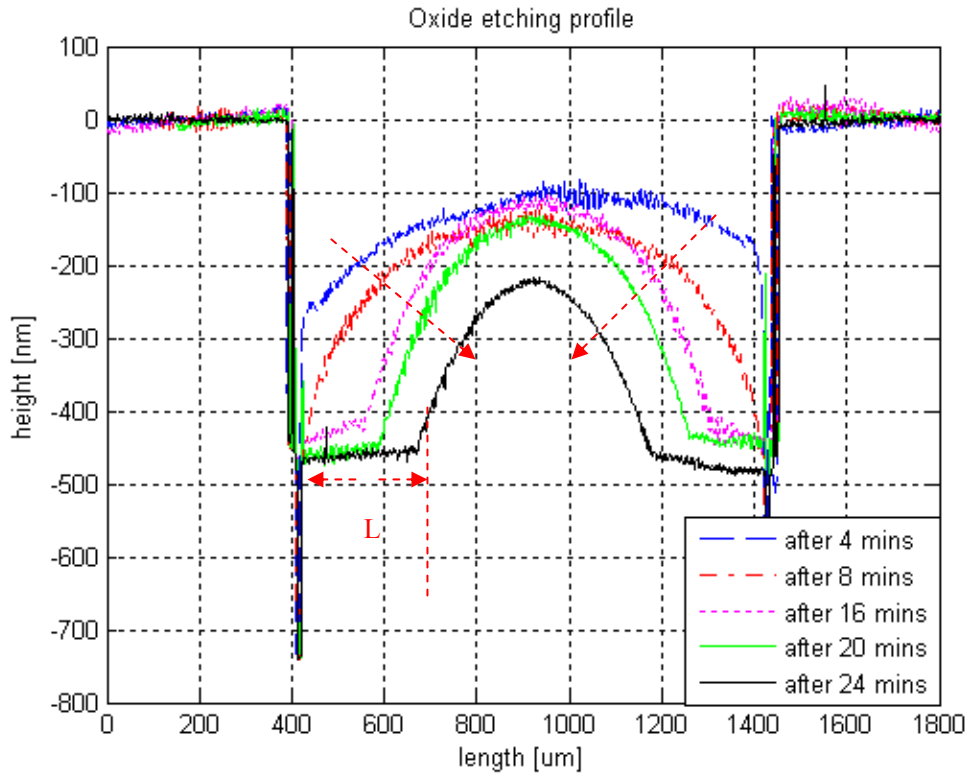


Figure 3.7: Sacrificial oxide layer etching profile.

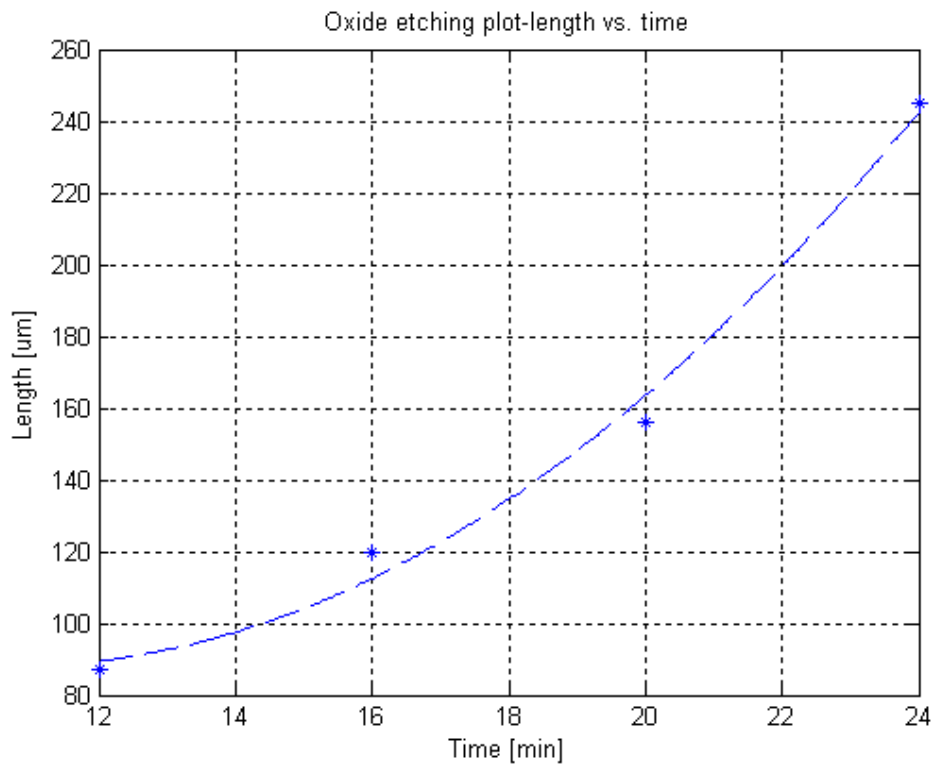
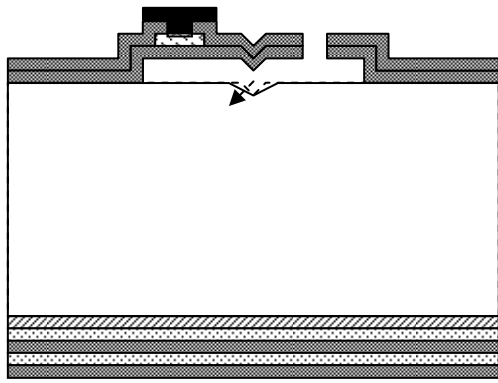


Figure 3.8: Sacrificial oxide layer lateral etching rate.

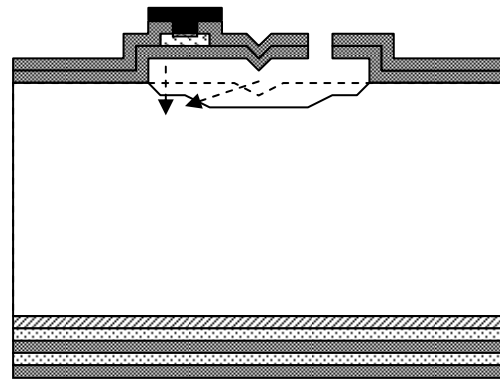
In the wide-band high frequency microphone design stage, the air cavity was used to modify the squeeze film damping effect, which requires a relative small cavity depth (in several micrometers range). This introduces the well-known stiction problem during the MEMS device release process: the two components with large surface area and small distance will be pushed together by the surface tension force of the etching solution during its drying period. Several advanced techniques are used to prevent this phenomenon, such as using a critical point dryer to dry the sample, using vapor state etching chemicals, using low surface tension solutions at the final drying stage or building some small structures on the device surface to decrease the effective surface area. We combined the last two methods and used low surface tension organic solution Isopropyl alcohol (IPA) to replace the de-ionized (DI) water and dried the sample at 110°C with a hotplate, as well as built reverse pyramidal dimple structures on the diaphragm to reduce the effective surface area (Figure 3.2). In this case, even when the surface tension force pushes the diaphragm into contact with the cavity bottom face, the contact area will be limited to the small tip areas, but not the whole diaphragm area.

However, the final etching profile is not the same as normal etching, in which the TMAH etching solution etches away the single crystalline silicon from the top surface and will not etch the (111) facet of the reverse pyramidal dimple mold (Figure 3.6). On the contrary, the real single crystalline silicon etching started at the edge of the dimple mold (Figure 3.9(a)). The dimple mold angle was quickly etched from nearly 45° to about 26°. During the etching time, the etching spread in two directions: vertically from the top surface of the silicon (100) facet and laterally from the dimple mold sidewall (Figure 3.9(b)). And finally, the etching stopped at the edge of the diaphragm (Figure 3.9(c)).



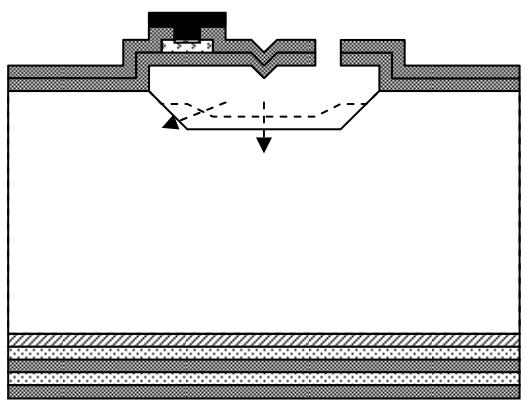
Thermal oxide   
  Amorphous silicon  
 MILC poly-Si   
  Low stress nitride  
 TiSi   
  Metallization

(a)



Thermal oxide   
  Amorphous silicon  
 MILC poly-Si   
  Low stress nitride  
 TiSi   
  Metallization

(b)

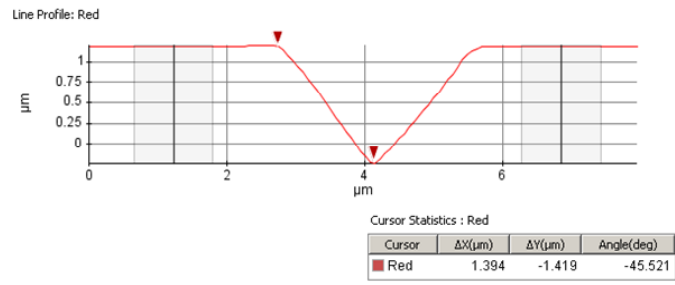
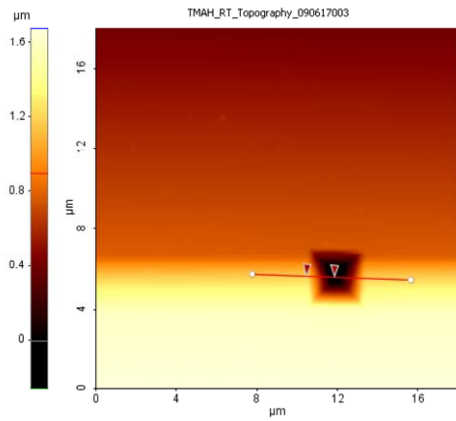


Thermal oxide   
  Amorphous silicon  
 MILC poly-Si   
  Low stress nitride  
 TiSi   
  Metallization

(c)

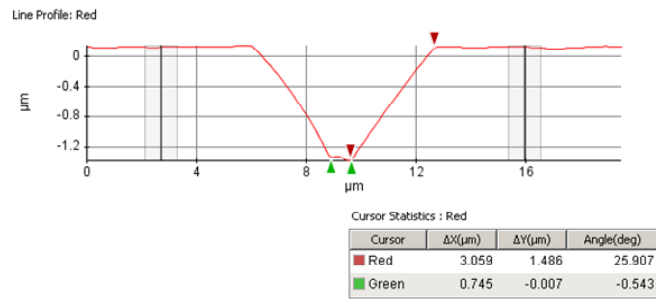
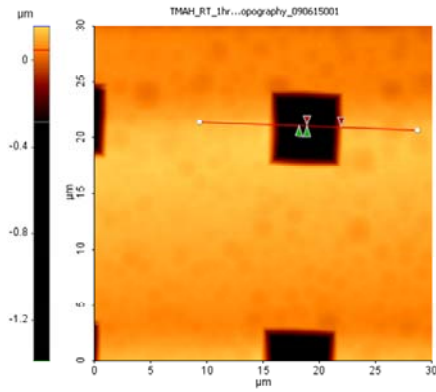
Figure 3.9: Detail of the etching profile due to the dimple mold.

An atomic force microscope was used to characterize this etching profile, especially around the dimple mold, to present the detailed etching information. Figure 3.10 presents the lateral etching information around the dimple mold. We find that the dimple mold gradually changed from a reverse pyramidal shape to a reverse trapezoid shape. The angle of the mold changed quickly from  $45^\circ$  to  $26^\circ$  and gradually changed to  $20^\circ$ , with an average of  $22.5^\circ$ .



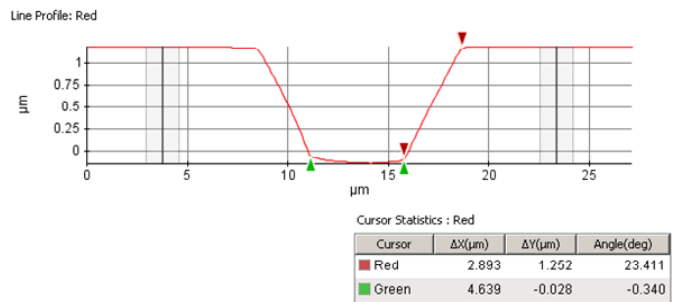
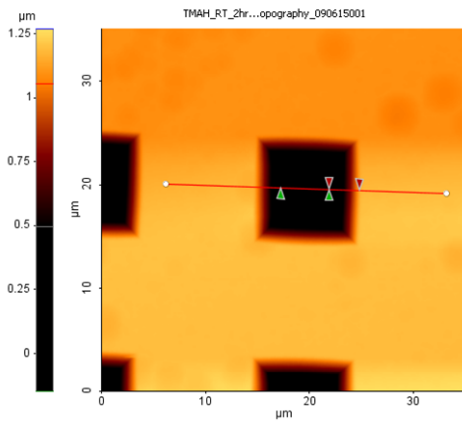
Original profile

(a): Original profile.



After 1 hour etching

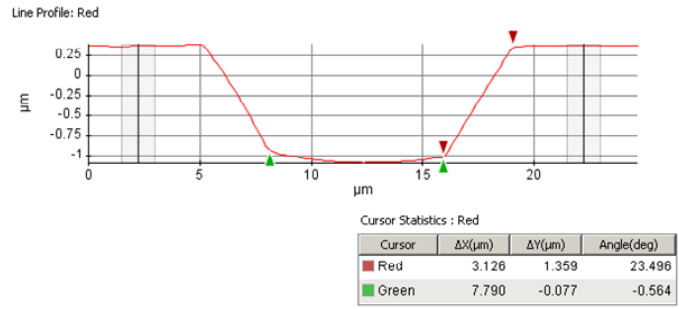
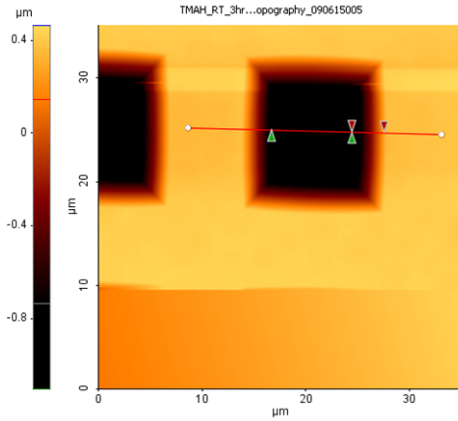
(b): Profile after 1 hour etching.



After 2 hours etching

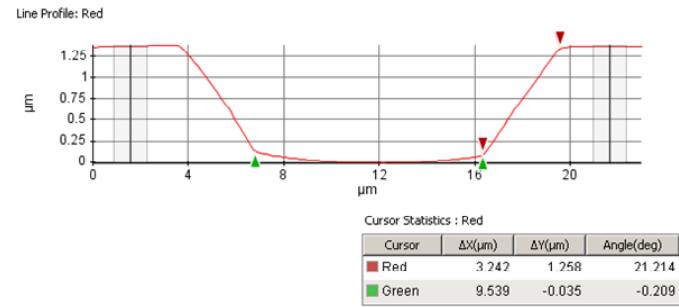
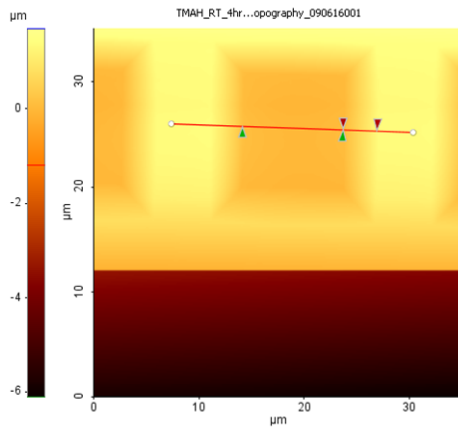
(c): Profile after 2 hours etching.





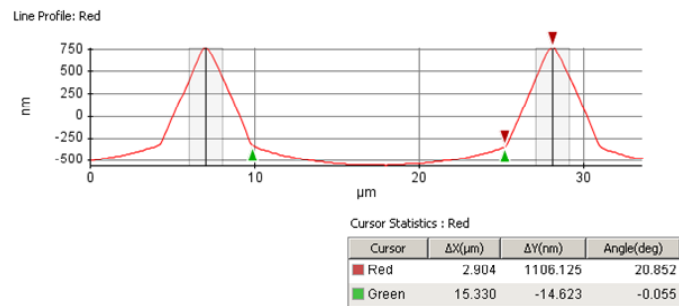
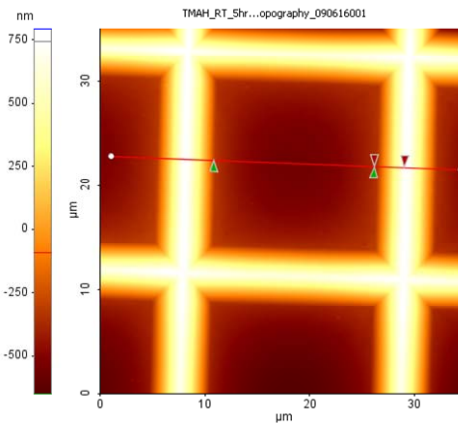
After 3 hours etching

(d): Profile after 3 hours etching.



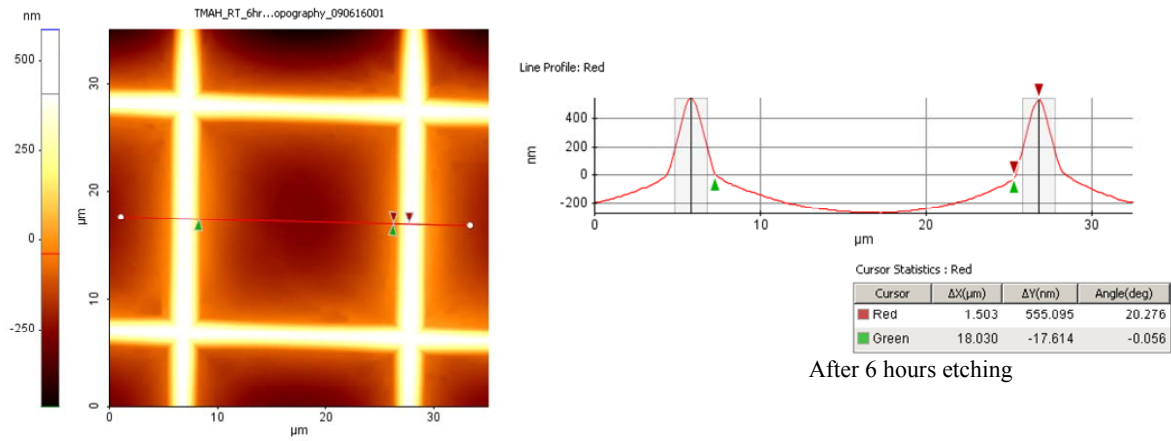
After 4 hours etching

(e): Profile after 4 hours etching.



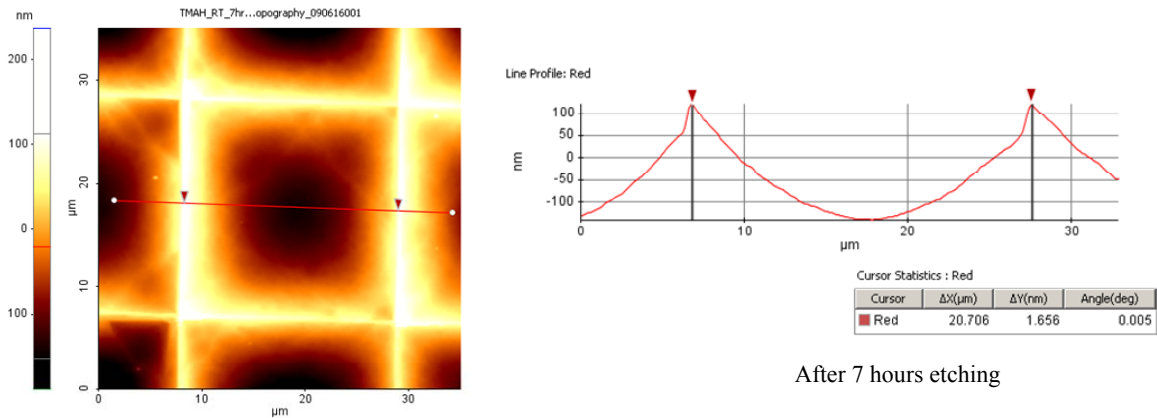
After 5.25 hours etching

(f): Profile after 5 hours etching.



After 6 hours etching

(g): Profile after 6 hours etching.



After 7 hours etching

(h): Profile after 7 hours etching.

Figure 3.10: AFM measurement of the substrate sc-silicon etching profile due to the dimple mold in room temperature TMAH solution.

The lateral etching rate ( $\sim 1.7\mu\text{m/hr}$ ) and vertical etching rate ( $\sim 0.74\mu\text{m/hr}$ ) of the sc-silicon were also measured and are shown in Figure 3.11 and Figure 3.12. One theory to explain this etching phenomenon is that the (311) facet was etched the most quickly in the TMAH solution compared with the other facets [29]. So during the etching, firstly, the (311) facet was quickly exposed and the angle between the (311) facet and the (100) facet is  $25^\circ$ , which is quite similar to the measured result of  $22.5^\circ$  on average. Then, the etching started in two directions at the same time. In the vertical direction, the TMAH etched silicon through the (100) facet from the top surface, and in the lateral direction, the TMAH etched silicon through the (311) facet. The ratio of these two etching rate is 2.29, which is quite similar to the reported result of 2.03 [29].

After releasing, the sample was put into the DI water to replace the etching solution. Then, IPA was used to replace the DI water. Finally, the sample was dried on a hotplate at 110°C to reduce the drying time.

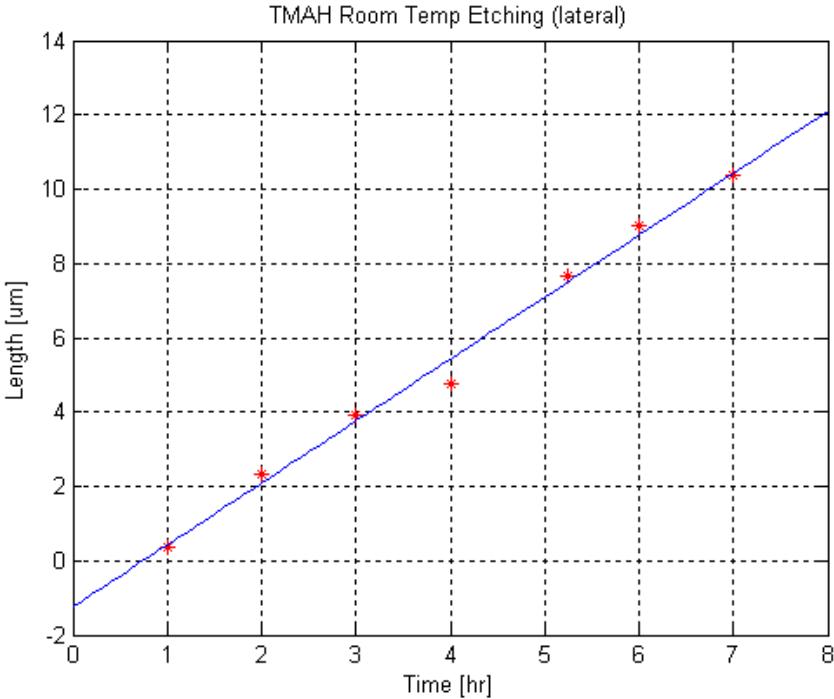


Figure 3.11: Silicon lateral etching rate of the TMAH solution at room temperature.

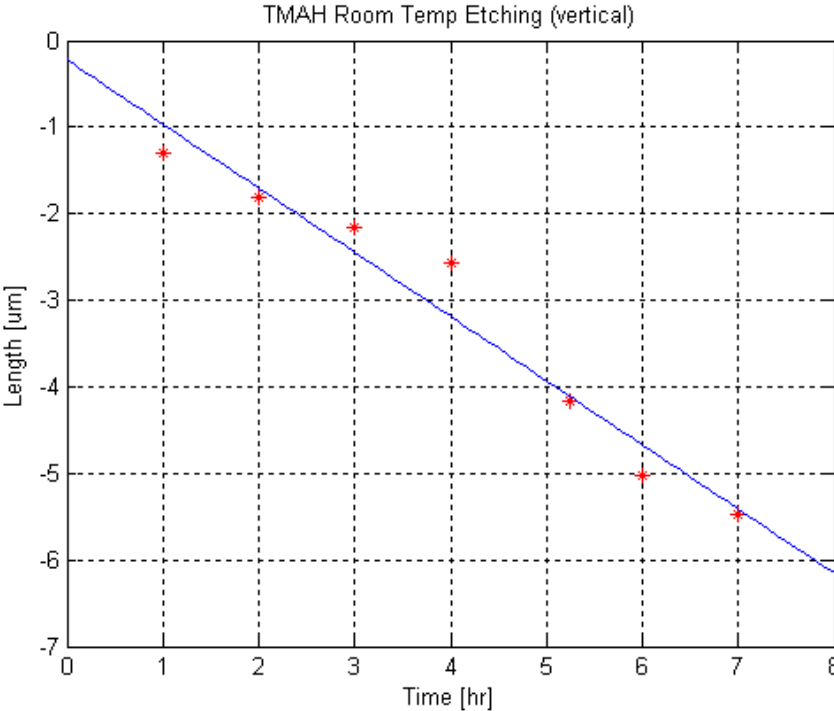


Figure 3.12: Silicon vertical etching rate of the TMAH solution at room temperature.

### 3.2.2 Contact and Metallization Technology

The metallization system used here is 50nm chromium and 1 $\mu$ m gold double metal layers, which are formed through lift-off process. This metallization system has a good adhesion to the LS-SiN layer, and both chromium and gold can resist the etching solutions, including TMAH and BOE. This characteristic is very important. It offers the capability to release the diaphragm at the final step (after metallization and wafer dicing). If the release step comes ahead of the dicing step, it will not only increase the fabrication complexity but also decrease the yield of the fabrication. This double metallization system is also thick enough to make the metal layer pinhole free, and the etching solution will not leak through the metal layer to etch the silicon piezoresistors underneath. At the same time, the gold layer will have a low resistivity. A thick chromium (1 $\mu$ m) and thin gold (0.2 $\mu$ m) combination was also tried to perform the metallization. However, thick chromium has a large residual stress, which makes the photoresist peel-off during the metal sputtering process (Figure 3.13), which is not suitable for the lift-off process.



Figure 3.13: Metal peel-off due to large residual stress.

A dual tone positive-negative inversion photoresist AZ 5200NJ was used to perform the lift-off process. The photoresist was 2.9 $\mu\text{m}$  thick if it was spin coated at 4000 revolutions per minute (rpm), which is suitable for a 1 $\mu\text{m}$  thick metal lift-off process. If this photoresist was exposed only one time, then it was developed to be a positive image of the mask, and if it was exposed two times by simply adding a flood-exposure, then it was developed to be the negative (reverse) image of the mask. Through adjusting the exposure energy of these two steps, the remaining photoresist could form a reverse trapezoid shape (Figure 3.14), which reduced the possibility of depositing metals on the sidewall of the photoresist and eased the difficulty of the thick metal lift-off process.

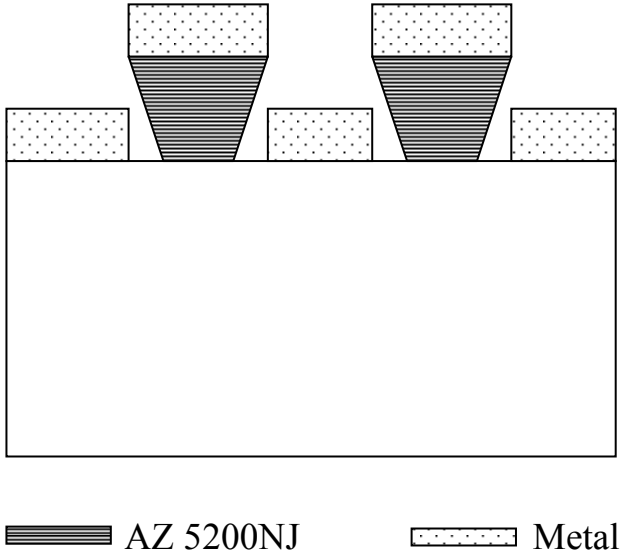


Figure 3.14: Reverse trapezoid shape of the dual tone photoresist.

One problem of this chromium and gold double layer metallization system is the schottky contact between the chromium layer and the MILC poly-Si piezoresistive material. Because the microphone works by transforming the acoustic pressure variation into the sensing resistance variation, if there is a large contact resistance between the metallization and sensing element, it is equal to introducing a large resistor in series with the sensing piezoresistor, which lowers the wide-band high frequency microphone sensitivity.

The key step to lower the contact resistance is to insert a thin titanium silicide layer in between the MILC poly-Si layer and the metallization system. This titanium silicide layer was

formed through a self-aligned two-step rapid thermal annealing technique. Firstly, 100nm titanium was deposited onto the wafer surface through a 3180 metal sputtering system (Figure 3.15). Then the first rapid thermal annealing was carried out at 560°C for 35 seconds in a nitrogen atmosphere. At this low temperature annealing, titanium and silicon formed to the high resistivity titanium silicide phase C49-TiSi<sub>2</sub> [30, 31], and titanium did not react with the silicon nitride material. Then, the un-reacted titanium was selectively removed by RCA-1 solution at 70°C, without attacking the formed titanium silicide thin layer [32, 33]. Through the second rapid thermal annealing at 800°C for 50 seconds in the nitrogen atmosphere, the titanium silicide went through phase transformation and became low resistivity phase C54-TiSi<sub>2</sub> (Figure 3.16). Before being put into the sputter machine, a 3.5 minutes HF (1:100) dipping was carried out to remove the native oxide at the titanium silicide surface and the dipping time was chosen according to the experiment results shown below (Figure 3.17). The comparison of the contact resistance between the contact system with and without insertion of the titanium silicide layer is shown in Figure 3.18, which demonstrates the improvement.

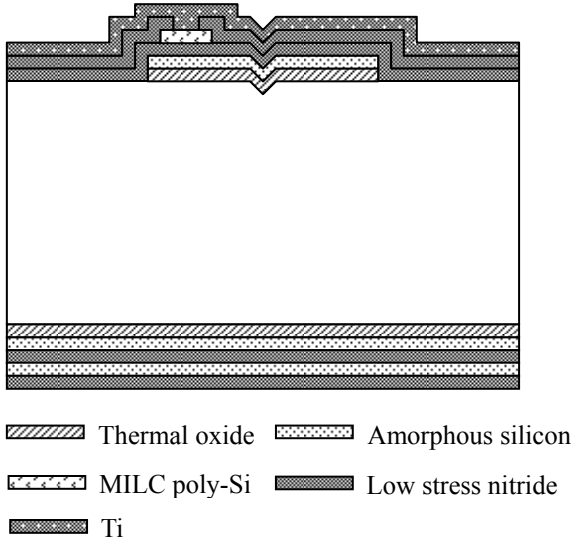


Figure 3.15: Cross-sectional view of microphone after Ti sputtering.

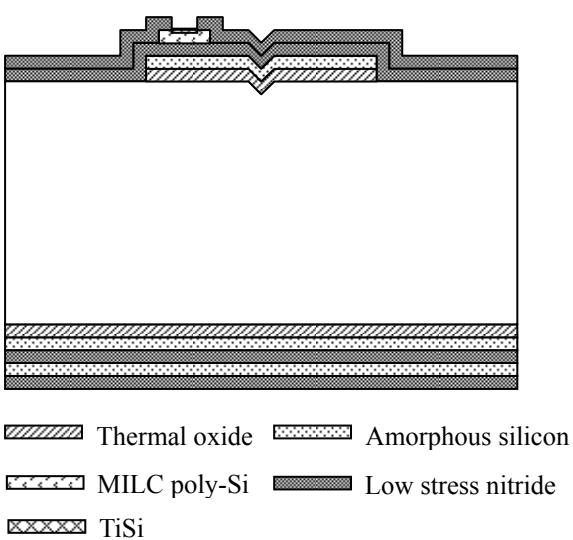


Figure 3.16: Cross-sectional view of microphone after the silicidation process.

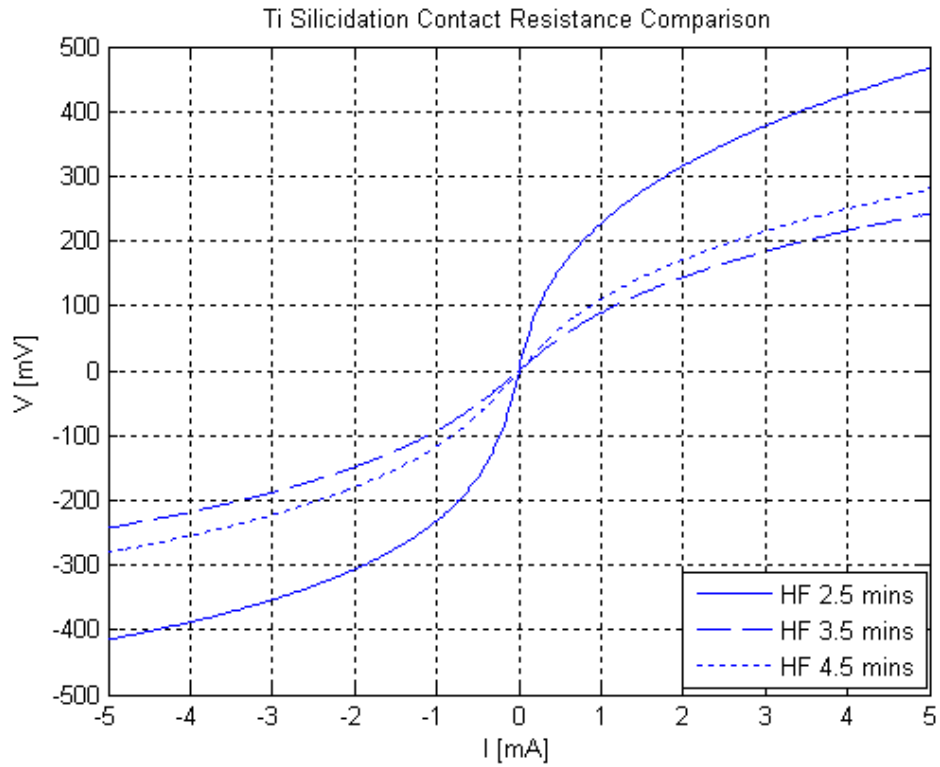


Figure 3.17: Contact resistance comparison (different HF pre-treatment time).

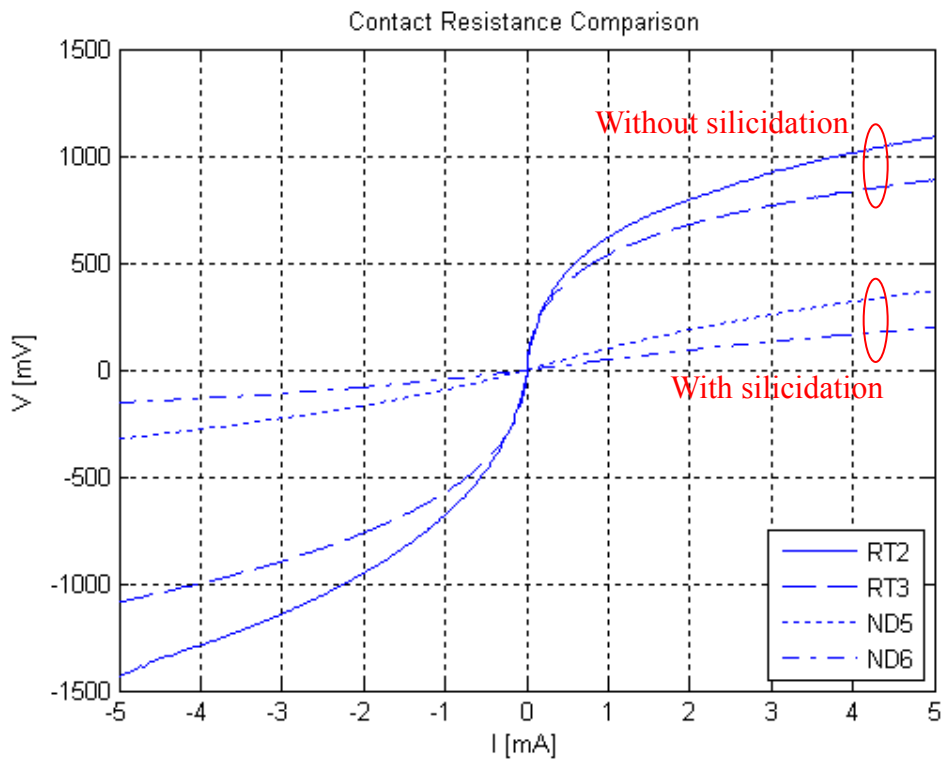
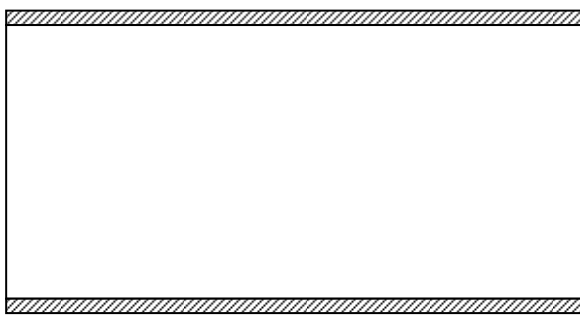


Figure 3.18: Contact resistance comparison (with/without silicidation).

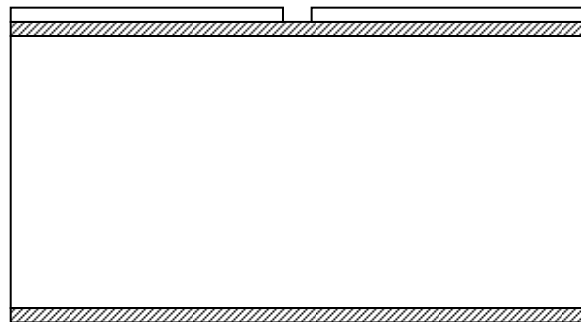
### 3.2.3 Details of Fabrication Process Flow

The whole process started from a p-type (100) silicon wafer. The first step was to form the reverse pyramidal dimple molds on the substrate surface: a 100nm thick thermal dry oxide layer was grown by furnace (Figure 3.19). Then the photolithography step was done with a “dimple” mask by photoresist HPR-504. Because HPR-504 is normally 1.3 $\mu\text{m}$  in thickness and the diameter of the dimple holes was 2 $\mu\text{m}$ , a discum process was needed to remove the possible photoresist residues in the holes (Figure 3.20). After that, BOE was used to etch the oxide hard mask layer (Figure 3.21). After stripping the photoresist by using piranha solution and rinsing with DI water, the wafers were dipped into HF (1:100) solution to remove the native oxide on the opening surface, rinsed and then directly put into TMAH solution for etching the reverse pyramidal dimple molds (Figure 3.22).



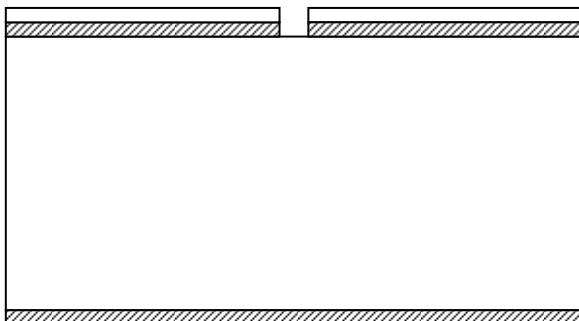
Thermal oxide

Figure 3.19: Thermal oxide hard mask.



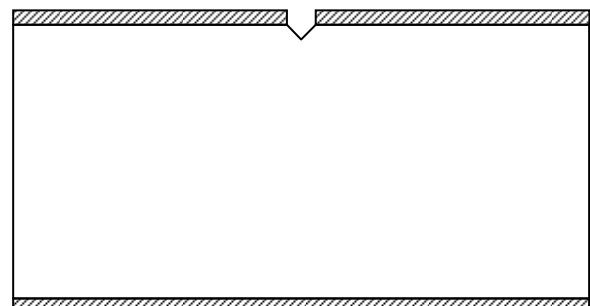
Thermal oxide HPR-504

Figure 3.20: Photolithography for dimple mold.



Thermal oxide HPR-504

Figure 3.21: Etching of thermal oxide hard mask.

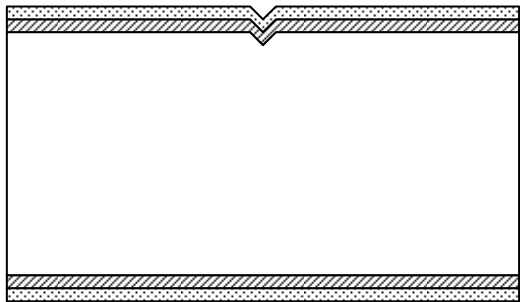


Thermal oxide

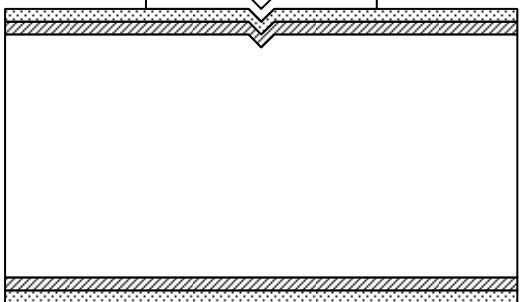
Figure 3.22: Etching of the reverse dimple mold.



The second step was to deposit and pattern the sacrificial layer. First, the thermal oxide hard mask layer was stripped by BOE solution. Then 300nm wet thermal oxide and 100nm *a*-silicon layers were grown and deposited by thermal furnace and LPCVD furnace (Figure 3.23). After this sacrificial layers deposition, a “trench” mask was used to do the photolithography to pattern the diaphragm areas (Figure 3.24). Then, *a*-silicon was etched away by LAM 490 using chlorine gas, which has a good selectivity between silicon and silicon oxide. Finally, the wet oxide was etched by BOE solution (Figure 3.25).



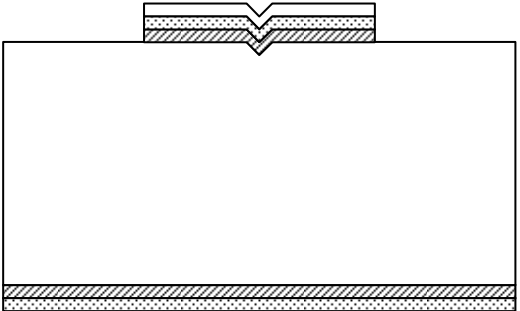
Thermal oxide Amorphous silicon



Thermal oxide Amorphous silicon HPR-504

Figure 3.23: Deposition of sacrificial layers.

Figure 3.24: Diaphragm area photolithography.



Thermal oxide Amorphous silicon HPR-504

Figure 3.25: Diaphragm area etching.

After stripping the photoresist, 400nm LS-SiN was deposited by LPCVD furnace and followed by a 600nm *a*-silicon layer (Figure 3.26). Then, a “resistors” mask was used to do the photolithography and the *a*-silicon was etched by an inductively coupled plasma (ICP) etcher using HBr gas (Figure 3.27).

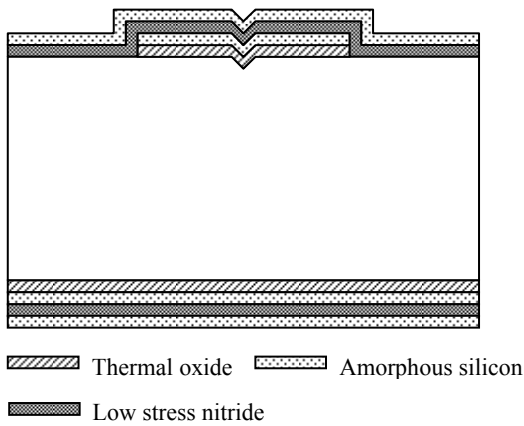


Figure 3.26: Piezoresistor material deposition.

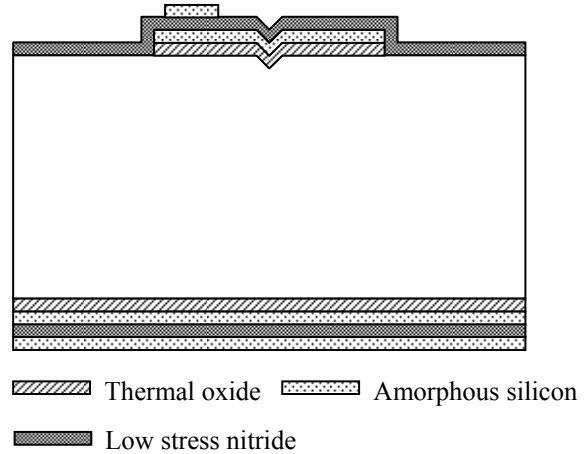


Figure 3.27: Define piezoresistor shape.

The next step was to re-crystallize the *a*-silicon to poly-Si by using the MILC technique. Firstly, a 300nm low temperature oxide (LTO) was deposited to cover the *a*-silicon layer (Figure 3.28). Then, a “contact hole” mask was used to do the photolithography and BOE was used to etch the LTO, which opened two induction holes on the resistor area (Figure 3.29). After removing the photoresist and doing an HF (1:100) solution dip, a 5nm nickel layer was evaporated onto the wafer surface (Figure 3.30). By annealing in the nitrogen environment at 590°C for 24 hours, the amorphous material was induced to poly-crystalline type, and a visible line (marked by the arrow in Figure 3.31) could be found in the middle of the resistor. This is the touched crystalline zone interface induced from the two holes. Then, the un-reacted nickel was removed by piranha solution and followed by a high temperature annealing at 900°C for 0.5 hours (Figure 3.32).

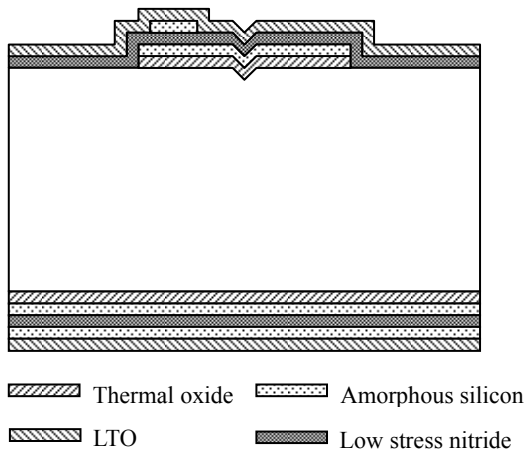


Figure 3.28: LTO deposition.

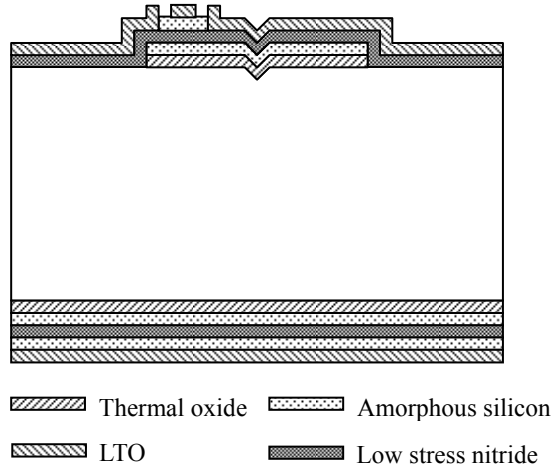


Figure 3.29: Open induce hole.

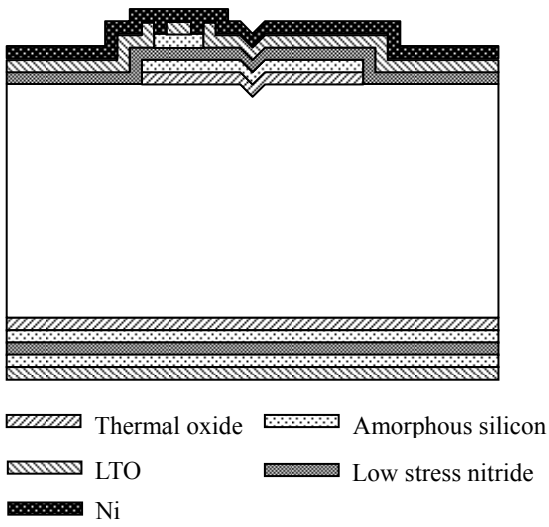


Figure 3.30: Ni evaporation.

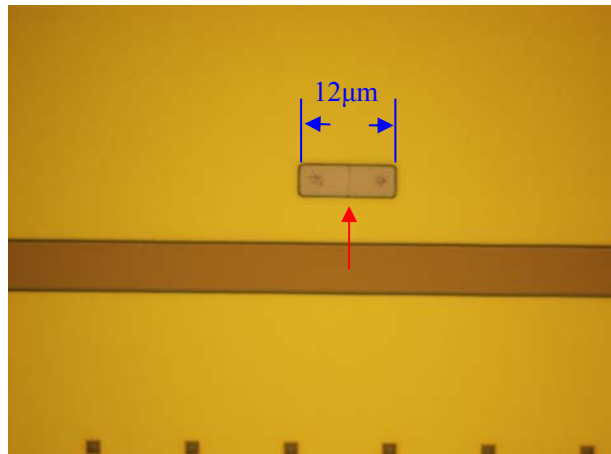


Figure 3.31: Microphotography of amorphous silicon after re-crystallization.

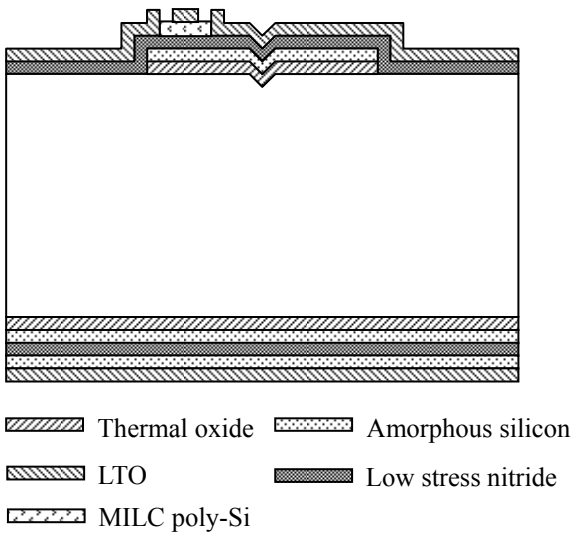


Figure 3.32: Remove Ni and high temperature annealing.

After *a*-Si re-crystallization, BOE solution was used to strip the LTO layer and boron was doped into the MILC poly-Si material through implantation technique (Figure 3.33). Because the poly-Si material is relatively thick (600nm), a double implantation technique was chosen and two implantations were carried out at 45KeV and 150KeV, respectively. For the sensing area, each implantation had a dose of  $2.1 \times 10^{14} \text{ cm}^{-2}$  and the total dose was  $4.2 \times 10^{14} \text{ cm}^{-2}$ ; the equivalent doping concentration was  $7 \times 10^{18} \text{ cm}^{-3}$ . For the connecting area, each implantation had a dose of  $1.2 \times 10^{16} \text{ cm}^{-2}$  and the total dose was  $2.4 \times 10^{16} \text{ cm}^{-2}$ ; the equivalent doping concentration was  $4 \times 10^{20} \text{ cm}^{-3}$ . After that, samples were put into the furnace at 1000°C for 1.5 hours to activate the doping impurity. The implantation energy and the activation temperature and time were simulated by SRIM and TSUPREM software.

Following this, by depositing the second LS-SiN layer (100nm), the MILC poly-Si piezoresistors were well protected (Figure 3.34). Then, a “contact hole” mask and photoresist FH 6400L were used to do the photolithography, and RIE 8110 was used to etch away the silicon nitride, which exposed the piezoresistor contacts for further metallization (Figure 3.35). The reason for using FH 6400L was that, after nitride etching, in the next step, the same photoresist was also used as the implantation mask and FH 6400L is a high melting point photoresist which can resist the high temperature generated by the iron bombardment during the implantation process.

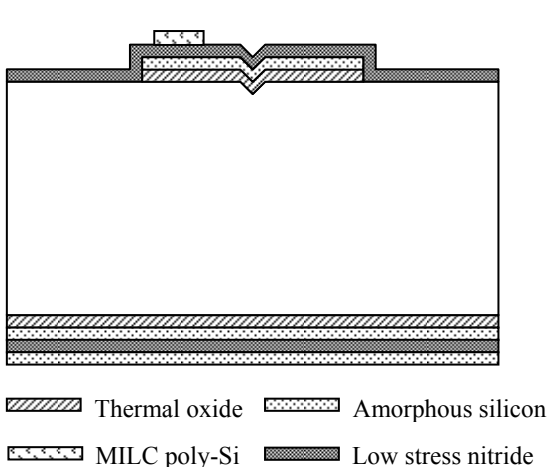


Figure 3.33: Boron doping and activation.

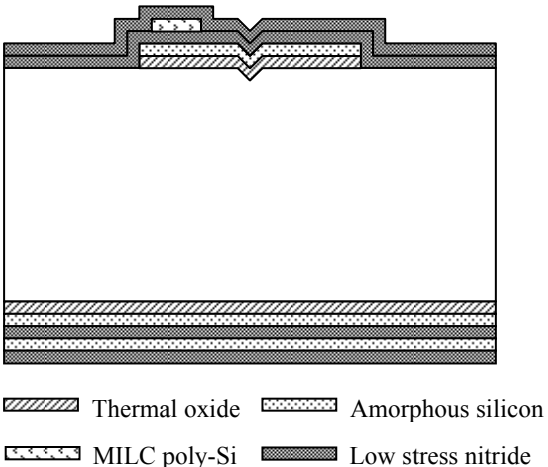


Figure 3.34: Second low stress nitride layer deposition.

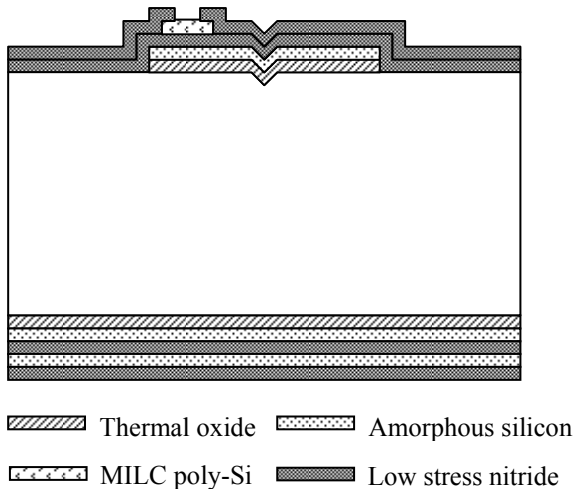
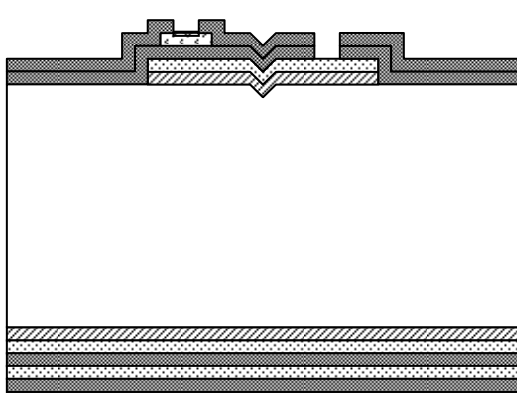


Figure 3.35: Open contact hole.

A heavy boron doping was carried out here to lower the contact resistance. The doping concentration was  $6 \times 10^{15} \text{ cm}^{-2}$ , with an implantation energy of 40KeV. Following the impurity implantation, an activation was carried out at  $900^\circ\text{C}$  for 30 minutes. After using the titanium silicide technique to improve the contact resistance, as mentioned in section 3.2.2, the “etching hole” mask was used to do the photolithography, and RIE 8110 was used to etch the silicon nitride to open the release etching holes (Figure 3.36).

The chromium and gold double layer metallization system, as mentioned in section 3.2.2, was deposited by a lift-off process. The details of the lift-off process are the following: Firstly spin coating of photoresist AZ 5200NJ at 4000 rpm and soft baking at  $100^\circ\text{C}$  for 150 seconds were done. Then the first exposure was carried out on Karl Suss MA6-2 contact aligner for 1.3 seconds and followed by a post-baking at  $110^\circ\text{C}$  for 3 minutes. The second flood-exposure was carried out later for 8 seconds to reverse the photoresist image, and the photoresist was developed in the FHD-5 solution for 130 seconds. Before being put into the sputter machine, a 3.5 minutes HF (1:100) dipping was carried out to remove the native oxide at the titanium silicide surface. After the metal lift-off process, the metal lines were well defined, as shown in Figure 3.37.



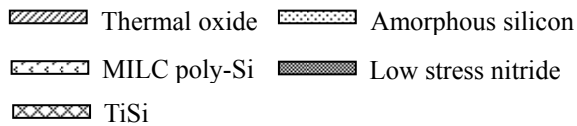


Figure 3.36: Open release hole.

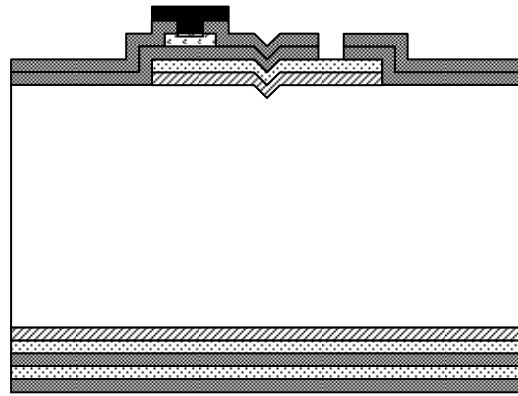




Figure 3.37: Metallization after lift-off process.

The final step was to etch away the two sacrificial layers (including *a*-silicon and oxide) and release the diaphragm, which is the same process as mentioned in section 3.2.1. Figure 3.38 presents a successfully fabricated wide-band high frequency microphone using the surface micromachining technique.

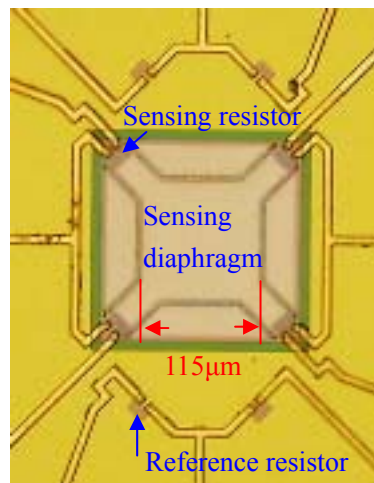


Figure 3.38: Microphotography of a wide-band high frequency microphone fabricated using the surface micromachining technique.

## 3.3 Silicon Bulk Micromachining Process

### 3.3.1 Comparison of Bulk Silicon Wet Etching and Dry Etching Techniques

Traditionally, the silicon bulk micromachining technique is achieved by using wet etching solutions such as Potassium hydroxide (KOH) or TMAH. Both of these two solutions have a good selectivity between silicon and silicon dioxide. However, due to the possible contamination from the potassium ions ( $K^+$ ), the TMAH solution is more widely used in the complementary metal–oxide–semiconductor (CMOS) compatible MEMS process, instead of using KOH solution.

The advantage of the wet bulk micromachining technique is that tenths of wafers can be processed simultaneously, which in turn increases the throughput. On the other hand, the disadvantages of the wet bulk micromachining technique are severe. The first one is due to the corrosive characteristic of the wet etching solution. In many devices' fabrication process flows, especially in the MEMS area, in order to increase the yield, the release step is made the final step, which means that the metallization is put on the wafer earlier. The traditional metal material used in the semiconductor fabrication process is silicon doped aluminium (AlSi), which can be easily etched away by either KOH or THAM solution. So, some techniques have been developed to overcome this problem. As mentioned in section 3.2.2, a chromium/gold double layer metallization system with self-aligned titanium silicidation technique can be used to achieve the final release with TMAH solution. However, this technique not only complicates the whole process flow, but also requires a thick gold layer ( $1\mu\text{m}$ ), which greatly increases the cost. Another technique [34] uses a modified TMAH solution, consisting of 5 wt. % TMAH, 1.4 wt. % (or above) dissolved silicon and 0.4-0.7 wt. % ammonium peroxodisulfate ( $(\text{NH}_4)_2\text{S}_2\text{O}_8$ ). This modified TMAH solution will not attack AlSi material and could be used in some MEMS applications. But the limitation is that this technique requires a good control of the solution ingredients, which is not easy to maintain. For example, normally, the TMAH solution is heated up to  $80^\circ\text{C}$  to increase the etching rate, and during etching that takes place over a long period of time, the water will be vaporized,

and then the percentage of the dissolved silicon and ammonium peroxodisulfate will continuously change, which needs an on-line monitoring system or requires a continuously introduction of fresh etching solution.

The second disadvantage of the wet bulk micromachining technique is due to the anisotropic etching characteristic of the KOH and TMAH solutions. For sc-silicon, these solutions have an etching selectivity between the silicon (100) plane and (111) plane (Figure 3.39). Normally the wet etching starts from the backside of the wafer. Due to the etching angle of  $54.74^\circ$ , for a  $300\mu\text{m}$  thick silicon wafer, to release a front-side square diaphragm with a length of  $200\mu\text{m}$ , the backside opening length will be about  $624\mu\text{m}$ . This takes much more area and in turn limits the device density in a single wafer. The anisotropic etching characteristic also brings in another problem. That is that the front-side diaphragm can only be designed to be a square/rectangular shape, which limits the design varieties. Any arbitrary etching opening will be etched into a rectangle containing a width and length equal to the largest dimension of the opening in the horizontal and vertical directions (Figure 3.40).

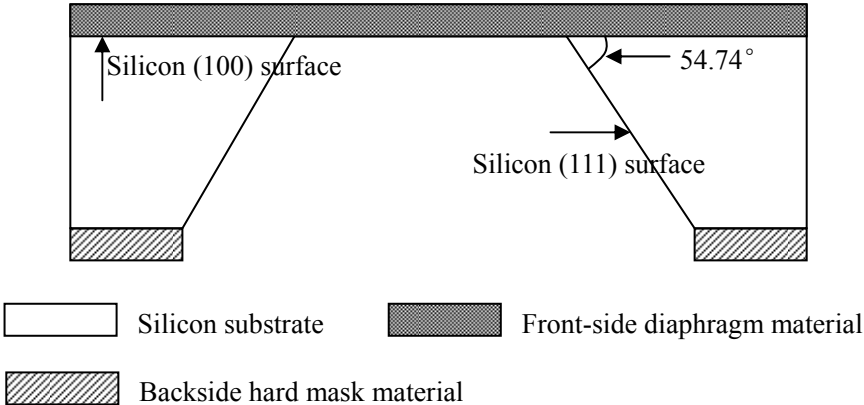


Figure 3.39: Etching profile of the KOH/TMAH solutions.

Compared to the wet bulk micromachining technique, the dry bulk micromachining technique, more specifically the silicon DRIE technique, overcomes all these drawbacks. The DRIE etching technique consists of a series of etching cycles. In each cycle, two steps are performed. The first step is to etch silicon in a vertical direction, and the second step is to protect the sidewall of the etched cavity using polymer. There is only one issue needing to be considered:



the etching or bombardment selectivity between silicon and the diaphragm material. In this thesis, the diaphragm is built with LS-SiN material, and even though the selectivity between silicon and LS-SiN is quite high (~85:1), due to the DRIE etching rate non-uniformity and the substrate thickness non-uniformity, a long duration over-etching is still needed. Then if the LS-SiN material is directly deposited on top of the silicon substrate, during the over-etching time, the LS-SiN material will be etched. In the following section, we demonstrate a two buffer layer process, containing one silicon dioxide layer and one *a*-silicon layer. In the DRIE over-etching time, the reaction will self-stop on the silicon dioxide layer, which has a selectivity of ~1:200 to the sc-silicon material. In the next step, without the second *a*-Si buffer layer, when the oxide layer is removed using the RIE technique, the selectivity between oxide and LS-SiN is ~1:1, which means any over-etching of oxide material will etch the LS-SiN diaphragm at the same thickness. But when the *a*-silicon buffer layer is inserted, the selectivity between the oxide and amorphous silicon is ~7:1 and the ICP etching selectivity between *a*-silicon and LS-SiN is ~4:1, which are all acceptable.

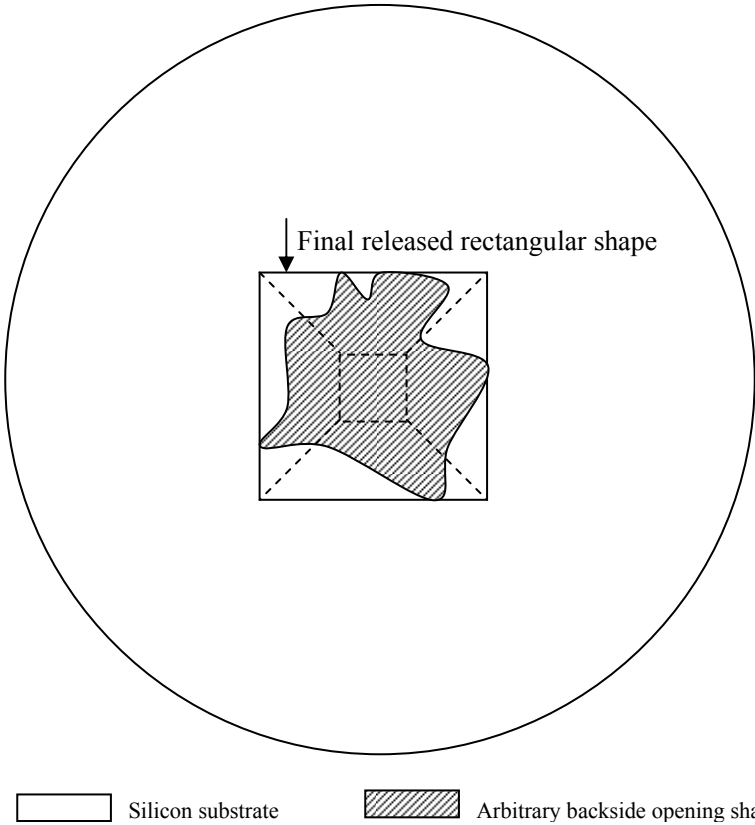


Figure 3.40: Top view of an arbitrary backside opening etching shape.

### 3.3.2 Details of Fabrication Process Flow

The bulk micromachining technique started from a double-side polished p-type (100) wafer with a thickness of 300 $\mu\text{m}$ . At the beginning, a 0.5 $\mu\text{m}$  thick thermal oxide, a 0.1 $\mu\text{m}$  thick *a*-silicon layer and a 0.4 $\mu\text{m}$  thick LS-SiN layer were deposited in sequence (Figure 3.41).

Following that, a 0.6 $\mu\text{m}$  thick *a*-silicon layer was deposited as the piezoresistive material. The back-side *a*-silicon material was removed by a LAM 490 etching machine and the front-side *a*-silicon was re-crystallized to poly-Si material using the MILC technique, which is the same as the technique mentioned in the previous section. This re-crystallized poly-Si layer was then patterned to form the piezoresistor shape as shown in Figure 3.42.

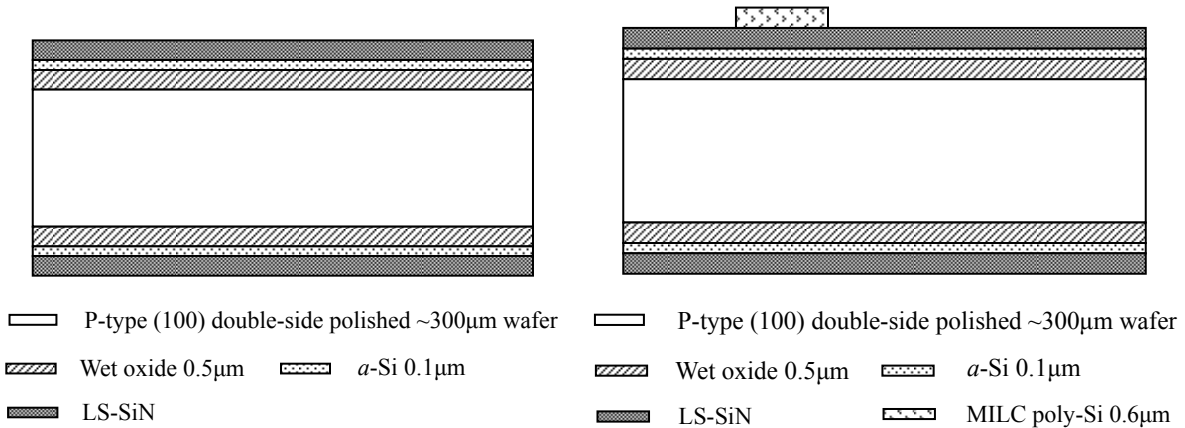


Figure 3.41: Diaphragm layers deposition.

Figure 3.42: Piezoresistor forming.

The piezoresistor was doped by the boron implantation technique with doping energy of 45KeV and 150KeV, respectively. For each implantation, the dose was  $2.1 \times 10^{14} \text{ cm}^{-2}$  and the total dose was  $4.2 \times 10^{14} \text{ cm}^{-2}$ ; the equivalent doping concentration was  $7 \times 10^{18} \text{ cm}^{-3}$ . After that, the wafer was put into the furnace at 1000 $^{\circ}\text{C}$  for 1.5 hours to activate the doping impurity.

After doping activation, the second 0.1 $\mu\text{m}$  thick LS-SiN layer was deposited, and then a 2 $\mu\text{m}$  thick LTO was deposited and the front-side LTO material was removed by BOE solution (Figure 3.43).

Then, the contact hole was opened by using photoresist FH 6400L and the RIE 8110 dry etching machine. The contact area was heavily boron doped with a concentration of  $6 \times 10^{15} \text{ cm}^{-2}$  and an implantation energy of 40KeV. Following the impurity implantation, an activation was carried out at 900°C for 30 minutes. After that, a 0.5µm thick Al:Si was sputtered and patterned to form the metallization (Figure 3.44). A forming gas annealing at 400°C for 30 minutes was carried out to improve the contact resistance.

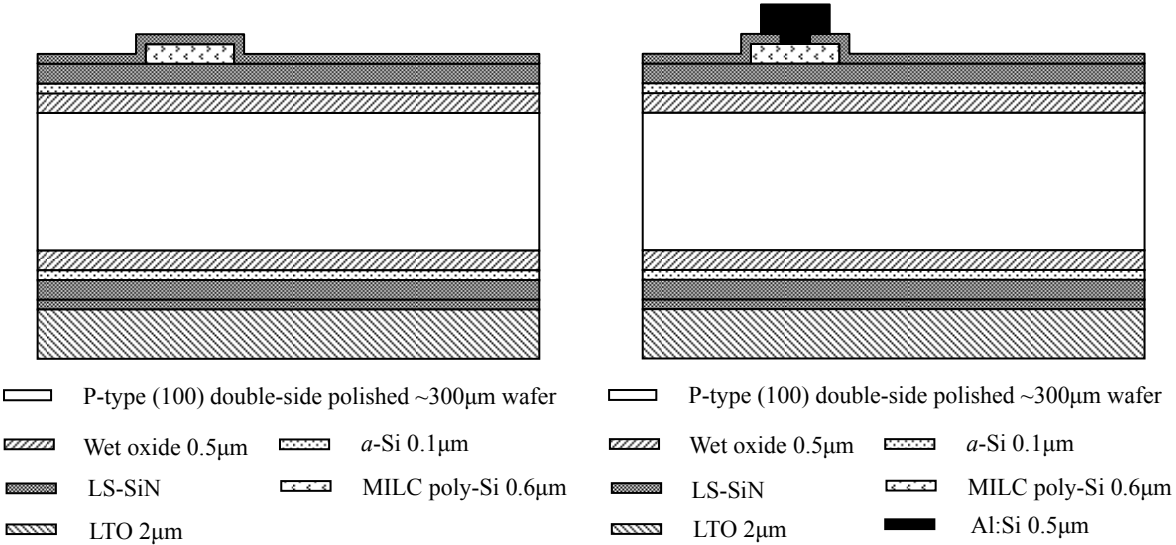


Figure 3.43: Piezoresistor protection and backside hard mask deposition.

Figure 3.44: Metallization.

Then, a 3µm thick photoresist PR507 was coated on to the back-side of the wafer and was patterned to form the diaphragm area (Figure 3.45). In the next step, the back-side coated material LTO, LS-SiN, amorphous silicon and thermal oxide layers were removed by the dry etching technique (advanced oxide etching machine, RIE 8110 etching machine, ICP poly-Si etching machine and RIE 8110 etching machine) in sequence. After that, the silicon substrate was etched through using the DRIE technique. During this etching, the photoresist PR507 together with the LTO performed as the mask layer. The DRIE silicon etching self-stopped at the front-side thermal oxide layer and the back-side photoresist PR507 was totally removed. Then the front-side thermal oxide and *a*-silicon was also removed using dry etching technique (RIE 8110 etching machine and ICP poly-Si etching machine) (Figure 3.46).

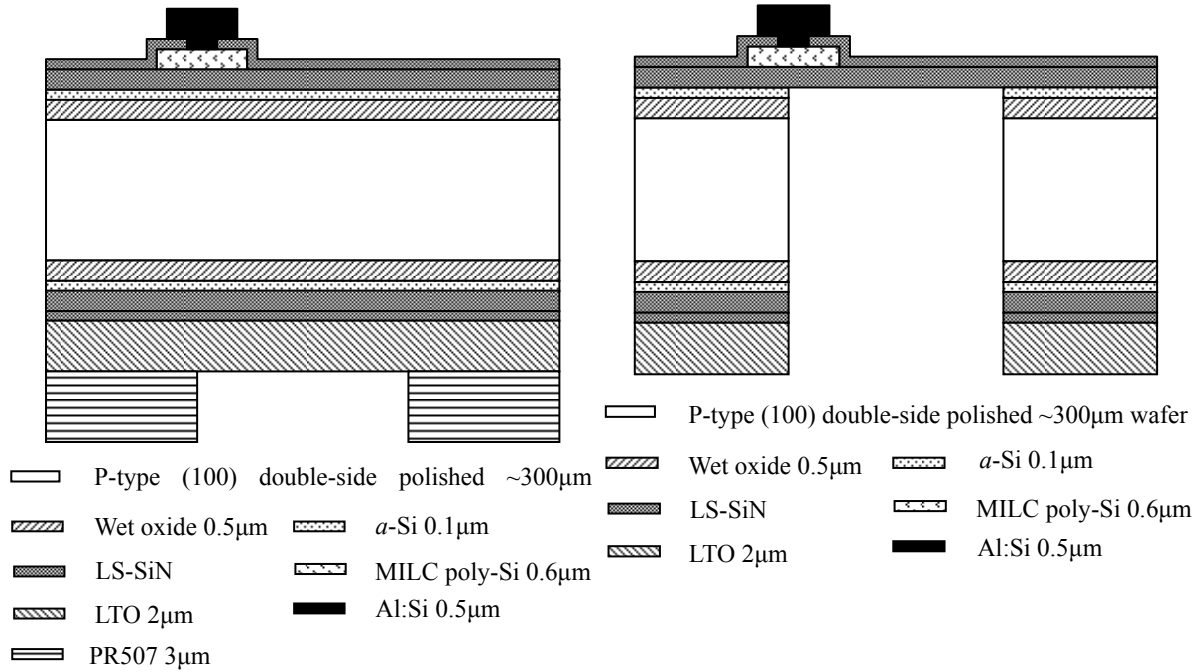


Figure 3.45: Diaphragm area patterning.

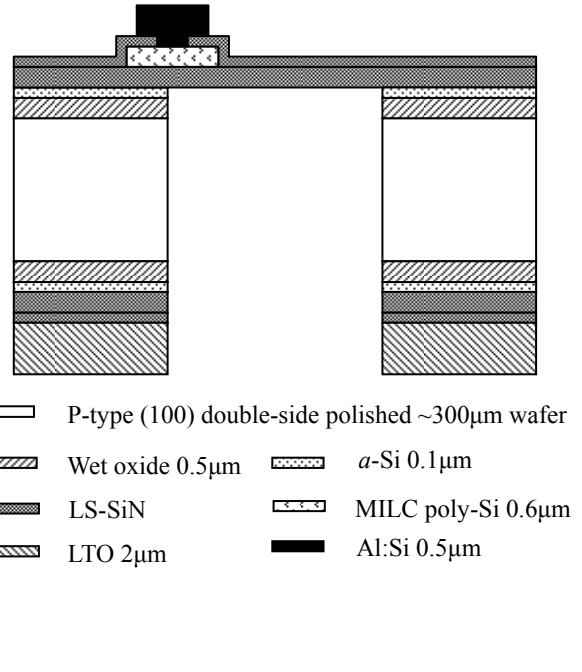


Figure 3.46: Cross-sectional view of the microphone device after dry etching release.

Figure 3.47 presents a successfully fabricated wide-band high frequency microphone using the bulk micromachining technique.

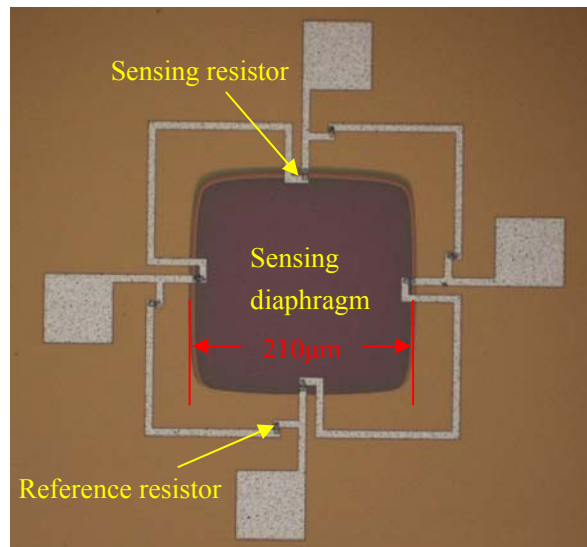


Figure 3.47: Microphotography of a wide-band high frequency microphone fabricated using the bulk micromachining technique.

When we did the back-side diaphragm area photolithography shown in Figure 3.45, narrow cutting lines with a width of  $10\mu\text{m}$  were also patterned surrounding each die. During the DRIE etching step, due to the well known DRIE lag effect, which could be simply described as the etching rate being proportional to the pattern feature size, the etching rate in the cutting line area was lower than the etching rate in the diaphragm area. So when the sc-Si under the diaphragm area was totally etched away, there was still a silicon layer remaining under the cutting line. The advantage of this arrangement is that, the remaining silicon layer under the cutting line area could support the whole wafer so that it would not break during the DRIE etching process, but at the same time, the remaining thin silicon layer could easily be broken using a diamond scribe. During the die cutting, applying small force would cause the die to be separated along the cutting line and the already suspended sensing diaphragm would not be broken. Figure 3.48 is the cross-sectional view microphotography of a cut die edge. It shows that for a  $300\mu\text{m}$  thick substrate, the remaining silicon layer thickness under the cutting line area is about  $120\mu\text{m}$ .

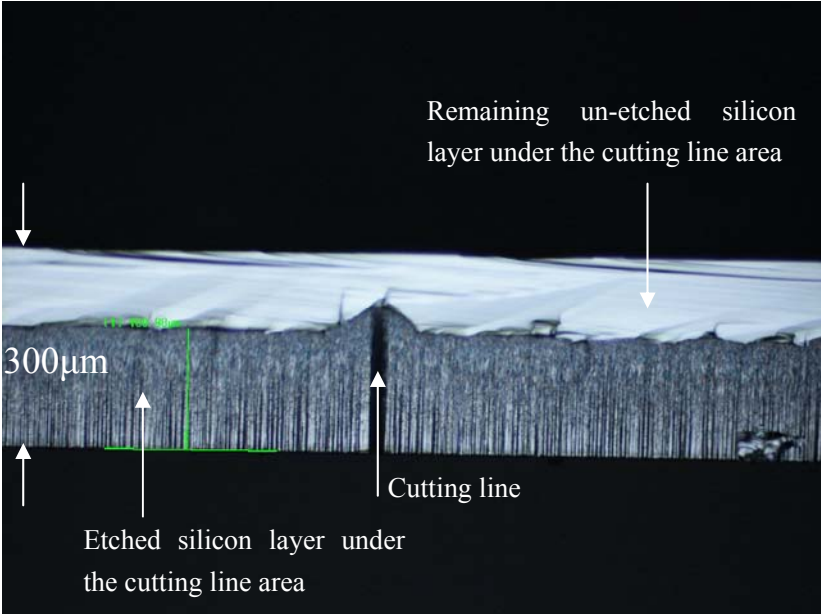


Figure 3.48: Cross-sectional view microphotography of the cut die edge.

### 3.4 Summary

In this chapter, firstly, the MILC technique is introduced. Poly-Si material fabricated using this technique offers a better piezoresistive property compared with the traditional SPC poly-Si material and is also relatively easier to fabricate, which makes the process to be more flexible compared with other re-crystallization techniques and also including the sc-Si material. Several key steps during the surface micromachining fabrication process are characterized, including the metallization system, the metal to poly-Si contact system, the dimple stiction prevention structure and the non-standard cavity release pattern. Following this, the whole surface micromachining fabrication process with cross-section views of each step are presented for reference. Finally, after comparing the bulk silicon wet etching and dry etching techniques, the bulk micromachining fabrication process, which is based on the DRIE dry etching technique, is presented with the cross-section schematics of each step.

### 3.5 References

- [1] W. C. Hsu, "Fabrication and Characterization of Polysilicon Thin Film Transistors With Various Channel Length/Width Ratios," MSc Thesis, Department of Electrical Engineering, Southern Taiwan University, 2006.
- [2] A. R. Joshi, "High Performance CMOS With Metal Induced Lateral Crystallization Of Amorphous Silicon," Ph.D Thesis, Stanford University, 2003.
- [3] W. Mingxiang, M. Zhiguo, Y. Zohar, and W. Man, "Metal-induced laterally crystallized polycrystalline silicon for integrated sensor applications," *Electron Devices, IEEE Transactions on*, vol. 48, pp. 794-800, Apr. 2001.
- [4] M. McCann, K. Catchpole, and A. W. Blakers, "A Review Of Thin Film Silicon For Solar Cell Applications," Australian National University, Report, 2004.
- [5] C. Young Jin, K. Won Kyu, C. Kyu Sik, K. Sung Ki, and J. Jin, "Hydrogenated amorphous silicon thin-film transistor with a thin gate insulator," *Electron Device Letters, IEEE*, vol. 21, pp. 18-20, 2000.
- [6] S. Wen-Jyh, L. Jyh-Ling, and L. Si-Chen, "High-performance a-Si:H thin-film transistor using lightly doped channel," *Electron Devices, IEEE Transactions on*, vol. 38, pp. 676-678, 1991.
- [7] J. M. Jaffe, "Monolithic polycrystalline-silicon pressure transducer," *Electronics Letters*, vol. 10, pp. 420-421, 1974.
- [8] E. Luder, "Polycrystalline silicon-based sensors," *Sensors and Actuators*, vol. 10, pp. 9-23, 1986.
- [9] Y.-C. Tai and R. S. Muller, "IC-processed electrostatic synchronous micromotors," *A Special Issue Devoted to Micromechanics*, vol. 20, pp. 49-55, 1989.
- [10] L.-S. Fan, Y.-C. Tai, and R. S. Muller, "IC-processed electrostatic micromotors," *A Special Issue Devoted to Micromechanics*, vol. 20, pp. 41-47, 1989.
- [11] K. Nakazawa, "Recrystallization of amorphous silicon films deposited by low pressure chemical vapor deposition from Si<sub>2</sub>H<sub>6</sub> gas," *Journal of Applied Physics*, vol. 69, pp. 1703-1706, 1991.
- [12] A. T. Voutsas and M. K. Hatalis, "Deposition and Crystallization of a-Si Low Pressure

- Chemically Vapor Deposited Films Obtained by Low-Temperature Pyrolysis of Disilane," *Journal of the Electrochemical Society*, vol. 140, pp. 871-877, March 1993.
- [13] S. Hasegawa, S. Sakamoto, T. Inokuma, and Y. Kurata, "Structure of recrystallized silicon films prepared from amorphous silicon deposited using disilane," *Applied Physics Letters*, vol. 62, pp. 1218-1220, 1993.
- [14] M. K. Hatalis and D. W. Greve, "Large grain polycrystalline silicon by low-temperature annealing of low-pressure chemical vapor deposited amorphous silicon films," *Journal of Applied Physics*, vol. 63, pp. 2260-2266, 1988.
- [15] V. Subramanian and K. C. Saraswat, "High-performance germanium-seeded laterally crystallized TFTs for vertical device integration," *Electron Devices, IEEE Transactions on*, vol. 45, pp. 1934-1939, 1998.
- [16] V. Subramanian, M. Toita, N. R. Ibrahim, S. J. Souri, and K. C. Saraswat, "Low-leakage germanium-seeded laterally-crystallized single-grain 100-nm TFTs for vertical integration applications," *Electron Device Letters, IEEE*, vol. 20, pp. 341-343, 1999.
- [17] G. Radnoczi, A. Robertsson, H. T. G. Hentzell, S. F. Gong, and M. A. Hasan, "Al induced crystallization of a-Si," *Journal of Applied Physics*, vol. 69, pp. 6394-6399, May 1, 1991.
- [18] J. Stoemenos, J. McIntosh, N. A. Economou, Y. K. Bhatnagar, P. A. Coxon, A. J. Lowe, and M. G. Clark, "Crystallization of amorphous silicon by reconstructive transformation utilizing gold," *Applied Physics Letters*, vol. 58, pp. 1196-1198, 1991.
- [19] B. Bian, J. Yie, B. Li, and Z. Wu, "Fractal formation in a-Si:H/Ag/a-Si:H films after annealing," *Journal of Applied Physics*, vol. 73, pp. 7402-7406, 1993.
- [20] S. Lee, Y. Jeon, and S. Joo, "Pd induced lateral crystallization of amorphous Si thin films," *Applied Physics Letters*, vol. 66, pp. 1671-1673, 1995.
- [21] J. K. Park, S. H. Kim, W. S. Shon, S. J. Park, J. Jang, S. Y. Yoon, C. O. Kim, and Y. Cuo, "Polycrystalline Silicon Thin Film transistor Using Co Induced MIC," in *Thin Film Transistor Technologies IV*, ed Pennington, NJ: The Electrochemical Society Inc., 1998.
- [22] Y. Kawazu, H. Kudo, S. Onari, and T. Arai, "Low-Temperature Crystallization of Hydrogenated Amorphous Silicon Induced by Nickel Silicide Formation," *Japanese Journal of Applied Physics*, vol. 29, pp. 2698-2704, 1990.
- [23] A. Nakamura, F. Emoto, E. Fujii, Y. Uemoto, A. Yamamoto, K. Senda, and G. Kano,



- "Recrystallization Mechanism for Solid Phase Growth of Poly-Si Films on Quartz Substrates," *Japanese Journal of Applied Physics*, vol. 27, pp. 2408-2410, 1988.
- [24] G. Liu and S. J. Fonash, "Selective area crystallization of amorphous silicon films by low-temperature rapid thermal annealing," *Applied Physics Letters*, vol. 55, pp. 660-662, 1989.
- [25] C. D. Lien, M. A. Nicolet, and S. S. Lau, "Low Temperature Formation of NiSi<sub>2</sub> from Evaporated Silicon," in *physica status solidi (a)* vol. 81, WILEY-VCH Verlag, pp. 123-128, 1984.
- [26] J. Zhonghe, K. Moulding, H. S. Kwok, and M. Wong, "The effects of extended heat treatment on Ni induced lateral crystallization of amorphous silicon thin films," *Electron Devices, IEEE Transactions on*, vol. 46, pp. 78-82, 1999.
- [27] C. Hayzelden and J. L. Batstone, "Silicide formation and silicide-mediated crystallization of nickel-implanted amorphous silicon thin films," *Journal of Applied Physics*, vol. 73, pp. 8279-8289, June 15, 1993.
- [28] X. F. Duan, "Microfabrication Using Bulk Wet Etching with TMAH," MSc Thesis, Department of Physics, McGill University, 2005.
- [29] I. Virginia Semiconductor, "Wet-Chemical Etching and Cleaning of Silicon," 2003.
- [30] A. E. Morgan, E. K. Broadbent, K. N. Ritz, D. K. Sadana, and B. J. Burrow, "Interactions of thin Ti films with Si, SiO<sub>2</sub>, Si<sub>3</sub>N<sub>4</sub>, and SiO<sub>x</sub>N<sub>y</sub> under rapid thermal annealing," *Journal of Applied Physics*, vol. 64, pp. 344-353, July 1, 1988.
- [31] R. W. Mann, L. A. Clevenger, P. D. Agnello, and F. R. White, "Silicides and local interconnections for high-performance VLSI applications," in *IBM Journal of Research and Development* vol. 39, pp. 403-417, 1995.
- [32] L. J. Chen and E. Institution of Electrical, *Silicide technology for integrated circuits*: Institution of Electrical Engineers, 2004.
- [33] Z. Yu, P. Nikkel, S. Hathcock, Z. Lu, D. M. Shaw, M. E. Anderson, and G. J. Collins, "Measurement and control of a residual oxide layer on TiSi<sub>2</sub> films employed in ohmic contact structures," *Semiconductor Manufacturing, IEEE Transactions on*, vol. 9, pp. 329-334, 1996.
- [34] G. Yan, P. C. H. Chan, I. M. Hsing, R. K. Sharma, J. K. O. Sin, and Y. Wang, "An improved

TMAH Si-etching solution without attacking exposed aluminum," *Sensors and Actuators A: Physical*, vol. 89, pp. 135-141, 2001.

## Chapter 4: Testing of the MEMS Sensor

This chapter is divided into four sections. The first section presents the testing of key fabrication process properties, including the piezoresistor sheet resistance measurement and metal to piezoresistor contact resistance measurement. The second section presents the static responses of the microphone samples measured by the nano-indentation technique. In the third section, the dynamic calibration method using spark generated shockwave is demonstrated to measure the frequency response of the wide-band high frequency microphone. And, finally, the sensor array application as a sound source localizer is presented.

### 4.1 Sheet Resistance and Contact Resistance

The sheet resistance of the doped MILC poly-Si material was measured by a Greek cross structure, as shown in Figure 4.1 (also marked within the blue dashed line in Figure 2.2). During the test, a current,  $I_{AB}$ , was passed through pad A and B and the potential difference  $V_{CD}$  between pad C and D was measured. The sheet resistance  $R_s$  was calculated using Equations 4.1 and 4.2 shown below.

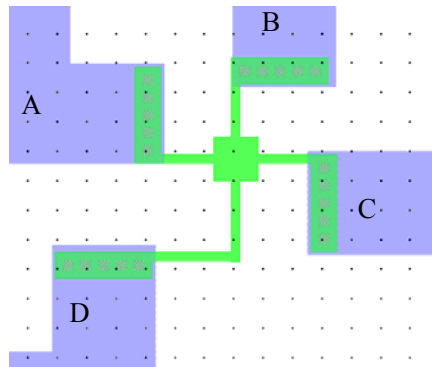


Figure 4.1: Layout of the Greek cross structure.

$$R = \frac{V_{CD}}{I_{AB}} \quad (4.1)$$

$$R_s = \frac{\pi R}{\ln 2} \quad (4.2)$$

For the sample fabricated using the surface micromachining technique, the measured average sheet resistances of the sensing area and the connecting area were 411.4 ohm/square ( $\Omega/\square$ ) and 24.7 $\Omega/\square$ , respectively. For the sample fabricated using the bulk micromachining technique, the measured average sheet resistance of the sensing area was 446.4 $\Omega/\square$ . Because the sensing resistors were fabricated using the same MILC technique with the same impurity doping and activation conditions for both the surface and bulk micromachining techniques, their sheet resistances are almost the same.

The Kelvin structure shown in Figure 4.2 (also marked within the purple dashed line in Figure 2.2) was used to measure contact resistance  $R_c$  of the metallization system to the doped MILC poly-Si material. During the test, a current  $I_{AC}$ , was passed through pad A and C, and the potential difference  $V_{BD}$  between pad B and D was measured. The contact resistance was calculated by Equation 4.3 and the specific contact resistivity  $\rho_c$  was calculated by Equation 4.4, where  $A$  is the contact area.

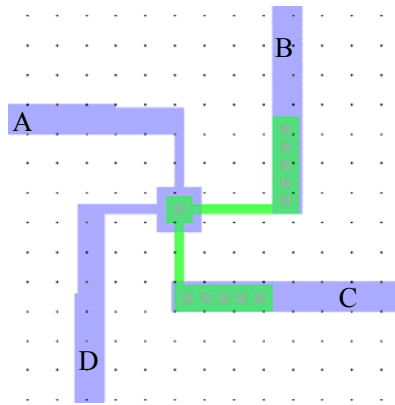


Figure 4.2: Layout of the Kelvin structure.

$$R_c = \frac{V_{BD}}{I_{AC}} \quad (4.3)$$

$$\rho_c = R_c A \quad (4.4)$$

For the Cr/Au to MILC poly-Si contact system, the measured average contact resistance was  $46.6\Omega$  and the specific contact resistivity was  $2.91\mu\Omega\cdot\text{cm}^2$  (with a contact area of  $6.25\mu\text{m}^2$ ) and for the Al:Si to MILC poly-Si contact system, the measured average contact resistance was  $58\Omega$  and the specific contact resistivity was  $2.32\mu\Omega\cdot\text{cm}^2$  (with a contact area of  $4\mu\text{m}^2$ ). From this comparison, we can see that with the help of the self-aligned titanium silicide layer, the specific contact resistivity of the Cr/Au to MILC poly-Si system is only a little bit larger than that of the traditional Al:Si to MILC poly-Si system.

## 4.2 Static Point-load Response

The static measurement setup is shown in Figure 4.3. The fabricated chip was wire-bonded onto a PCB. The latter was then glued to a metallic holder and fixed on a vibration-free stage. A computer-controlled tribo-indenter was used to apply a point-load, through a probe with a conical tip having radius of  $25\mu\text{m}$  (Figure 4.4), at the center of the sensing diaphragm. A Wheatstone bridge (Figure 4.5), consisting of two sensing and two reference resistors respectively on- and off- the diaphragm, was used to measure the static force response of the diaphragm. With a DC input bias, the output voltage was measured and recorded using an HP 4155 Semiconductor Parameter Analyzer. For a  $115\times 115\mu\text{m}^2$  square diaphragm, which was fabricated using the surface micromachining technique, with a DC bias of 2V, a static response of  $\sim 0.4\mu\text{V/V/Pa}$  was measured (Figure 4.6). And for a  $210\times 210\mu\text{m}^2$  square diaphragm, which was fabricated using the bulk micromachining technique, with a DC bias of 3V, a static response of  $\sim 0.28\mu\text{V/V/Pa}$  was measured (Figure 4.7).

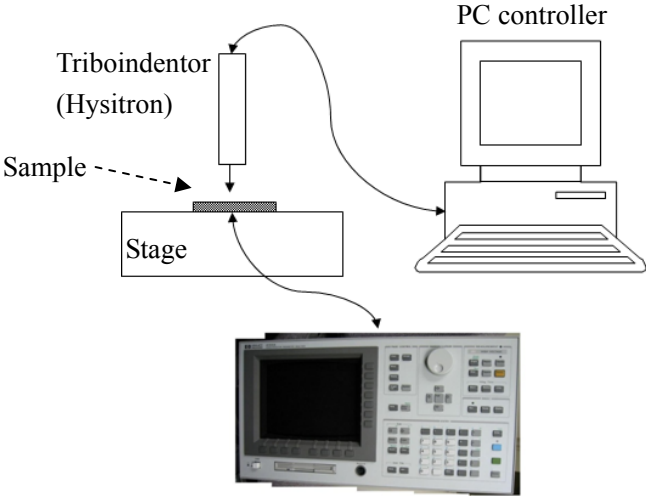


Figure 4.3: Static measurement setup.

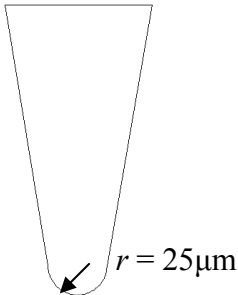


Figure 4.4: Cross-sectional view of the probe applying the point-load.

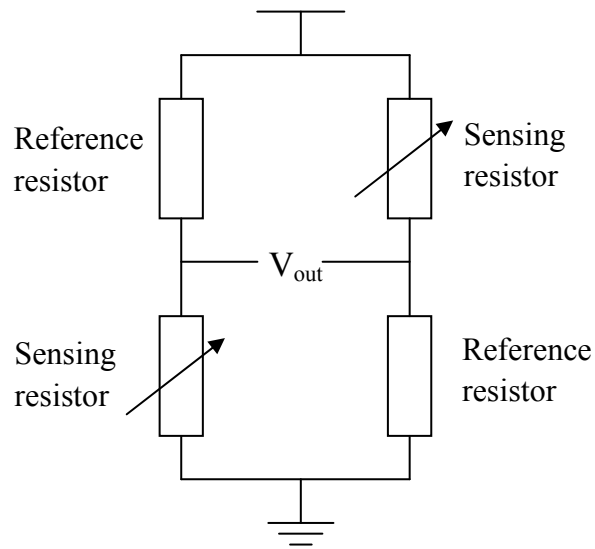


Figure 4.5: Wheatstone bridge configuration.

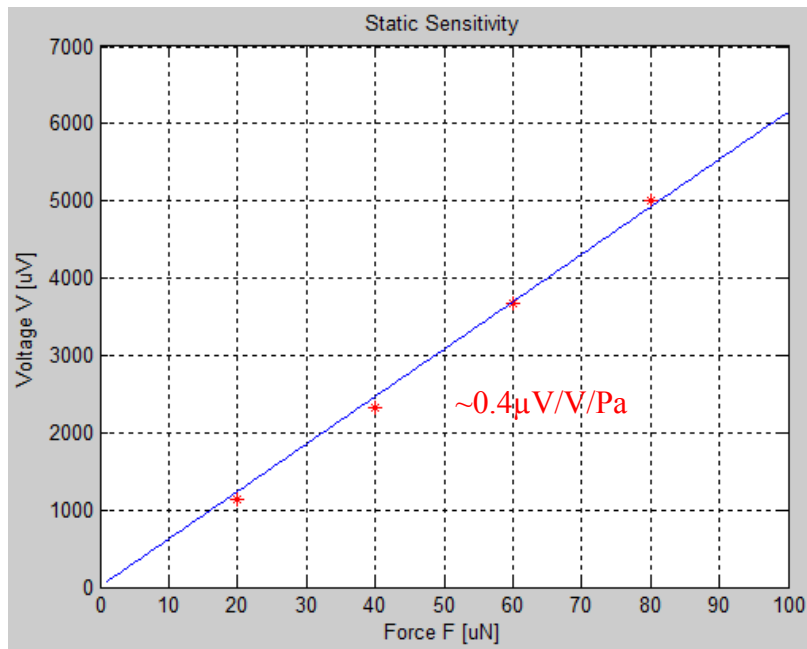


Figure 4.6: Typical measurement result with a diaphragm length of  $115\mu\text{m}$  and thickness of  $0.5\mu\text{m}$  (fabricated using the surface micromachining technique).

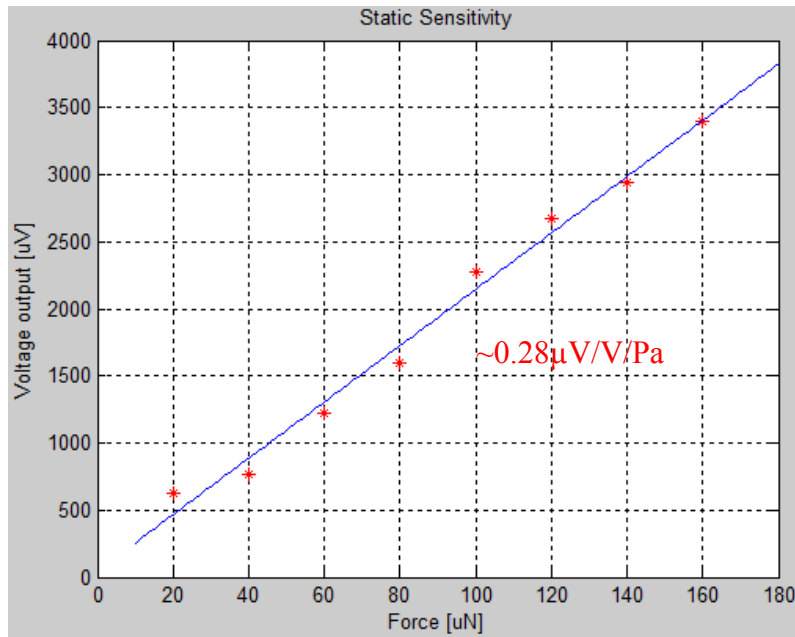


Figure 4.7: Typical measurement result with a diaphragm length of 210 $\mu\text{m}$  and thickness of 0.5 $\mu\text{m}$  (fabricated using the bulk micromachining technique).

Figure 4.6 shows that for the surface micromachined device, the voltage output is linear at least to 80 $\mu\text{N}$ , which is equivalent to 4.4kPa (equivalent pressure is calculated by dividing the point force by diaphragm area plus the supporting beams' areas). And Figure 4.7 shows that for the bulk micromachined device, the voltage output is linear at least to 160 $\mu\text{N}$ , which is equivalent to 3.6kPa (equivalent pressure is calculated by dividing the point force by diaphragm area).

Figure 4.8 and Figure 4.9 present the applied point-load versus diaphragm center displacement and corresponding equivalent pressure load versus diaphragm center displacement relationships, respectively. The extrapolated mechanical sensitivity in the unit of nm/Pa is 0.32 and 0.29 for the surface micromachined diaphragm and the bulk micromachined diaphragm, respectively. The ratio of the mechanical sensitivity is  $0.32\text{nm/Pa} \div 0.29\text{nm/Pa} = 1.1$ , while the ratio of the measured static electrical sensitivity is  $0.4\mu\text{V/V/Pa} \div 0.28\mu\text{V/V/Pa} = 1.43$ . This means that compared to the fully clamped diaphragm (bulk micromachining technique), the beam supported diaphragm (surface micromachining technique) has a more efficient mechanical to electrical conversion. With the same displacement, the beam supported diaphragm generates more stress at the piezoresistor



location and leads to a higher electrical voltage output.

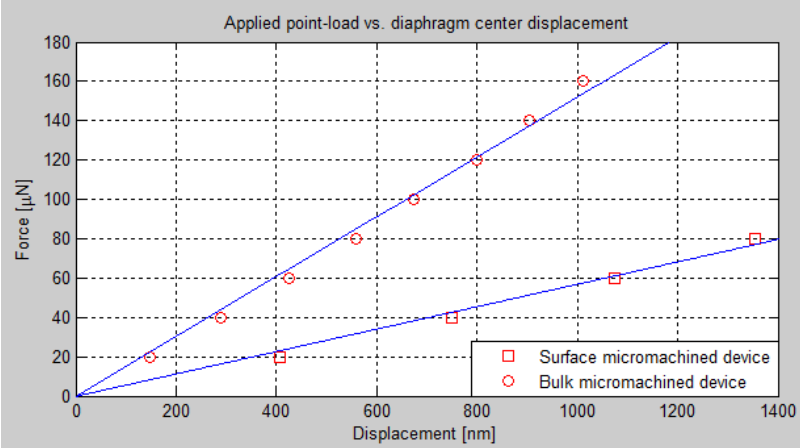


Figure 4.8: Point-load vs. displacement relationships of sensors fabricated using two different micromachining techniques.

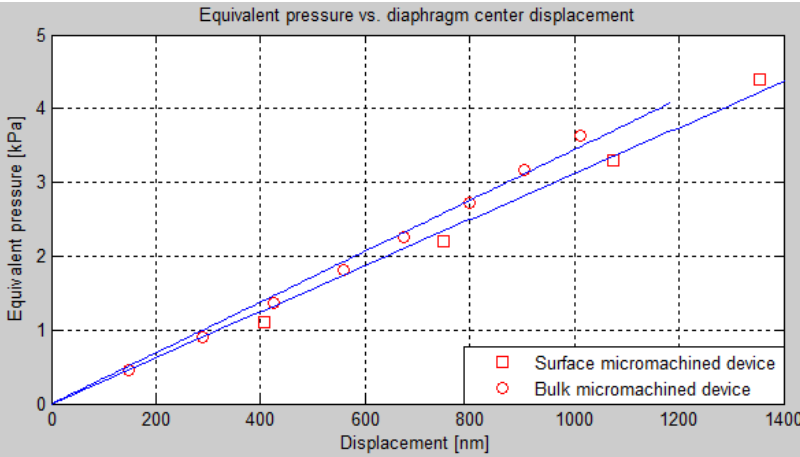


Figure 4.9: Equivalent pressure vs. displacement relationships of sensors fabricated using two different micromachining techniques.

## 4.3 Dynamic Calibration

### 4.3.1 Review of Microphone Calibration Methods

To calibrate a microphone, there are many methods with different names. However, from a methodology point of view, they can be classified into just two categories: the primary method and the secondary method. Techniques that are described for calibrating a microphone, except the techniques that require a calibrated standard microphone, are considered to be primary methods. A primary method requires basic measurements of voltage, current, electrical and acoustical impedance, length, mass (or density), and time (frequency). In practice, handbook values of density, sound speed, elasticity, and so forth are used rather than directly measured values of these parameters. The secondary methods are those in which a microphone that has been calibrated by a primary method is used as a reference standard. Secondary methods for calibrating microphones require fewer measurements and provide fewer sources of error than do primary methods. Therefore, they are more generally used for routine calibrations, although the accuracy of secondary calibrations can never be better than the accuracy of the primary calibration of the reference standard, if only one standard is used. Accuracy and reliability can be increased by averaging the results of measurements with two or three standards [1].

#### 4.3.1.1 Reciprocity Method

The reciprocity method is the mostly used primary method to calibrate microphones. The reciprocity principle as applied to electroacoustics was introduced by Schottky [2] in 1926 and Ballantine [3] in 1929. MacLean [4] and Cook [5] first used it for calibration purposes in 1940 and 1941. The reciprocity theorem is not only valid for the condenser microphone itself but also for the combined electrical, mechanical and acoustical network which is made up of a transmitter and a receiver microphone coupled to each other via an acoustic impedance. This makes reciprocity calibration possible [6].

The reciprocity method requires the to-be-calibrated microphone to be reciprocal; that is, the ratio of its receiving sensitivity  $M$  to its transmitting response  $S$  must be equal to a constant  $J$  called the reciprocity parameter. This parameter depends on the acoustic medium, the frequency, and the boundary conditions but is independent of the type or construction details of the microphone. To be reciprocal, a microphone must be linear, passive, and reversible. However, not all linear, passive, and reversible microphones are reciprocal. Conventional microphones, such as piezoelectric, piezoceramic, magnetostrictive, moving-coil, condenser, etc. are reciprocal at nominal signal levels [1].

Three-transducer spherical-wave reciprocity is the most commonly used reciprocity method to calibrate a microphone. During calibration, the microphones are coupled together by the air (gas) enclosed in a cavity. One microphone operates as a transmitter and emits sound into the cavity, which is detected by the receiver microphone. The dimensions of the cavity and the acoustic impedance of the microphones must be known, while the properties (pressure, temperature and composition) of the gas (air) in the coupler must be controlled or monitored in connection with the measurement. These parameters are used for the succeeding calculations of Acoustic Transfer Impedance and microphone sensitivity. Three microphones (A, B and C) are used (Figure 4.10). They are pair-wise (AB, BC and CA) coupled together. For each pair the receiver output voltage and the transmitter input current are measured and their ratio, which is called the Electrical Transfer Impedance is calculated. After having determined the electrical impedance and calculated the acoustic transfer impedance for each microphone combination, the sensitivities of all three microphones may be calculated by solving the equations below [6]:

$$M_{p,A} \times M_{p,B} = \frac{Z_{e,AB}}{Z_{a,AB}}; \quad (4.5)$$

$$M_{p,B} \times M_{p,C} = \frac{Z_{e,BC}}{Z_{a,BC}}; \quad (4.6)$$

$$M_{p,C} \times M_{p,A} = \frac{Z_{e,CA}}{Z_{a,CA}}; \quad (4.7)$$

where  $Z_{e,AB} = \frac{u_{AB}}{i_{AB}}$ ;  $Z_{e,BC} = \frac{u_{BC}}{i_{BC}}$ ;  $Z_{e,CA} = \frac{u_{CA}}{i_{CA}}$ .

( $M_{p,A}$ ,  $M_{p,B}$ ,  $M_{p,C}$ : pressure sensitivities of microphone A, B and C;

$Z_{a,AB}$ ,  $Z_{a,BC}$ ,  $Z_{a,CA}$ : acoustic transfer impedances of coupler with microphones AB, BC and CA;

$Z_{e,AB}$ ,  $Z_{e,BC}$ ,  $Z_{e,CA}$ : electrical transfer impedances of coupler with microphones AB, BC and CA.)

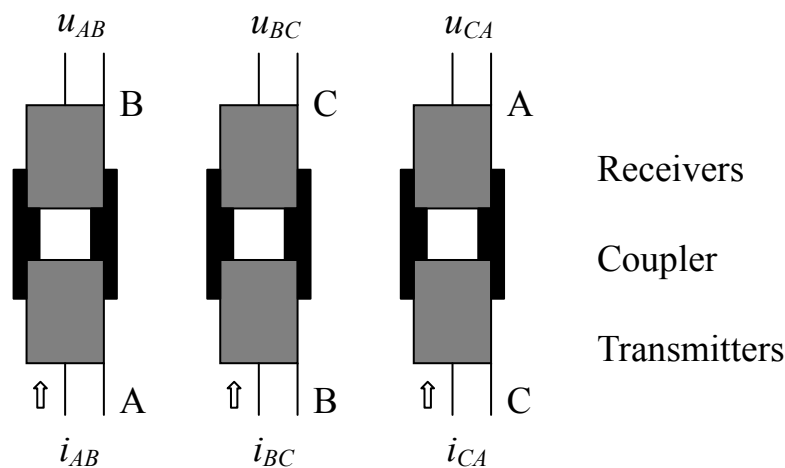


Figure 4.10: Principle of Pressure Reciprocity Calibration. The three microphones (A, B and C) are coupled two at a time together by the air (or gas) enclosed in a cavity while the three ratios of output voltage and input current are measured. Each ratio equals the Electrical Transfer Impedance valid for the respective pair of microphones.

#### 4.3.1.2 Substitution Method

The substitution method (also called a comparison calibration method) is a simple secondary calibration technique. When properly made, it is reliable and accurate. This method consists of subjecting the to-be-calibrated microphone and a calibrated reference or standard microphone to the same pressure field and then comparing the electrical output voltages of the two microphones [6]. Theoretically, the characteristics of the pressure field generator are irrelevant. It is necessary only that it produces sound of the desired frequency and of a sufficiently high signal level.

The standard microphone is immersed in the sound field. It must be far enough from the pressure source that it intercepts a segment of the spherical wave small enough (or having a radius of curvature large enough) that the segment is indistinguishable from a plane wave. Any nearby housing for preamplifiers or other components must be included in the dimensions of the microphone because the presence of such housing may affect the sensitivity.

Unless the standard microphone is omni-directional, it must be oriented so that its acoustic axis points toward the pressure source. The open-circuit output voltage  $V_s$  of the standard microphone in such a position and orientation is measured. The standard microphone then is replaced by the unknown microphone, and the open-circuit output voltage  $V_x$  of the unknown is measured. If the free-field voltage sensitivity of the standard is  $M_s$ , then the sensitivity of the unknown  $M_x$  is found from the following:

$$M_x = M_s \frac{V_x}{V_s} \quad (4.8)$$

A variation of the substitution method is the practice of simultaneously immersing both the standard and the unknown microphone in the medium and in the same sound field (also named the simultaneous method). Since the two microphones cannot be in the same position, this technique requires some assurance that the sound pressure at the two locations is the same, or has some known relationship. If the microphones are placed close together, the presence of one may influence the sound pressure at the position of the other, and if the microphones are placed far apart, reflections from boundaries and the directivity of the pressure source may produce unequal pressure at the two locations. If the boundary and medium conditions are stable, the relationship between the sound pressures at the two locations can be measured. The disadvantages of this variation usually outweigh the advantages, and the method is not used very much.

#### 4.3.1.3 Pulse Calibration Method

The reciprocity and substitution methods are well established to calibrate microphones in the audio frequency range (20Hz ~ 20kHz). However, they are difficult to apply in the wide-band high frequency microphone calibration area. As we described in the previous section, the microphone produced in this thesis is original and unique, which means no comparable microphone exists on the market. Therefore no commercial standard microphone can be used as the reference in the substitution calibration method, and this microphone can not be calibrated by the secondary method. Reciprocity is a primary method. However, that the microphone be reciprocal is a prerequisite, and the piezoresistive type aero-acoustic microphone does not meet this requirement.

The most difficult part of the primary calibration process is to know the exact pressure (force) applied to the microphone diaphragm. In the audio frequency range, this is achieved by using a piston-phone, which provides a constant and known volume velocity to a microphone, and in the lower ultrasonic frequency band (up to 100kHz), an electrostatic actuator (EA) is normally used to apply a known force to the microphone. The EA produces an electrostatic force, which simulates sound pressure acting on the microphone diaphragm. In comparison with sound based methods, the actuator method has a great advantage in that it provides a simpler means of producing a well-defined calibration pressure over a wide frequency range without the special facilities of an acoustics laboratory. However, the EA method requires an accessible, conductive diaphragm [7], which is not compatible with some kinds of microphones, including the piezoresistive type.

There is no single tone wide-band pressure source ( $> 100\text{kHz}$ ) on the market, and the simple reason is that no wide-band high frequency microphone in this range could be used to calibrate the source. Much work has been done in the calibration of acoustic emission (AE) devices in the ultrasonic range. These use a pulse or step force such as the Hsu-Nielsen method (also named as pencil lead breaking method) [8] or glass capillary breaking method [9], as a source. Figure 4.11 presents three kinds of pulse signal and their fast Fourier

transform. The basic idea of these methods is that the smaller the pulse duration is, the wider the flat band pressure that can be generated from the system.

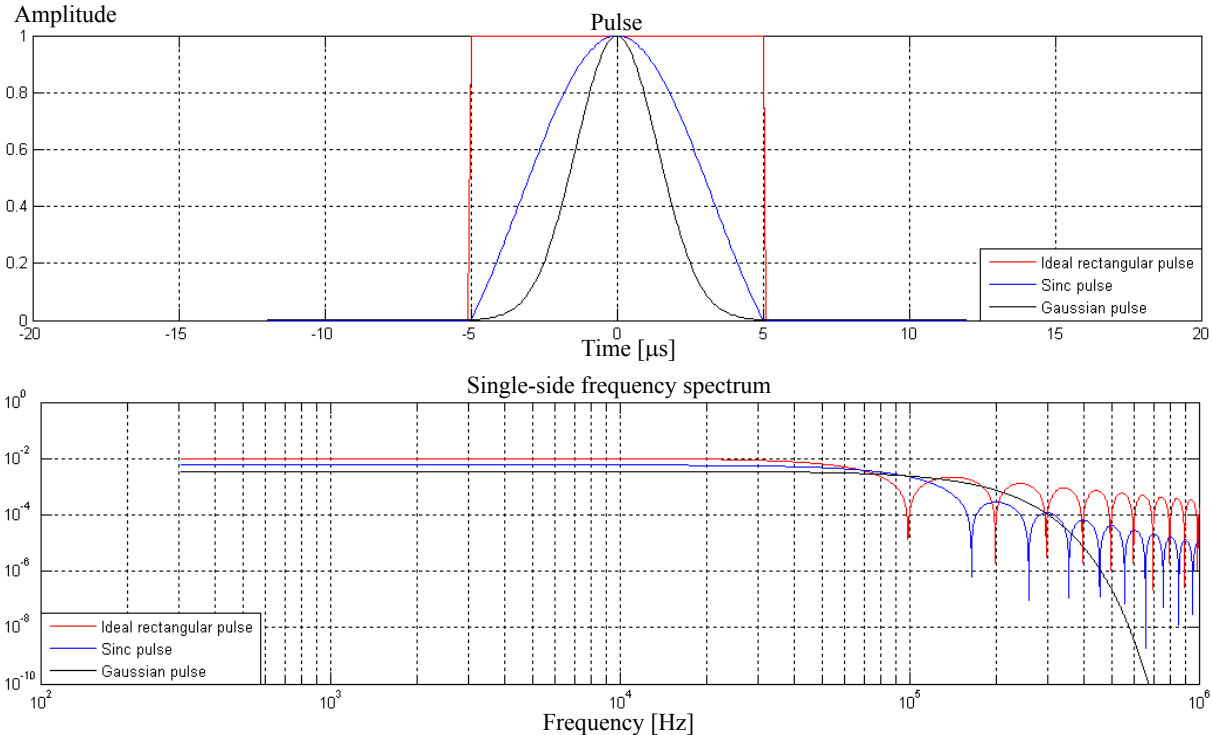


Figure 4.11: Pulse signals and their corresponding spectra.

Hsu-Nielsen and glass capillary breaking methods could not be directly used for the wide-band high frequency microphone calibration since they generate a pulse signal in the form of displacement, which is only suitable for an AE sensor. Considering the microphone calibration, a pulse signal in the pressure form should be generated and more specifically, the pressure pulse duration should be in the micro-second range, which makes the frequency bandwidth ~1MHz, and the pressure level should be adjustable for a large dynamic range, which matches the microphone specifications. Table 4.1[7] summarizes the methods to calibrate a microphone. Until now, the pulse calibration method has been the most suitable for a wide-band high frequency microphone.

Table 4.1: Summary of different microphone calibration methods.		
Method	Bandwidth	Limitations
Reciprocity	Low frequency	Microphone to be reciprocal
Substitution	Low frequency	Need calibrated reference
Piston-phone	Low frequency	Limited sound pressure level
EA	High frequency	Need conductive diaphragm
Pulse	High frequency	Not mature technique

### 4.3.2 The Origin, Characterization and Reconstruction Method of N Type Acoustic Pulse Signals

Figure 4.12 presents an ideal N type acoustic pulse signal (N-wave) in 10 $\mu$ s duration and its corresponding frequency spectrum. Even though the frequency spectrum is not flat, it still could be used as a pulse source to calibrate microphones. The work has been verified by Averiyarov [10].

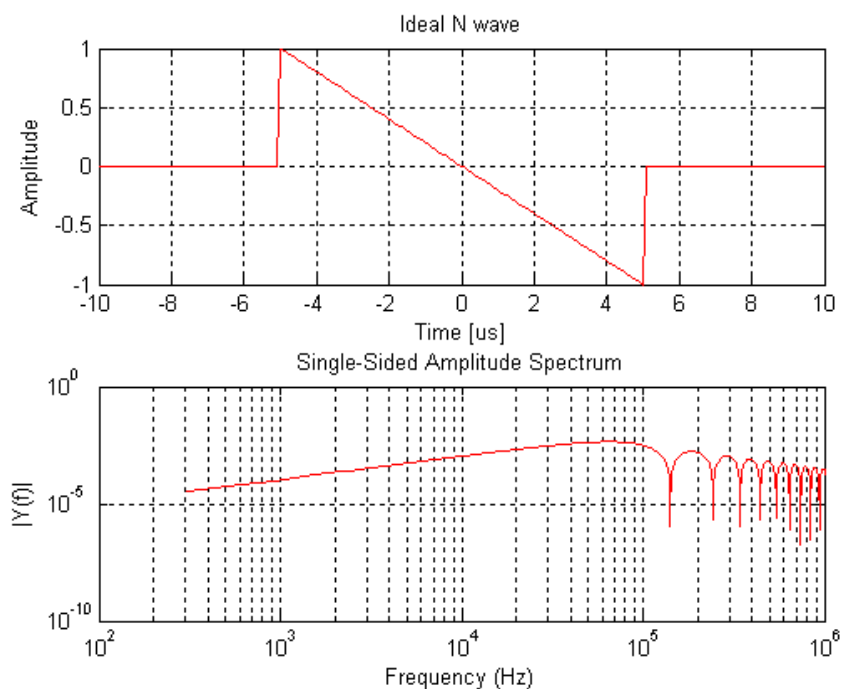


Figure 4.12: An ideal N-wave in 10  $\mu$ s duration and its corresponding frequency spectrum.



4.3.2.1 The Origin and Characterization of the N-wave

The origin of the discovery of the N-wave is from the study of small firearm bullets (Figure 4.13), but it has been found that the same mathematical expressions will describe the characteristics of the N-wave as a good approximation for supersonic projectiles of any sizes and shapes [11].

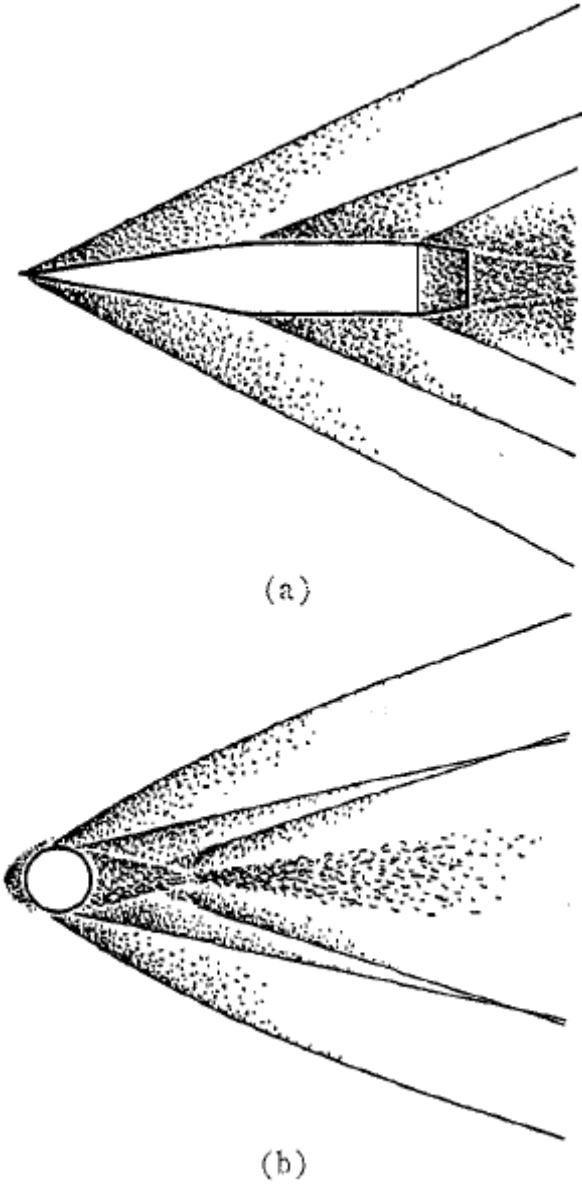


Figure 4.13: N-wave near projectile (a) Cone-cylinder, (b) Sphere.

Although the N-wave starts as a wave with considerably rounded contours, as illustrated schematically in Figure 4.14(a), it rapidly changes into an N shape wave such as that shown in

Figure 4.14(c). This is due to the fact that the particles of the medium in the compressed portions of the wave are traveling noticeably faster than normal sound velocity, while the particles in the rarefaction phase are traveling at slower velocities. Consequently, the high positive amplitudes arrive early at a given point and the high negative amplitudes arrive late. Thus, the wave steepens to have a sudden sharp rise, gradually diminishes to a point below the ambient pressure, and then suddenly recovers to ambient pressure at the end.

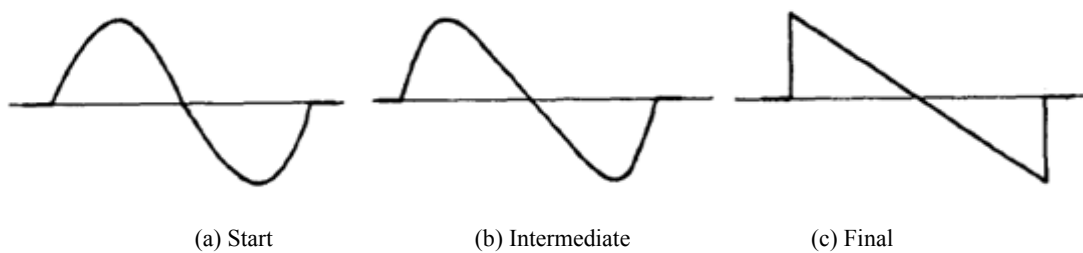


Figure 4.14: N-wave generation process.

To study and characterize the N-wave, it is good to use a full scale model, which means that when the generated N-wave is characterized, the original source is used. This is still possible or affordable for the N-wave source study which will not cost too much. However, when it is used as an acoustic source for microphone calibration, the cost will directly limit the number of trials and the results will also be affected by environmental factors, such as the temperature, humidity, background noise, etc. To get a more cost effective and repeatable N-wave, researchers have tried to build an artificial N-wave source for which the generation conditions can be easily controlled in a laboratory.

Many techniques have been investigated to generate the N-wave under laboratory scale conditions. The simplest way to generate the N-wave is from the bursting of a balloon [12]. When an initial spherical, uniform, static-pressure distribution is released, the acoustic disturbance that results has the N shape, which is predicted from the linear acoustic-wave equation with the appropriate boundary conditions. Generally two methods can be used to burst the balloon. The first method is to fill the balloon with air until it ruptures spontaneously, and the second one is to fill the balloon with air, seal it off just before the breaking point, and puncture it with a pin or any sharp object. Experiments show that the spontaneous rupture

tears the balloon into many small shreds, indicating a more complete disintegration of the skin. Thus, this method results in a closer approximation of a pressure distribution, which is released at all points.

A similar method, but with better controlled equipment, is the shock tube (Figure 4.15), which can be used to generate the N-wave under laboratory scale conditions also [13]. It consists, basically, of a rigid tube divided into two sections. These sections are separated by a gas-tight diaphragm, which is mounted normally to the axis. Initially, a significant pressure difference exists between the two sections. The high pressure section is called the compression chamber, while the low pressure section is known as the expansion chamber. When the diaphragm is ruptured, the pressure begins to equalize in the form of a shock wave (N-wave) moving into the expansion chamber and a rarefaction wave moving into the compression chamber.

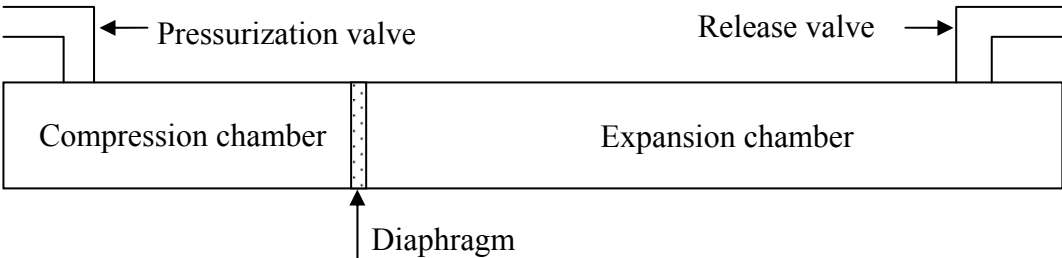


Figure 4.15: Schematic of the shock tube.

Other methods such as using a laser as a focused electromagnetic energy source to burn the target and generate the N-wave have also been reported [14-16]. However, the most commonly used method is generation from a high voltage electrical spark. This method is a robust way to generate an intense acoustic pulse that acts independently of the acoustic matching between the emitter and medium. It is far less sensitive to any contamination. In addition the directivity pattern is essentially omni-directional in the equatorial plane, and the acoustic characteristics have proven to be repeatable for successive sparks. Studies on the acoustic wave that occurs after a spark discharge in air have been performed [17, 18], and this method is even used to act as an ultrasonic generator in the flow measurement situation [19].

A simple spark discharge circuit is shown in Figure 4.16 [20]. A high voltage power supply

(~14kV) charges a storage capacitor (1nF) through a current limiting resistor (50MΩ), and the discharge of the capacitor occurs through the spark gap (~1.3cm), which may reach one ohm of resistance or less during discharge. The process of electrical breakdown may be outlined as follows. When the voltage across the gap reaches a sufficiently high potential (breakdown voltage), causing ionization in the air around the gap, a very narrow cylindrical region between the gap becomes a good conductor. The energy stored in the circuit surges through this region, often raising the temperature to several thousand degrees Kelvin. This results in the rapid expansion of the spark channel, forming a cylindrical shock ahead of it. The initial shock usually pulls away from the spark channel within 1 micro-second, and the shock front is first observed to be ellipsoidal, with its major axis along the axis of the spark. Within 10 micro-seconds, however, it assumes a nearly perfect spherical shape.

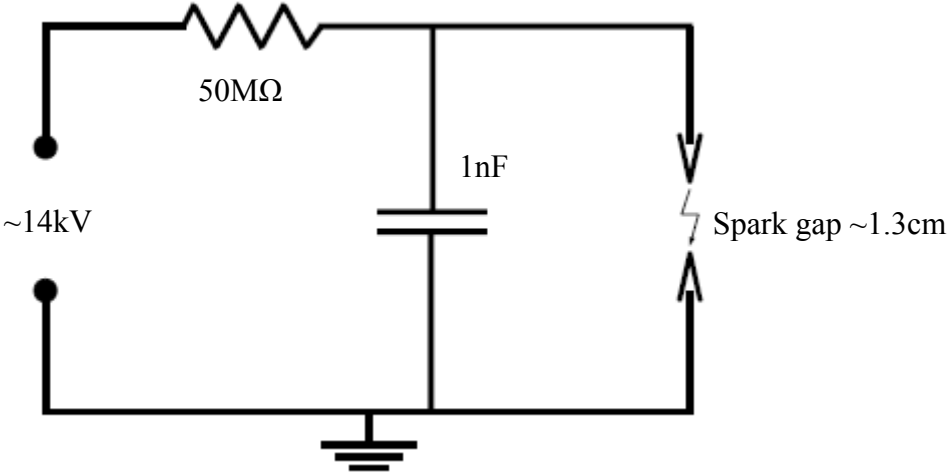


Figure 4.16: High voltage capacitor discharge scheme.

Figure 4.17 shows an ideal N-wave generated by the electrical spark discharge, which is characterized by two parameters, the half duration  $T$  and the overpressure  $P_s$ . The intensity of the spark is controlled by the electrical energy stored in the capacitor:

$$E_0 = \frac{1}{2} CV^2, \tag{4.9}$$

where  $E_0$  is the stored electrical energy,  $C$  is the capacitor for energy storage and  $V$  is the charging voltage. By simplifying the spark source to appear as a point source producing a

spherical omni-directional wave at normal room temperature, Wyber [18] theoretically estimates the electrical to acoustical energy transform efficiency to be  $\sim 0.07$ , as shown in Equation (4.10):

$$E_A \approx 0.07 E_0, \quad (4.10)$$

where  $E_A$  is the generated acoustical energy from the electrical spark discharge, in the unit of joule.

Plooster [21] characterizes the relationship between the overpressure and the released energy in Equation (4.11):

$$P_s = \frac{2}{b(\gamma+1)} \frac{E_u}{r^2} \delta, \quad (4.11)$$

where  $E_u$  is the energy released per unit length of the source,  $\gamma$  is the air specific heat ratio which is equal to 1.4,  $b$  is a parameter which is only dependent upon  $\gamma$  and is found to be 3.94,  $r$  is the distance between the location of the calculated overpressure and the source and  $\delta$  is unity under the strong shock solution.

The half duration  $T$  is proportional to the spark gap distance. To summarize, the acoustic overpressure generated by the electrical spark discharge is proportional to the released energy. The larger spark gap needs higher voltage to break down the air, which leads to larger released energy and in turn a higher acoustic overpressure. But on the other hand, the larger spark gap will also lead to a larger half duration of the N-wave, which will limit the frequency information. A typical spark with  $\sim 11\mu\text{s}$  half duration and 2.3kPa overpressure at 10cm propagation distance is recorded by Wright [17].

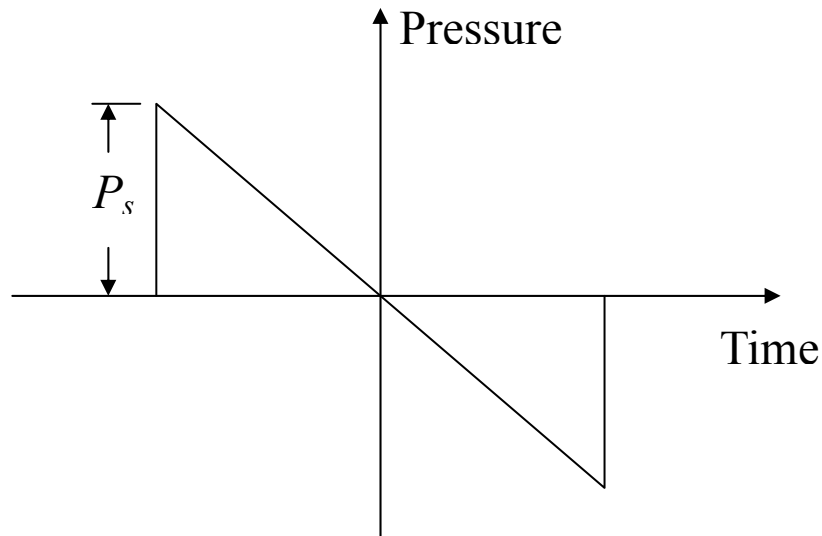


Figure 4.17: Schematic of an ideal N-wave.

#### 4.3.2.2 N-wave Reconstruction Method

To accurately calibrate a microphone, it is important to know the exact shape of the N-wave generated in our laboratory conditions. Figure 4.18 presents a real N-wave and the shape of this real N-wave is decided by three parameters: the half duration  $T$ , the overpressure  $P_s$  and the rise time  $t$  (defined as the time interval from  $10\%P_s$  to  $90\%P_s$ ).

The rise time  $t$  of the N-wave is measured by focused shadowgraphy. By using the shadowgraphy technique, the distribution of light intensity in space is photographed and then analyzed. The pattern of the light intensity is formed due to the light refraction in non-homogeneities of the refraction index caused by variations of medium density. Shadow images called shadowgrams are captured by a camera at some distance from the shock wave by changing the position of the lens focal plane.

The setup designed for this optical measurement is shown in Figure 4.19 [22]. It is composed of a 15kV high voltage spark source, which is used to generate an acoustic N-wave; a B&K wideband microphone (type 4137, cut-off frequency  $\sim 200\text{kHz}$ ), which is used to determine the N-wave amplitude and duration and deduce the theoretical rise time using a Generalized

Burgers equation; and optical equipment including a flash-lamp, light filter, lens and a digital CCD camera. These pieces of optical equipment were mounted on a rail and aligned coaxially. The flash-lamp generated short duration (20ns) light flashes that allowed a good resolution of the front shock shadow. The focusing lens was used to collimate the flash light in order to have a parallel light beam. The dimension of the CCD camera was 1600 pixels along the horizontal coordinate and 1186 pixels along the vertical coordinate. The lens was used to focus the camera at a given observation plane perpendicular to the optical axis. Compared to the rise time deduced from the microphone measurement, the optical measurement result matches better with the theoretical estimation (Figure 4.20) [22], which verifies that the rise time result is limited by the frequency bandwidth of the microphone used.

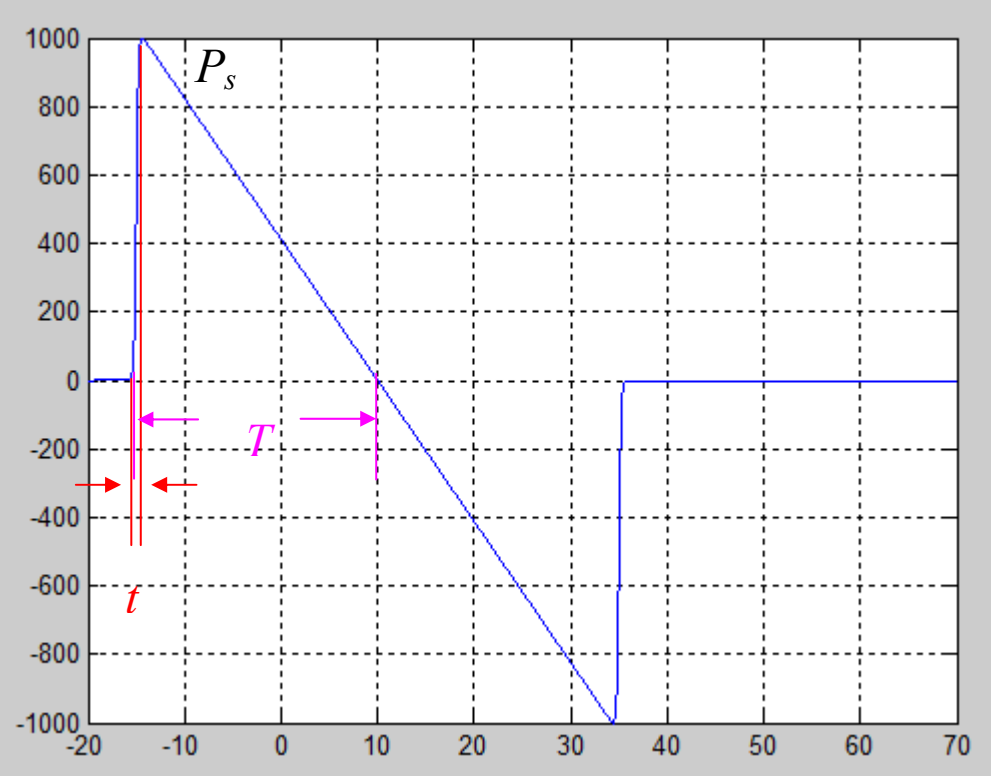


Figure 4.18: Real N-wave shape.

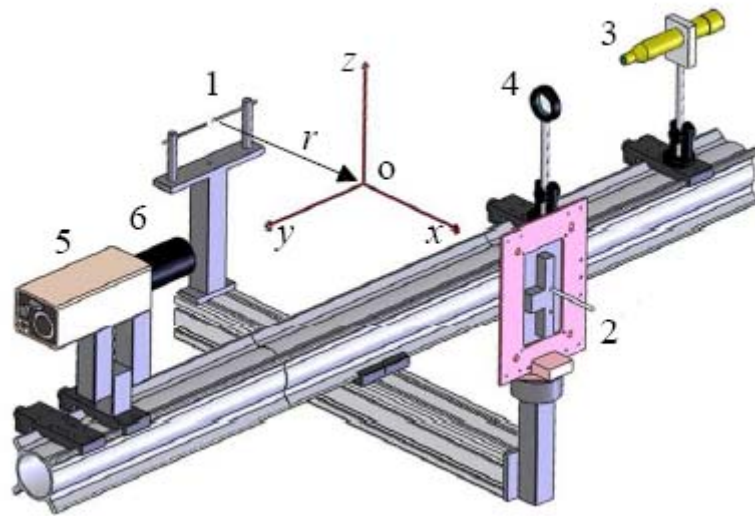


Figure 4.19: Shadowgraph experiment setup (1. spark source, 2. microphone in a baffle, 3. nanolight flash lamp, 4 focusing lens, 5. camera, 6. lens).

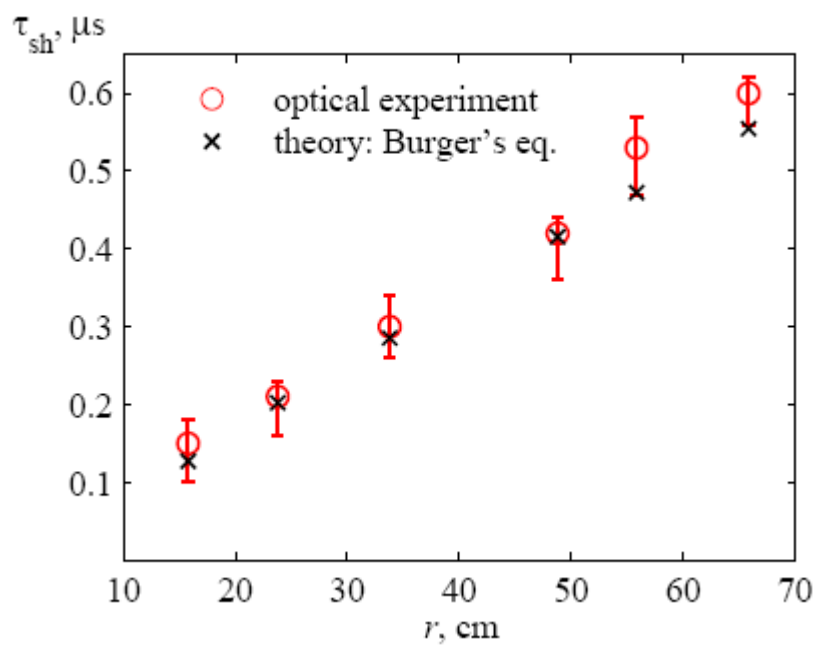


Figure 4.20: Comparison between the optically measured rise time and the predicted rise time by using the acoustic wave propagation at different distances from the spark source.

The half duration  $T$  of the N-wave, normally around  $20\mu\text{s}$ , which equivalents to 25kHz in frequency spectrum, can be directly measured by a B&K microphone type 4138 with a bandwidth of 140kHz.



To know the overpressure  $P_{s0}$  at distance  $r_0$  from the spark source, at first, the half duration  $T_0$  at distance  $r_0$  is measured. Then, by varying the distance  $r$ , a series of N-wave half duration values  $T$  at corresponding distance  $r$  are recorded. For a spherical N-wave, weak shock theory gives the following evolution law for the half duration [23]:

$$T(r) = T_0 \sqrt{1 + \sigma_0 \ln\left(\frac{r}{r_0}\right)}; \quad (4.12)$$

$$\sigma_0 = \frac{(\gamma + 1)r_0 P_{s0}}{2\gamma P_{atm} c_0 T_0}, \quad (4.13)$$

where  $\gamma = 1.4$  is the ratio of the specific heat for gas,  $P_{atm}$  is the atmospheric pressure and  $c_0$  is the sound speed. From Equation (4.12), the coefficient  $\sigma_0$  shows the dependence of half duration  $T$  to the initial overpressure at distance  $r = r_0$ . As we have already recorded a series of half duration  $T$  at different distances  $r$ , the parameter  $(T/T_0)^2 - 1$  is plotted as a function of  $\ln(r/r_0)$ . Then, the slope of the linear fitted line is the coefficient  $\sigma_0$ . Once the coefficient  $\sigma_0$  is obtained, the overpressure  $P_{s0}$  can be calculated by Equation (4.14):

$$P_{s0} = \frac{\sigma_0 2\gamma P_{atm} c_0 T_0}{(\gamma + 1)r_0}. \quad (4.14)$$

### 4.3.3 Spark-induced Acoustic Response

As we found from the static nano-indentation measurement, the sensitivity of the sample is very low. So, an amplification card was connected to the sensor output to boost the signal and make it large enough for the oscilloscope to capture. Figure 4.21 shows the schematic of the amplification card connecting to the sensor. The card is composed of a two-stage configuration with two identical instrumentation amplifiers (INA103). The first stage is a pre-amplifier directly connected to the sensor output with a gain of 10. A high pass filter with -3dB cut-off frequency at 1kHz is inserted in between the first stage and the second stage ( $C = 10\text{nF}$ ,  $R = 15\text{k}\Omega$ ). This high pass filter blocks the possibly amplified DC off-set signal

originally from the sensor to prevent voltage saturation of the second stage, which has a large gain of 100. The frequency response of the amplification card is shown in Figure 4.22. With a real gain of 58dB, the -3dB cut-off frequency is 600kHz.

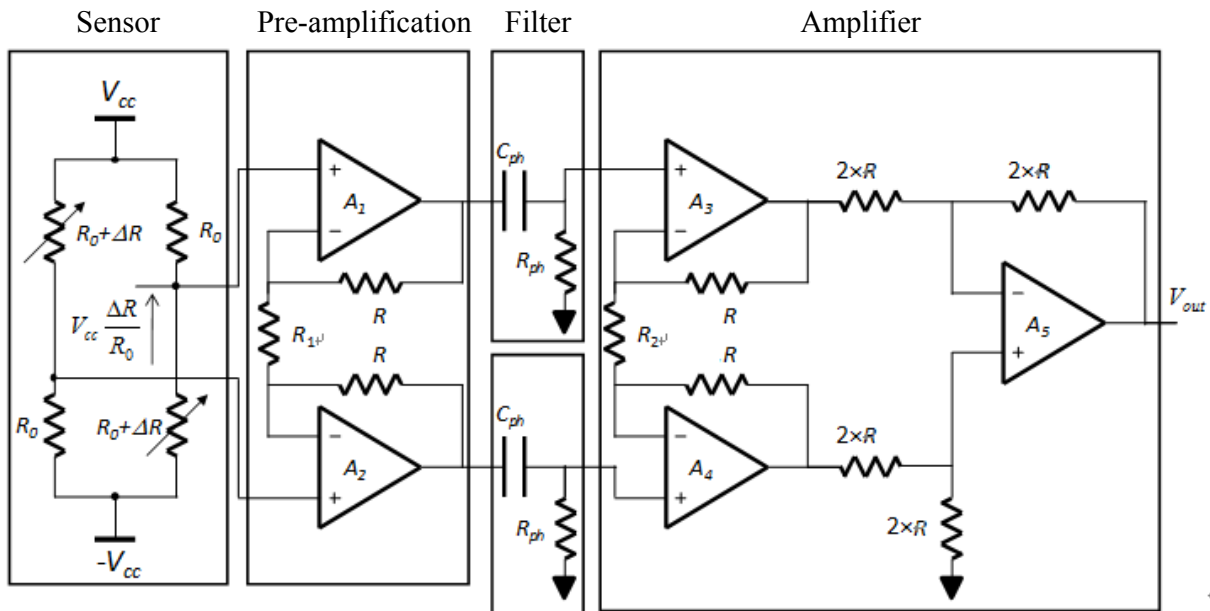


Figure 4.21: Schematic of the amplifier.

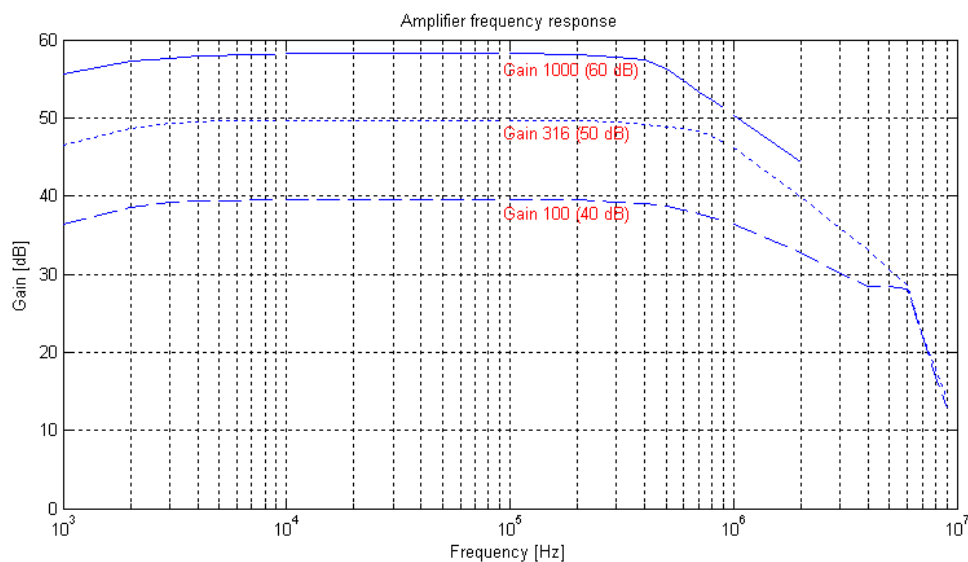


Figure 4.22: Frequency response of the amplification card.

The dynamic calibration setup is shown in Figure 4.23. The spark discharging circuit is configured the same as Figure 4.16. The microphone sample is glued to a PCB and wire bonded. The PCB is then put into a baffle, which is used to eliminate the acoustic reflection

effect due to the PCB edge. The baffle is specially designed so that it allows the PCB to be surface mounted into it (Figure 4.24). The gap between the PCB and the surrounding baffle is covered by Scotch tape.

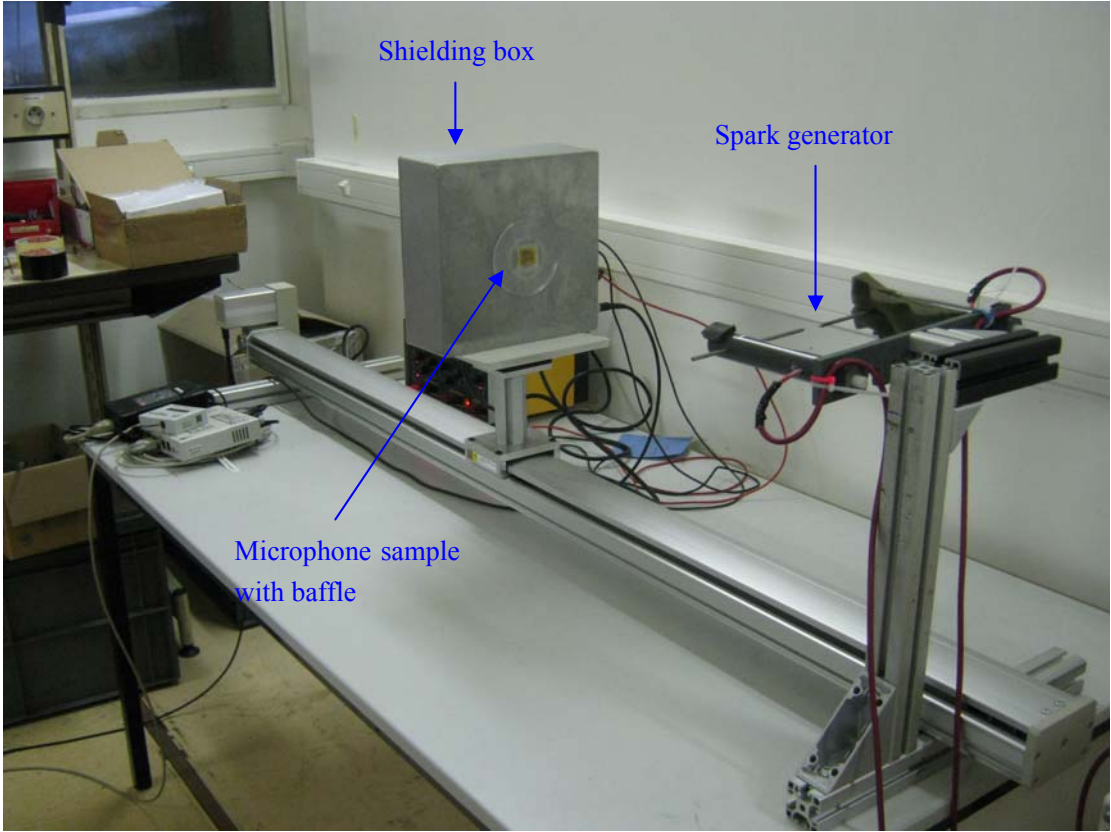


Figure 4.23: Spark calibration test setup.

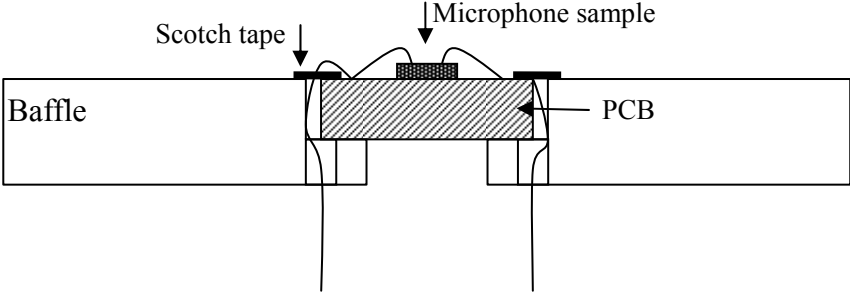


Figure 4.24: Baffle design.

The amplification card was put into an aluminum shielding box, which prevented the strong electromagnetic interference generated by the electrical discharge. The to-be-calibrated microphone sample was connected to the amplification card through a small hole in the shielding box front surface. Finally, the shielding box was placed on top of a stage which could move along the guided rail and be controlled through LabVIEW software.

#### 4.3.3.1 Surface Micromachined Devices

After discovering the exact N-wave shape at distance  $r_0$  away from the spark source, our to-be-calibrated samples were placed at the same distance. A typical measured N-wave signal using surface micromachining devices is shown in Figure 4.25. From the figure, we can clearly find two consecutive oscillation signals. The first oscillation corresponds to the sharp rise of the front shock of the N-wave, and the second oscillation corresponds to the sharp rise of the rear shock of the N-wave. However, the low frequency information of the N-wave, corresponding to the slope from the front shock to rear shock cannot be seen in the measured curve. This also verifies the low frequency information loss due to the acoustic short path effect, which is predicted in the finite element modeling. At the same time, we find that due to the fact that this device is only sensitive to the high frequency signal, which is related to the sharp upward rise step in the signal time domain, both the first and second measured oscillations start with an upward curve. The single-sided spectra of the measured signals from the microphone and from the optical method are obtained by applying fast Fourier transform (FFT) to the time domain signals (Figure 4.26). The frequency response (electrical sensitivity, in the unit of V/Pa) is defined by Equation 4.15. When using decibel (dB) in the logarithmic unit (referring to 1V/Pa), Equation 4.15 is changed to Equation 4.16 and the frequency response can be calculated by directly subtracting the green curve in Figure 4.26 from the blue curve.

$$\text{Electrical sensitivity} = \frac{\text{Voltage output}}{\text{Input pressure}} \quad (\text{V/Pa}) \quad (4.15)$$

$$\begin{aligned} \text{Electrical sensitivity} &= 20 \cdot \log\left(\frac{\text{Voltage output (V)}}{\text{Input pressure (Pa)}}\right) \\ &= 20 \cdot [\log(\text{Voltage output (V)}) - \log(\text{Input pressure (Pa)})] \quad (4.16) \\ &= 20 \cdot \log(\text{Voltage output (V)}) - 20 \cdot \log(\text{Input pressure (Pa)}) \\ &= \text{Voltage (dB)} - \text{Input pressure (dB)} \end{aligned}$$

The frequency response of the calibrated microphone is shown in Figure 4.27, which is also compared with FEA result. The resonant peak is about 400kHz, which is the same as the

prediction of the FEA result. The flat band is very narrow, roughly from 100kHz to 200kHz and below 100kHz, the frequency response is quickly decreased. The dynamic sensitivity within the flat band is  $0.033\mu\text{V/V/Pa}$ , which is much lower than the static value ( $0.4\mu\text{V/V/Pa}$ ). This phenomenon could also be explained by the acoustic short path effect (Figure 4.28). Using the N-wave reconstruction method, we can accurately find the incident pressure  $P_0$  to the sensing diaphragm. But the real pressure difference  $\Delta p$  on the sensing diaphragm is equal to  $P_0 - P_s$  ( $P_s$  is the leaked pressure into the air cavity through the release holes/slots), which is difficult to predict.

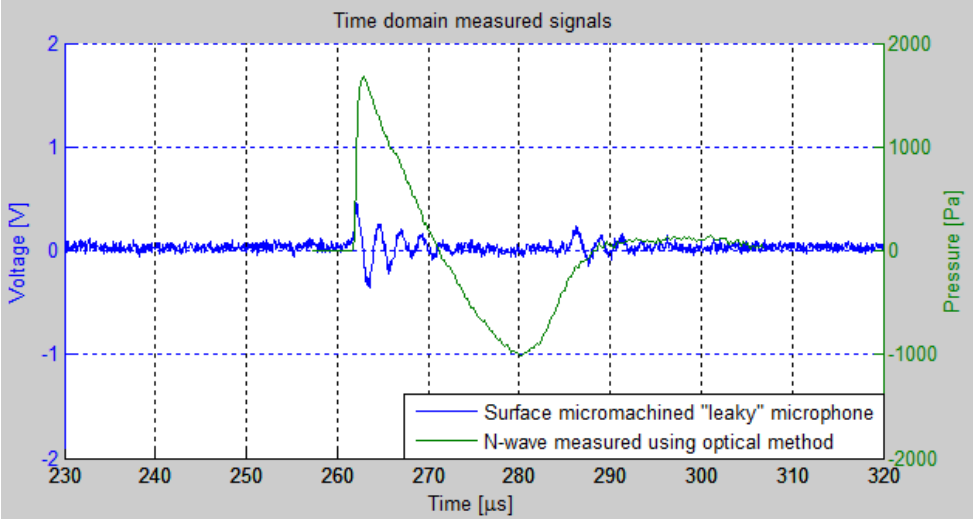


Figure 4.25: Typical spark measurement result of a microphone sample fabricated using the surface micromachining technique (3V DC bias, with amplification gain 1000 and source to microphone distance is 10cm).

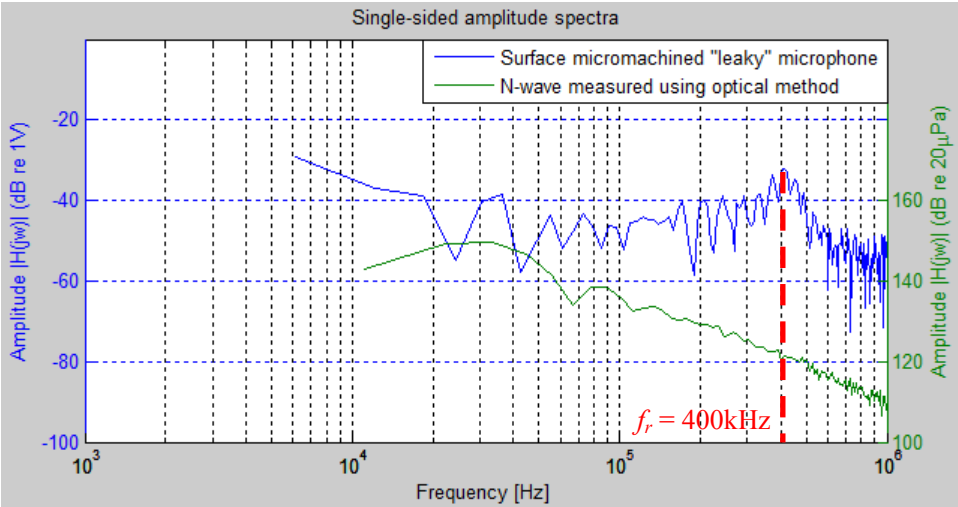


Figure 4.26: FFT single-sided amplitude spectra of the measured signals from a surface micromachined microphone and from the optical method.

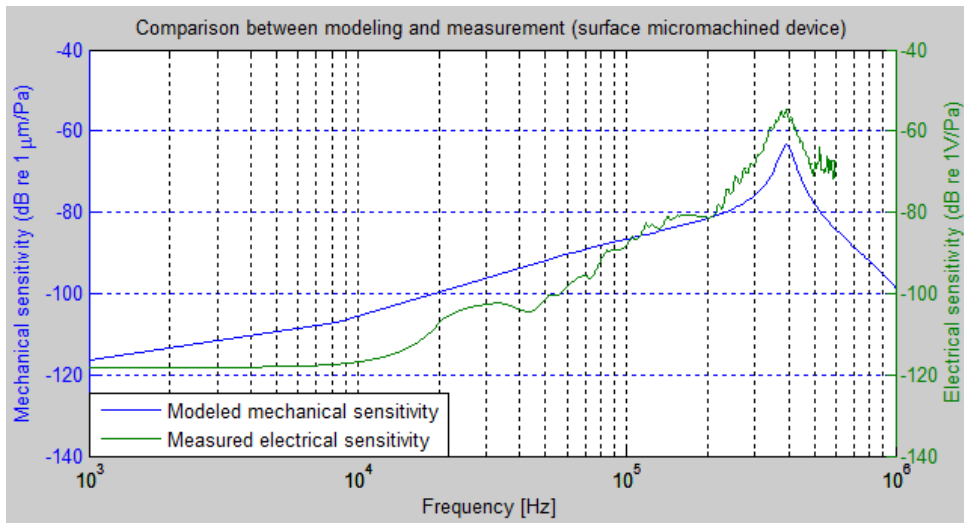


Figure 4.27: Frequency response of the calibrated microphone (3V DC bias, with amplification gain 1000, averaged signal), compared with FEA result.

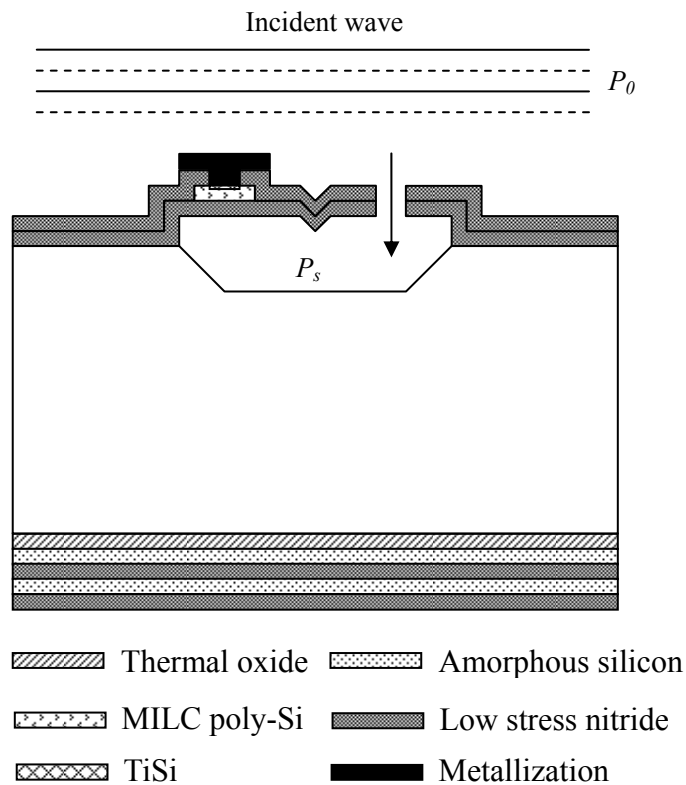


Figure 4.28: Acoustic short circuit induced leakage pressure  $P_s$ .

### 4.3.3.2 Bulk Micromachined Devices

Figure 4.29 shows the typical measured N-wave signal using bulk micromachining devices, and Figure 4.30 presents the corresponding spectra calculated using the FFT algorithm. From Figure 4.30, we can see that the bulk micromachining devices have a larger resonant frequency (715kHz) and from Figure 4.29, we can see that not only the high frequency information, but also the low frequency information can be caught by this device (the slope from the front shock of the N-wave to the rear shock of the N-wave). Also, we can see that there is an oscillation superimposed on the slope, which means that the microphone device is not sufficiently damped at its resonant frequency.

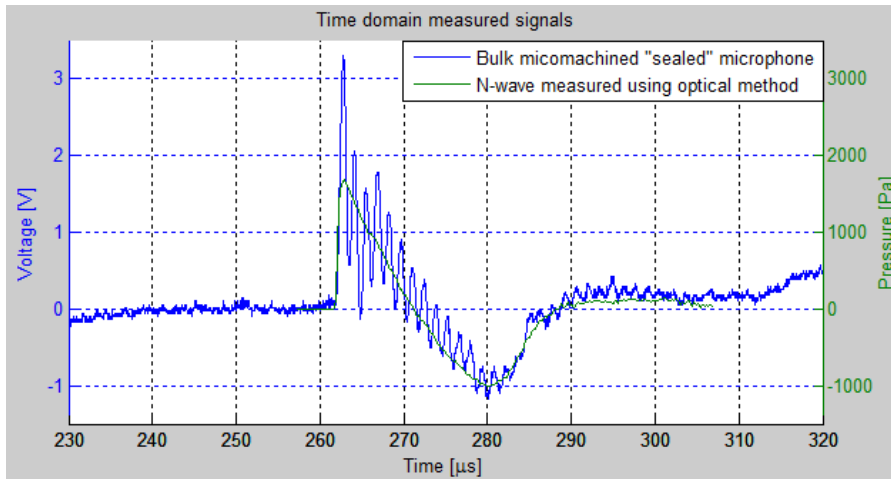


Figure 4.29: Typical spark measurement result of a microphone sample fabricated using the bulk micromachining technique (3V DC bias, with amplification gain 1000 and source to microphone distance is 10cm).

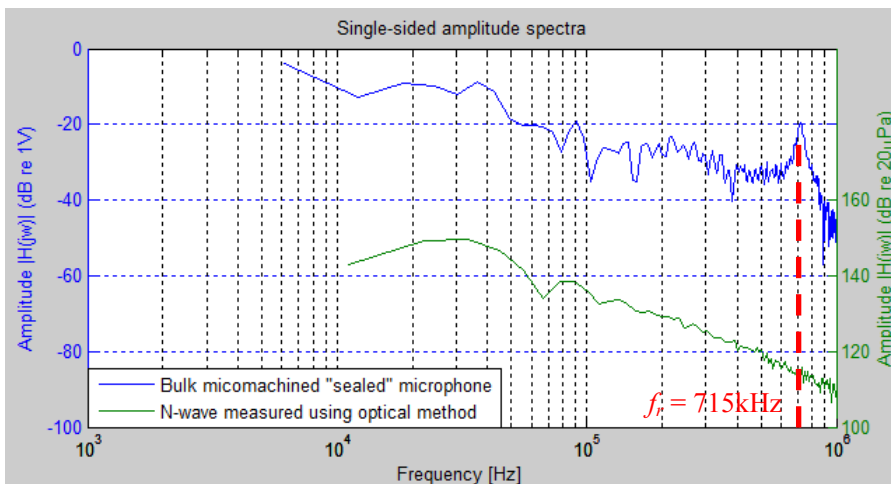


Figure 4.30: FFT single-sided amplitude spectra of the measured signals from a bulk micromachined microphone and from the optical method.

Again, using the calculation method mentioned in the previous section, the frequency response of the bulk micromachining devices is shown in Figure 4.31 and is compared with the lumped-element modeling result. The dynamic sensitivity is 1mV/Pa (with amplification gain 1000 and 3V DC bias), which means that the real microphone dynamic sensitivity is about 0.33 $\mu$ V/V/Pa and is similar to the static calibrated sensitivity (0.28 $\mu$ V/V/Pa). Also this microphone has a wide flat bandwidth from 6kHz up to 500kHz. However, compared to the lumped-element model, the measured resonant frequency is a little smaller. This phenomenon is possibly caused by the LS-SiN material properties variations between different fabrication batches. The material properties used in the lumped-element modeling were measured from the test batch, while the real device was fabricated 6 months later.

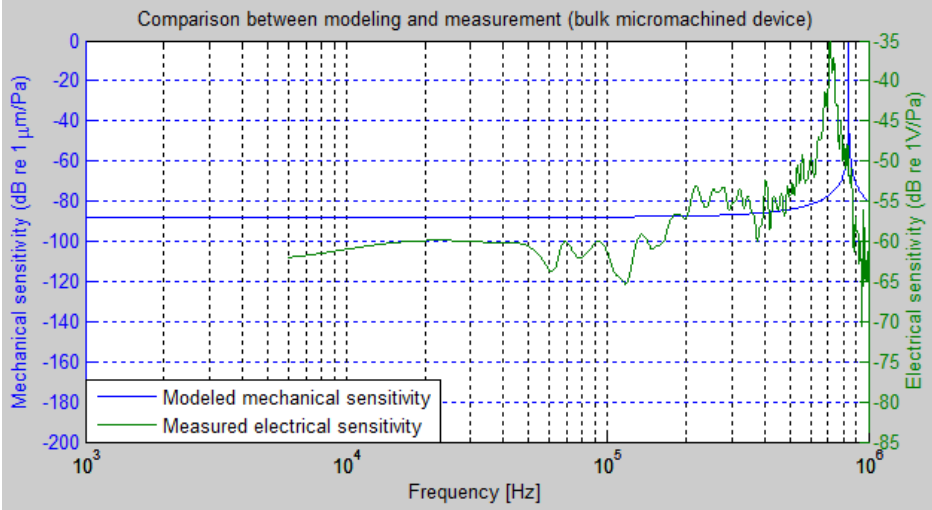


Figure 4.31: Frequency response of the calibrated microphone (3V DC bias, with amplification gain 1000, averaged signal), compared with lumped-element modeling result.

Finally, the spark measurement results of these two microphones compared with the optical measured signal are shown in Figure 4.32, and the comparison of the frequency responses are presented in Figure 4.33.



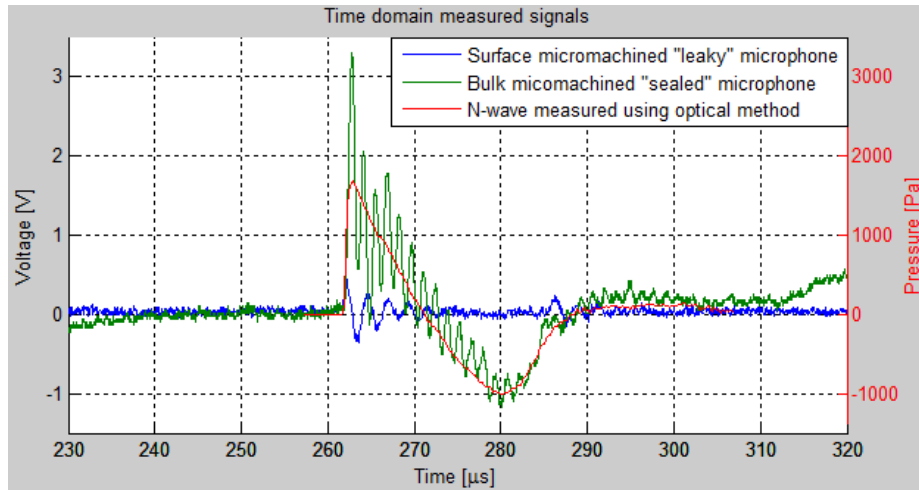


Figure 4.32: Comparison of the spark measurement results of microphones fabricated by two different techniques (spark source to microphone distance is 10cm).

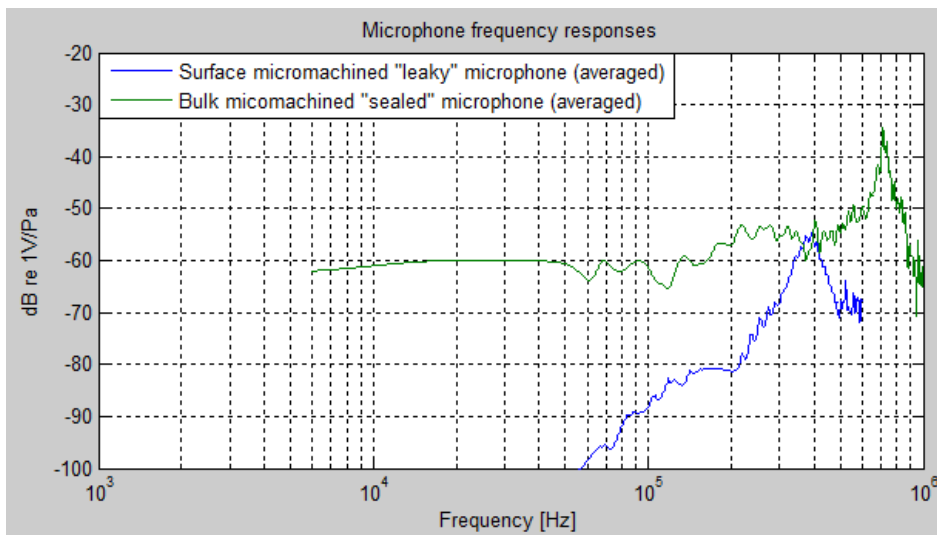


Figure 4.33: Comparison of the frequency responses of microphones fabricated by two different techniques.

## 4.4 Sensor Array Application as an Acoustic Source Localizer

To calculate an acoustic source in a Cartesian coordinate system (Figure 4.34) with three unknown parameters  $x$ ,  $y$  and  $z$ , we need three equations to solve (as shown in Equation 4.17), where  $(x, y, z)$  are the acoustic source coordinates,  $(x_{i,i=1,2,3}, y_{i,i=1,2,3}, z_{i,i=1,2,3})$  are the three sensor coordinates and  $d_{i,i=1,2,3}$  are the distances between the acoustic source and each sensor. These distances are calculated using Equation 4.18, where  $v$  is the sound velocity and  $t_{i,i=1,2,3}$  are the acoustic wave's travelling time from the source to each sensor.

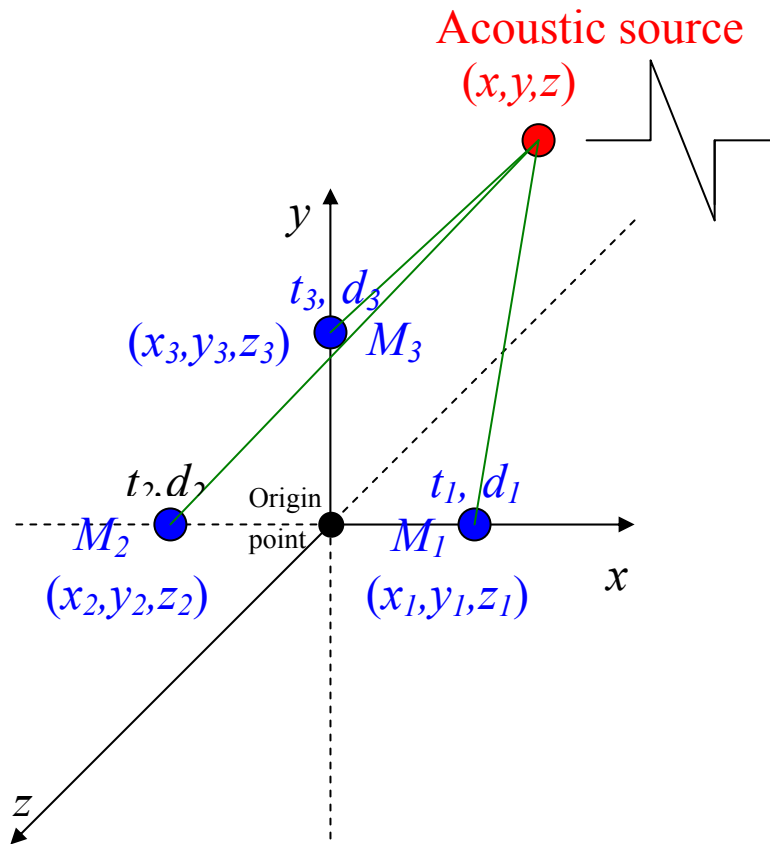


Figure 4.34: Cartesian coordinate system for acoustic source localization.

$$\begin{cases} (x-x_1)^2 + (y-y_1)^2 + (z-z_1)^2 = d_1^2 \\ (x-x_2)^2 + (y-y_2)^2 + (z-z_2)^2 = d_2^2 \\ (x-x_3)^2 + (y-y_3)^2 + (z-z_3)^2 = d_3^2 \end{cases} \quad (4.17)$$

$$\begin{cases} d_1 = t_1 \cdot v \\ d_2 = t_2 \cdot v \\ d_3 = t_3 \cdot v \end{cases} \quad (4.18)$$

Three sensors were placed in one plane to form an array, as shown in Figure 4.34 and Figure 4.35. The first sensor ( $M_1$ ) has a coordinate of  $x_1 = 2.5$ ,  $y_1 = 0$  and  $z_1 = 0$ ; the second sensor ( $M_2$ ) has a coordinate of  $x_2 = -2.5$ ,  $y_2 = 0$  and  $z_2 = 0$  and the third sensor ( $M_3$ ) has a coordinate of  $x_3 = 0$ ,  $y_3 = 4$  and  $z_3 = 0$ , all in the unit of centimeter.

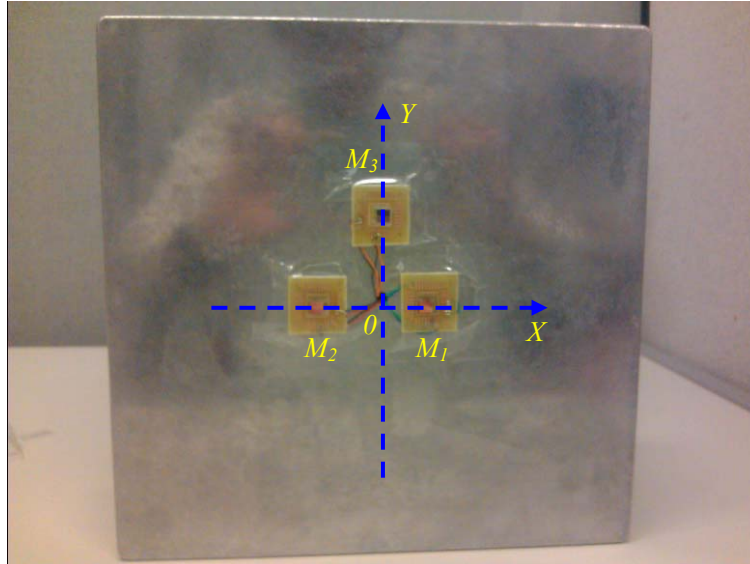


Figure 4.35: Sensor array coordinates.

The sound velocity  $v$  is a key parameter in the coordinate calculation process and it is sensitive to the environmental parameters, such as ambient pressure, temperature and humidity. So, before location coordinate calculation, the sound velocity  $v$  should be well calibrated. The acoustic source was fixed at the  $XY$  plane ( $x_o, y_o$ ) with  $Z$  coordinate  $z_o = 0$ , and one microphone was placed with the same  $X$  and  $Y$  coordinates ( $x_o, y_o$ ), while the  $Z$  coordinate  $z_m$  changed from 10cm to 105cm (Figure 4.36). The acoustic signal captured by the sensor was recorded by an oscilloscope. The acoustic source was the spark generator, as mentioned in the previous section, and the oscilloscope was triggered by the electromagnetic signal from the spark. As the electromagnetic signal travels at a speed of  $3 \times 10^8$  m/s, which is much faster than the speed of sound, the sound travelling time was calculated using the delay time between the oscilloscope trigger point time and the recorded signal arrival time.

The sound travelling distance vs. travelling time is shown in Figure 4.37. The velocity is extrapolated by linearly fitting the measured data, and the value is 344.2m/s. From the linear

fitting curve, we also find an offset of 2.1mm when time is equal to zero, which could come from a system setup error.

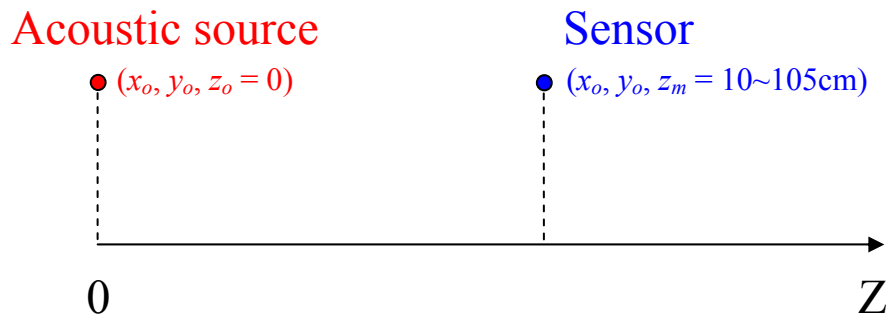


Figure 4.36: Sound velocity calibration setup.

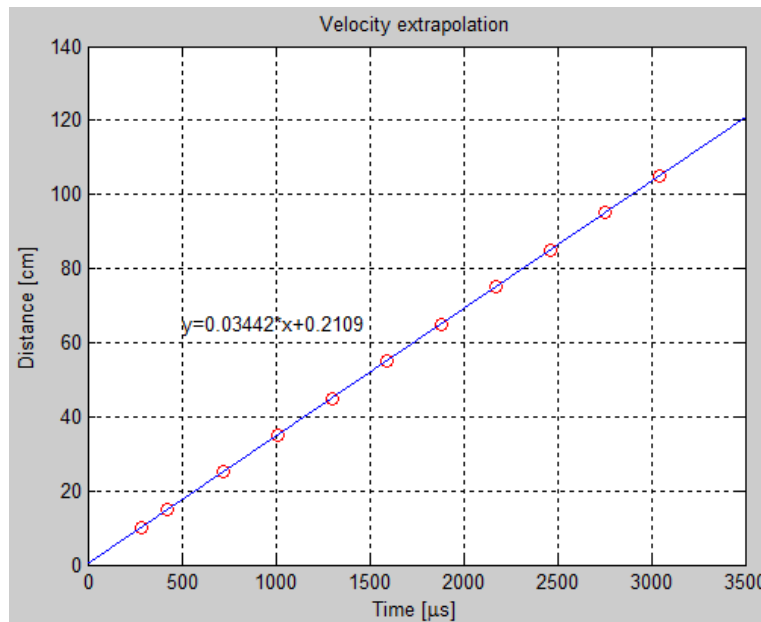


Figure 4.37: Sound velocity extrapolation.

Figure 4.38 presents the setup for the acoustic source localization application. The spark generator emitted an acoustic wave, which was sensed by the sensor array. The sensed signals were captured by an oscilloscope (Tektronix TDS 2024C) and then the captured signals were transferred to a laptop through a USB cable using the MATLAB Instrument Control Toolbox, which is based on the National Instruments Virtual Instrument Software Architecture (NI-VISA) standard. Then the delay times and the acoustic source coordinates were calculated by MATLAB software. All of these functions were realized by a customized MATLAB graphic user interface (GUI).

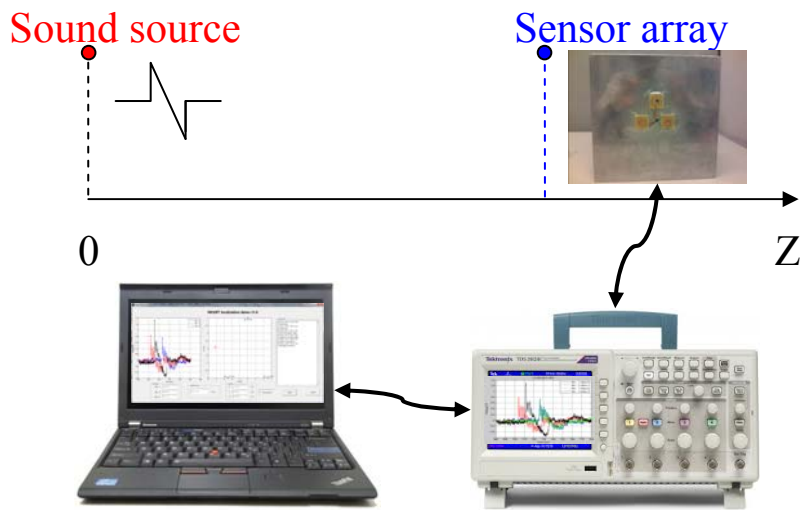


Figure 4.38: Acoustic source localization setup.

During the GUI initialization, firstly, the sound velocity was required to be input, otherwise, the default value of 340m/s would be used (Figure 4.39). After initialization, the main window, as shown in Figure 4.40, popped up. The main window consists of three parts: the main figures showing the captured acoustic signals and source locations projected in the  $XY$  plane (marked by the red dashed line in Figure 4.40); the boxes showing the calculated delay times of each signal, the input sound velocity and the calculated source coordinates (marked by the pink dashed line in Figure 4.40) and session log information and functional buttons (marked by the blue dashed line in Figure 4.40). The “Connection” button was used to initialize the communication between the GUI and the oscilloscope, and the “Start” button was used to initiate the data transfer from the oscilloscope to the MATLAB software and the following data processing.

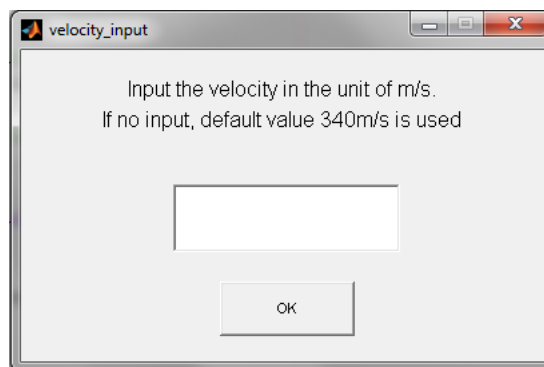


Figure 4.39: GUI initialization for sound velocity input.

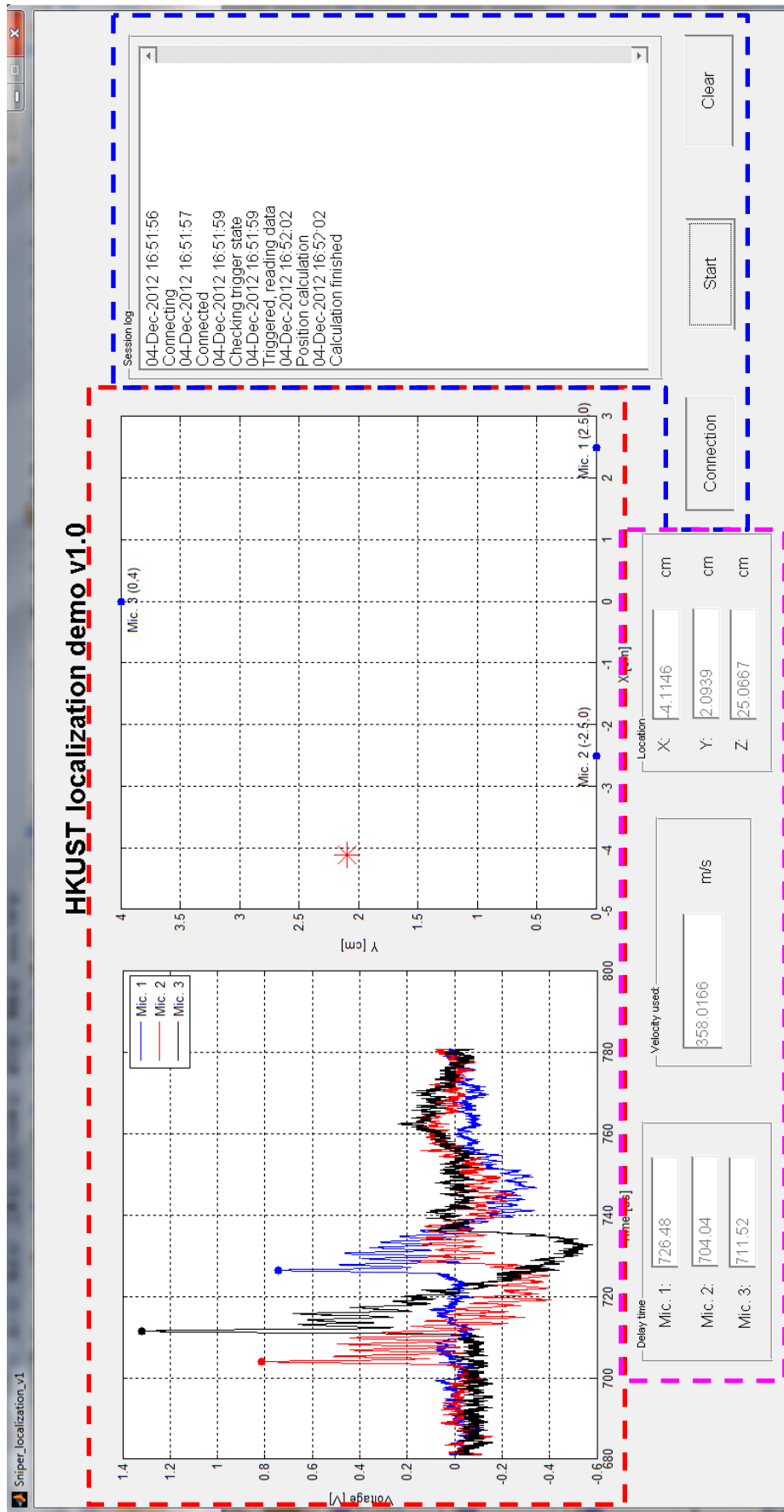


Figure 4.40: Localization GUI main window.

During the localization test, the spark source was fixed at one position and the sensor array was moving in the Z direction. But the origin of the Z coordinate was always the sensor array plane, as shown in Figure 4.34 and Figure 4.41, which was equivalent to the setup in which the sensor array was fixed at the coordinate origin and the sound source was moving. The reason for this setup arrangement is simply that the high voltage cable connecting the voltage generator and spark needles is not long enough.

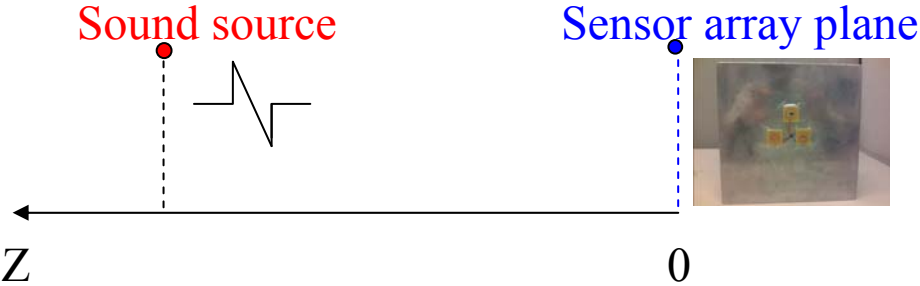


Figure 4.41: Localization test of the Z coordinate system.

The spark sound source was preset at the coordinates of  $(x_s = 0\text{cm}, y_s = 4\text{cm})$  in the XY plane. Because the two spark needles had a gap of 1.3cm, the middle position of the gap was assumed to be the source position (Figure 4.42). The distance between the sound source and the sensor array in the Z coordinate was changing from 10cm to 105cm (the distance was measured by a ruler). At each position, 20 measurements were carried out. Using the measured delay times, the calibrated sound velocity and using Equation 4.17 and Equation 4.18, the sound source coordinates, were calculated and compared with the values which were pre-measured by a ruler (Figure 4.43).

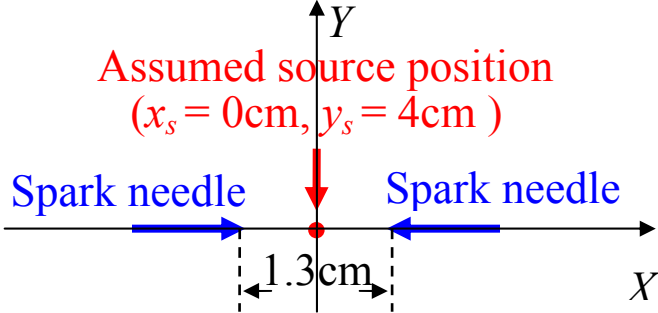
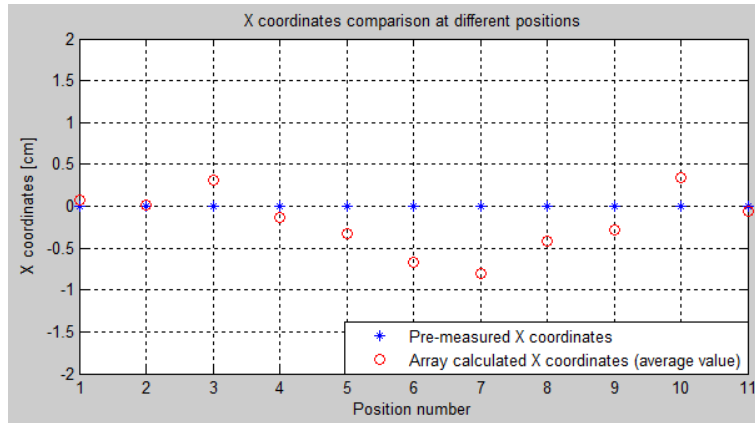
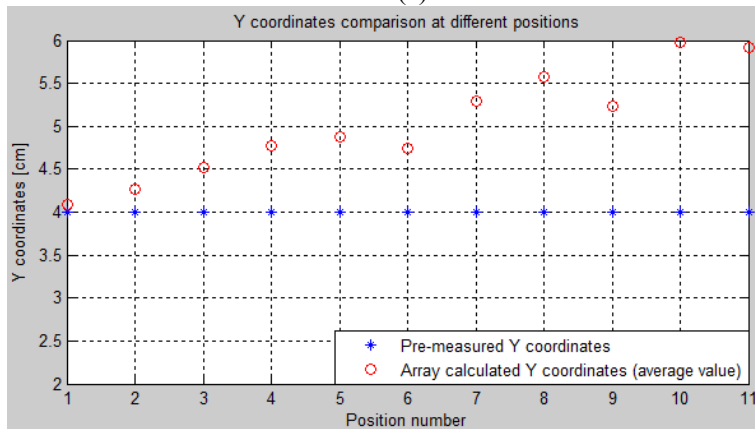


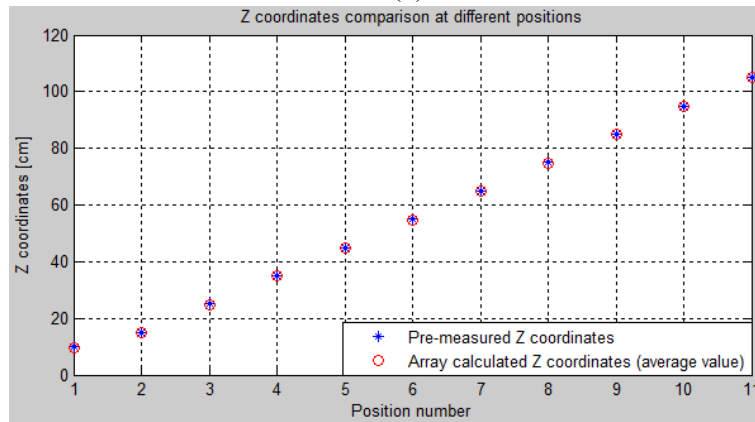
Figure 4.42: Sound source position definition.



(a)



(b)



(c)

Figure 4.43: Coordinates comparisons between the pre-measured values and the calculated values, (a):  $X$  coordinates; (b)  $Y$  coordinates and (c)  $Z$  coordinates.

Figure 4.43 shows that the pre-measured values and the calculated values of the  $Z$  coordinates matched very well, while the  $X$  and  $Y$  coordinates did not. For the  $X$  coordinates (Figure 4.43(a)), the calculated values fluctuated around the pre-measured values. This phenomenon could be explained by the fact that the real spark generation point was not always at the middle of the two needles; the point varied during the experiment and was different from position to position. To verify this assumption, a high speed camera is needed to capture the



spark images during the whole measurement process for position analysis, which is not applicable at the current stage.

For the  $Y$  coordinates (Figure 4.43(b)), the differences between the pre-measured values and the calculated values linearly increased up to 2cm when the measurement position changed from 1 to 11 (from Figure 4.43(c), this position changing means the  $Z$  coordinates changed from 10cm to 105cm). There are three possible reasons that may explain this phenomenon. One reason is that the table surface, onto which the measurement setup was placed, was not level; the second reason is that the ground surface was not level; and the third is the combination of the previous two effects. Table 4.2 presents the measured distance between the table surface and ground surface at corresponding measurement positions. These results eliminate the possibility that the table surface was unlevel. So, the differences between the pre-measured values and the calculated values of the  $Y$  coordinates can be explained by the ground surface being unlevel, as shown in Figure 4.44. The angle  $\theta$  between the ground surface and the level is calculated to be  $1.1^\circ$ .

Position number	source	1	2	3	4	5	6	7	8	9	10	11
Distance between source and measurement position in $Z$ coordinates [cm]	0	10	15	25	35	45	55	65	75	85	95	105
Distance between table surface and ground surface [cm]	87	86.8	86.8	86.7	86.7	86.7	86.7	86.7	86.7	86.5	86.6	86.5

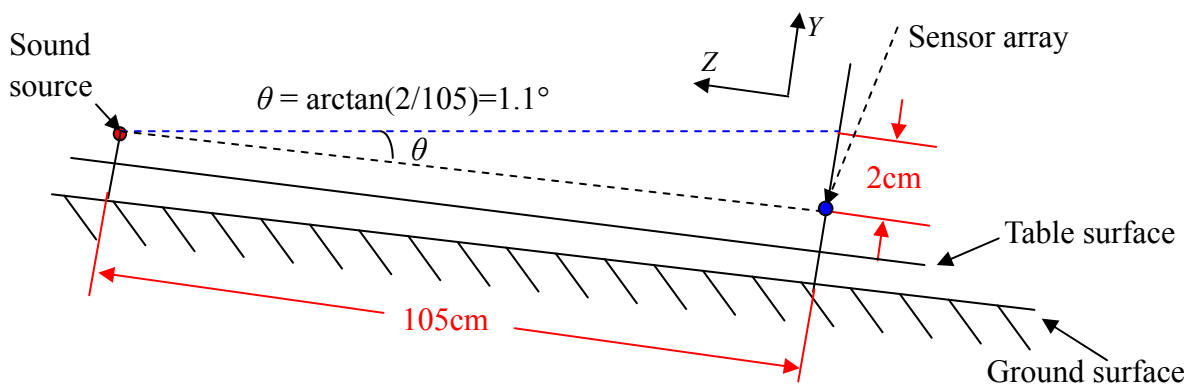


Figure 4.44:  $Y$  coordinates differences between the pre-measured values and the calculated values due to unlevel ground surface.

## 4.5 Summary

In this chapter, two microphone samples fabricated using surface micromachining technique and bulk micromachining technique were tested. From the contact resistance measurement, the usefulness of the titanium silicide layer is verified. Using this interlayer between Cr/Au metallization system and heavily doped MILC poly-Si material, the contact resistance decreased to almost the same level as in the traditional AlSi to poly-Si contact system, which is widely used in the CMOS process. Then, the static sensitivity was measured by the nano-indentation technique, which demonstrated that the static sensitivity value is similar for both samples. Finally, these two samples were dynamically calibrated using a spark generated N-wave source. Due to the previously mentioned acoustic short path effect, the surface micromachined sample not only lost low frequency information, but also had ten times lower dynamic sensitivity compared to the bulk micromachined sample. Finally, the array application of the sensors as a sound source localizer was demonstrated using the bulk micromachined devices.

## 4.6 References

- [1] R. J. Bobber, "ch. 2," in *Underwater Electroacoustic Measurement*, US Government Printing Office, 1970.
- [2] W. Schottky, "Das Gesetz des Tiefempfangs in der Akustik und Elektroakustik," *Zeitschrift fur Physik A Hadrons and Nuclei*, vol. 36, pp. 689-736, 1926.
- [3] S. Ballantine, "Reciprocity in Electromagnetic, Mechanical, Acoustical, and Interconnected Systems," *Proceedings of the Institute of Radio Engineers*, vol. 17, pp. 927-951, 1929.
- [4] W. R. MacLean, "Absolute Measurement of Sound Without a Primary Standard," *The Journal of the Acoustical Society of America*, vol. 12, pp. 140-146, July 1940.
- [5] R. K. Cook, "Absolute Pressure Calibration of Microphones," *The Journal of the Acoustical Society of America*, vol. 12, pp. 415-420, January 1941.
- [6] E. Frederiksen and J. I. Christensen, "Pressure Reciprocity Calibration - Instrumentation, Results and Uncertainty," *Bruel & Kjaer Technical Review*, vol. No.1, 1998.
- [7] A. J. Zuckerwar, G. C. Herring, and B. R. Elbing, "Calibration of the pressure sensitivity of microphones by a free-field method at frequencies up to 80 kHz," *The Journal of the Acoustical Society of America*, vol. 119, pp. 320-329, January 2006.
- [8] N. N. Hsu and L. Ky, "Acoustic Emissions Simulator," 4018084, 1977.
- [9] *Standard method for primary calibration of acoustic emission sensors*, Annual book of ASTM standards, Vol. 03.03, ASTM Philadelphia, pp. 486 - 495, 1994.
- [10] M. Averiyarov, "Nonlinear-diffraction effects in propagation of sound waves through turbulent atmosphere: experimental and theoretical studies," Ph.D Thesis, l'École Centrale de Lyon, 2008.
- [11] W. Snow, "Survey of acoustic characteristics of bullet shock waves," *Audio and Electroacoustics, IEEE Transactions on*, vol. 15, pp. 161-176, 1967.
- [12] D. T. Deihl and J. F. R. Carlson, "'N Waves" from Bursting Balloons," *American Journal of Physics*, vol. 36, pp. 441-444, May 1968.
- [13] N. R. McKenzie, "The effect of viscous attenuation on shock tube performance," M.S. Thesis Report, , Air Force Inst. of Tech., Wright-Patterson AFB, OH., 1994.

- [14] C. E. Bell and J. A. Landt, "Laser-induced high-pressure shock waves in water," *Applied Physics Letters*, vol. 10, pp. 46-48, 1967.
- [15] J. F. Roach, W. Zagieboylo, and J. M. Davies, "Shock wave generation in dielectric liquids using Q-switched lasers," *Proceedings of the IEEE*, vol. 57, pp. 1693-1694, 1969.
- [16] J. P. Chen, R. X. Li, Z. N. Zeng, X. T. Wang, and Z. Z. Xu, "Experimental observation of a ps-laser-induced shock wave," in *Lasers and Electro-Optics. CLEO/Pacific Rim 2003. The 5th Pacific Rim Conference on*, p. 544 vol.2, 2003.
- [17] W. M. Wright, "Propagation in air of N waves produced by sparks," *The Journal of the Acoustical Society of America*, vol. 73, pp. 1948-1955, June 1983.
- [18] R. Wyber, "The design of a spark discharge acoustic impulse generator," *Acoustics, Speech and Signal Processing, IEEE Transactions on*, vol. 23, pp. 157-162, 1975.
- [19] E. Martinson and J. Delsing, "Electric spark discharge as an ultrasonic generator in flow measurement situations," *Special Issue: Validation and Data Fusion for Process Tomographic Flow Measurements*, vol. 21, pp. 394-401, 2010.
- [20] R. E. Klinkowstein, "A study of acoustic radiation from an electrical spark discharge in air," M.S., Thesis, Department Mechanical Engineering, Massachusetts Institute of Technology, 1974.
- [21] M. N. Plooster, "Shock Waves from Line Sources. Numerical Solutions and Experimental Measurements," *Physics of Fluids*, vol. 13, pp. 2665-2675, November 1970.
- [22] P. Yuldashev, M. Averiyarov, V. Khokhlova, O. Sapozhnikov, S. Ollivier, and P. Blanc Benon, "Measurement of shock N-waves using optical methods," in *10eme Congres Francais d'Acoustique*, Lyon, France, 2010.
- [23] S. Ollivier, E. Salze, M. Averiyarov, P. V. Yuldashev, V. Khokhlova, and P. Blanc-Benon, "Calibration method for high frequency microphones," in *Acoustics 2012 conference*.

## Chapter 5: Summary and Future Work

### 5.1 Summary

In this thesis, at the beginning, the definition and the performance specifications of the wide-band aero-acoustic microphone were introduced. This kind of microphone is specifically used in the acoustic scaled modeling technique with a scaling factor  $M$  larger than 20, which requires the microphone to have a bandwidth of several hundreds of kilo-Hz and a dynamic range of up to 4kPa. Then, a comparative study of the current state-of-the-art of capacitive and piezoresistive microphones, especially the study of their scaling properties, demonstrated that a piezoresistive sensing mechanism is more suitable for achieving the wide-band and large sensitivity requirements.

In Chapter Two, first, the key mechanical properties including residual stress, density and Young's modulus, of LS-SiN, which was used to build the sensing diaphragm were discussed and measured. Following this, the design considerations due to the use of different micro-fabrication techniques (surface micromachining technique and bulk micromachining technique) were discussed, and two different mechanical structures were proposed and modeled by the FEA method at the end of the chapter.

Because the piezoresistive material is the same for both micromachining techniques, at the beginning of Chapter Three, a review of the material fabrication technique (MILC) was presented. Then, detailed fabrication processes of the surface micromachining and bulk micromachining techniques were illustrated with transitional schematic views of the microphone cross-sectional areas.

In Chapter Four, firstly, the electrical performances of the piezoresistor, such as sheet resistance and contact resistance, were measured. Then, the static point-load response was measured using the nano-indentation technique. Following this, the microphone dynamic

calibration methods, including the reciprocity method, substitution method and pulse calibration method, were reviewed. Due to the characteristics of the piezoresistive sensing mechanism and commercial reference microphone market limitations, both the reciprocity and substitution methods are not suitable for calibrating these newly designed wide-band high frequency microphones. Only pulse calibration, which requires a repeatable, high acoustic amplitude and short duration acoustic pulse source, is suitable for our calibration process. Then, the acoustic pulse source, an electrical discharge induced spark generator, was presented and the characterization and reconstruction method of the generated N-wave were introduced. Finally, the dynamic calibrated microphone frequency responses were shown and compared.

Comparisons between other already demonstrated piezoresistive type aero-acoustic microphones and the current work are listed in Table 5.1. While keeping a small diaphragm size, the microphone in the current work achieves the highest measurable pressure level, at least up to 165dB, and has the widest calibrated bandwidth, from 6kHz to 500kHz. This microphone has a lower sensitivity. The main reason is that the sensing material used in the current work is MILC poly-Si material, which has a lower gauge factor compared to the sc-Si material used in Arnold and Sheplak's work. Another reason is that the piezoresistor geometry shape in the current work is not optimized, especially the piezoresistor thickness. To make the resistance of the piezoresistor smaller, which means the electrical-thermal noise is smaller (Equation 5.1), the piezoresistor thickness is kept relatively large. This makes the maximum diaphragm bending stress be not at the diaphragm surface, where the piezoresistor is located.

$$S_{th} = 4K_B RT \quad [V^2 / Hz] \quad (5.1)$$

( $K_B$  is the Boltzmann constant,  $R$  is the resistance, and  $T$  is the temperature in Kelvin)

Table 5.1: Comparisons of current work and state-of-the-art.

Microphone	Type	Radius (mm)	Max pressure (dB)	Sensitivity	Bandwidth (predicted)
Arnold et al. [1]	piezoresistive	0.5	160	0.6 $\mu$ V/V/Pa(3V)	10Hz ~ 19kHz (~100kHz)
Sheplak et al. [2]	piezoresistive	0.105	155	2.2 $\mu$ V/V/Pa(10V)	200Hz ~ 6kHz (~300kHz)
Current work	piezoresistive	0.105 (square)	165	0.28 mV/V/Pa (3V)	6kHz (DC) ~500kHz

## 5.2 Future Work

Although two wide-band high frequency microphone prototypes were successfully fabricated and calibrated, there are several issues that need to be worked on in the near future. Firstly, models of these two microphones are all based on the FEA method. This method is useful and accurate for structure performance verification, but the limitation is that it is not suitable to use for design, which means that, given specifications, a designer needs to conduct many trials to find the structure's shape and dimensions. Therefore an analytical model, which may not be accurate but could quickly estimate the performance of different structures, is urgently needed.

Secondly, for the microphone fabricated using the bulk micromachining technique, due to the large cavity under the sensing diaphragm, there is no sufficient damping to critically damp the resonant peak. In the future, a new structure with an integrated damper using the squeeze film damping effect should be explored. At the same time, as the titanium silicidation technique is not needed for reducing contact resistance, the thickness of the piezoresistor could be decreased to increase the sensitivity. The trade-off between increasing sensitivity and increasing noise level due to the decreasing of the piezoresistor's thickness should be optimized.

Thirdly, in our testing, the amplifier is built by discrete components on the PCB and the sensor and amplifier are connected through wire bonding. To depress the noise and increase the amplification performance, the amplifier should be fabricated on one chip, and eventually the sensor and amplifier should be fabricated on one die together.



### 5.3 References

- [1] D. P. Arnold, S. Gururaj, S. Bhardwaj, T. Nishida, and M. Sheplak, "A piezoresistive microphone for aeroacoustic measurements," in *Proceedings of ASME IMECE 2001, International Mechanical Engineering Congress and Exposition*, pp. 281-288, 2001.
- [2] M. Sheplak, K. S. Breuer, and Schmidt, "A wafer-bonded, silicon-nitride membrane microphone with dielectrically-isolated, single-crystal silicon piezoresistors," in *Technical Digest. Solid-State Sensor and Actuator Workshop . Transducer Res*, Cleveland, OH, USA, pp. 23-26, 1998.

## **Appendix I: Co-supervised Ph.D Program Arrangement**

My Ph.D study was co-supervised by Dr. Man WONG, Professor of Electronic and Computer Engineering (ECE) Department at the Hong Kong University of Science and Technology (HKUST) and Dr. Libor RUFER, Researcher at Laboratoire Techniques de l'Informatique et de la Microélectronique pour l'Architecture des systèmes integres (TIMA Lab.), France. Dr. RUFER is also affiliated with Centre national de la recherche scientifique (CNRS, France), Université Joseph Fourier (UJF) and Grenoble Institute of Technology (Grenoble-INP). In June 2009, UJF, Grenoble-INP and other research institutes merged into Université de Grenoble (UG), so I registered both in the HKUST and UG from 2009 to 2013.

My research work was financially supported by the French Consulate at Hong Kong and also funded by Agence Nationale de la Recherche (ANR, French National Agency for Research) through Program BLANC 2010 SIMI 9 for the project SIMMIC. The consortium for this project consisted of three academic laboratories: TIMA, LIRMM (Laboratoire d'Informatique, de Robotique et de Microélectronique de Montpellier, l'Université Montpellier 2) and LMFA (Laboratoire de Mécanique des Fluides et d'Acoustique, Ecole Centrale de Lyon) and one private partner (Microsonics).

For my Ph.D study, generally speaking, when I was in Hong Kong, research works were estimating the mechanical vibration of the sensing diaphragm using lumped-element model and FEA method, developing the corresponding sensor fabrication process and preliminary static response measurement. I spent one year in Grenoble, from February 2011 to July 2011 and February 2012 to July 2012. When I was in Grenoble, research works were sensor dynamic calibration with the cooperation of LMFA and sensor mechanical-acoustic interaction modeling with the cooperation of Microsonics.

## Appendix II: Extended Résumé

Pour les raisons de clarté et de facilité de compréhension, dans cette thèse, le capteur MEMS à haute fréquence sera également dénommé le microphone MEMS aéro-acoustique à large bande. L'aéro-acoustique est une filière de l'acoustique qui étudie la génération de bruit soit par un mouvement turbulent du fluide, soit par les forces aérodynamiques qui interagissent avec les surfaces. L'aéro-acoustique est un secteur en croissance qui attire une attention contemporaine en raison de l'évolution de la transportation aérienne, terrestre et spatiale.

Conformément à la définition ci-dessus, notre recherche se concentre principalement sur trois domaines aéro-acoustiques. Tout d'abord, des avancées significatives en aéro-acoustique sont nécessaires pour réduire le bruit environnemental et le bruit de cabine générés par les avions subsoniques, et pour se préparer à l'éventuelle entrée à grande échelle des avions supersoniques dans l'aviation civile. D'autre part, dans le domaine des transports terrestres, les efforts sont faits pour réduire le bruit aérodynamique des automobiles et des trains à grande vitesse. Enfin, si le bruit des véhicules lancés dans l'espace n'est pas contrôlé, de graves dommages structurels peuvent être engendrés au véhicule et à sa charge.

Alors que les tests/mesures d'un objet dans une situation réelle sont possibles, leur dépense est trop élevée, leur configuration est généralement compliquée et les résultats sont facilement corrompus par le bruit ambiant et par les changements de paramètres environnementaux, tels que les fluctuations de la température et de l'humidité. Par conséquent, les tests effectués en laboratoire dans une condition bien contrôlée en utilisant les modèles de dimension réduite sont préférables.

La plupart des travaux anciens sur les microphones MEMS ont porté sur la conception des microphones acoustiques low-cost pour leurs applications dans la téléphonie mobile. En revanche, l'objectif de cette thèse est clairement axé sur les applications métrologiques en acoustique dans l'air et plus particulièrement sur les applications acoustiques du modèle réduit où les mesures précises des ondes de pression à large bande avec une fréquence de

plusieurs centaines de kHz et les niveaux de pression allant jusqu'à 4kPa sont essentielles.

Afin de couvrir une large gamme de fréquences, les transducteurs électro-acoustiques pour la génération et la détection de signal acoustique dans l'air utilisent traditionnellement les éléments piézoélectriques. Les transducteurs piézoélectriques classiques en volume vibrant en mode d'épaisseur ou de flexion ont été largement utilisés pour les détecteurs de présence. L'un des inconvénients de ces systèmes est la nécessité d'utiliser les couches d'adaptation sur la surface active du transducteur, ce qui minimise la différence principale entre l'impédance acoustique du transducteur et le milieu de propagation. L'efficacité de ces couches dépend de la fréquence et du process. Bien que ces capteurs puissent fonctionner dans la gamme de plusieurs centaines de kHz, ils souffrent d'une bande de fréquence étroite et d'une sensibilité relativement faible, ce qui entraîne la faible dynamique du signal.

D'autres transducteurs électro-acoustiques les plus couramment utilisés sont les microphones de type capacitif et de type piézorésistif. Dans le microphone de type capacitif, la membrane fonctionne comme une plaque d'un condensateur, et les vibrations entraînent la variation de la distance entre les plaques. Avec une polarisation DC, les plaques stockent une charge fixe. Sous l'effet de cette charge fixe, les surfaces des plaques et le diélectrique au milieu, la tension maintenue à travers les plaques de condensateur varie avec la fluctuation de séparation engendrée par la vibration de l'air.

Le microphone de type piézorésistif est constitué d'un diaphragme équipé de quatre résistances piézorésistives configurées en pont de Wheatstone. Les piézorésistances fonctionnent sur la base de l'effet piézorésistif, qui décrit la variation de la résistance électrique du matériau à cause d'une contrainte mécanique appliquée. Pour les diaphragmes minces et les petites déformations, la variation de la résistance est linéaire en fonction de la pression appliquée.

Le Tableau 1 résume les propriétés de dimensionnement des microphones MEMS de type capacitif et piézorésistif, dans lequel le SBW est défini par le produit de la sensibilité et de la bande passante du microphone. Nous constatons dans le Tableau 1 que, en supposant que le

ratio d'aspect du diaphragme reste inchangé, si les dimensions du microphone sont réduites, la performance globale du microphone piézorésistif va améliorer, tandis que celle du microphone capacitif détériore. En conséquence, le mécanisme de détection par piézorésistivité est finalement choisi pour réaliser le microphone aéro-acoustique.

Tableau 1: Propriétés de dimensionnement des microphones MEMS.				
Microphone type	Sensibilité	Bande passante	SBW	Tendance
Piezorésistif	$V_B \cdot \frac{a^2}{h^2}$	$\frac{h}{a^2}$	$\frac{V_B}{h}$	S -, BW ↑, SBW ↑
Capacitif	$\frac{V_B \cdot A}{g} \cdot \frac{a^2}{h \cdot h^2}$	$\frac{h}{a^2}$	$\frac{V_B}{g} \cdot \frac{a^2}{h^2}$	S ↓, BW ↑, SBW ↓

Le silicium monocristallin a été principalement utilisé pour fabriquer les microphones aéro-acoustiques piézorésistifs grâce à son facteur de jauge très élevé. Les techniques de bonding sont utilisées, y compris la technique de bonding par fusion à haute température et la technique de bonding direct à basse température assisté par plasma.

Bien que le silicium monocristallin possède un facteur de jauge élevé, le processus de bonding complique le flux de process et cette technique de bonding n'offre pas un rendement élevé. Dans les chapitres suivants de cette thèse, le matériau de silicium polycristallin re-cristallisé sera utilisé pour remplacer le silicium monocristallin pour réaliser les piézorésistances.

L'élément clé de la structure de microphone est le film mince, qui peut se déformer lorsque la pression est appliquée. Après le processus de dépôt de film mince, ce film contient normalement une contrainte résiduelle, qui est le plus souvent provoquée soit par la différence de coefficient de dilatation thermique entre la couche mince et le substrat ou par les différences de propriété de matériaux dans l'interface entre le film mince et le substrat, tel que le désaccord de maille. La première d'entre eux est appelée la contrainte thermique et cette dernière est appelée la contrainte intrinsèque.

En 1909, Stoney a constaté que, après le dépôt d'un film mince métallique sur le substrat, la structure film-substrat avait plié en raison de la contrainte résiduelle dans le film déposé (Figure 1). Puis il a donné la formule bien connue comme l'Equation 1 pour calculer la contrainte dans le film mince basé sur la mesure de la courbure de flexion du substrat, où  $\sigma$  est la contrainte résiduelle du film mince,  $E_s$  est le module d'Young du matériau du substrat,  $d_s$  est l'épaisseur du substrat,  $d_f$  représente l'épaisseur du film mince,  $\nu_s$  est le coefficient de Poisson du matériau du substrat et  $R$  est la courbure de flexion.

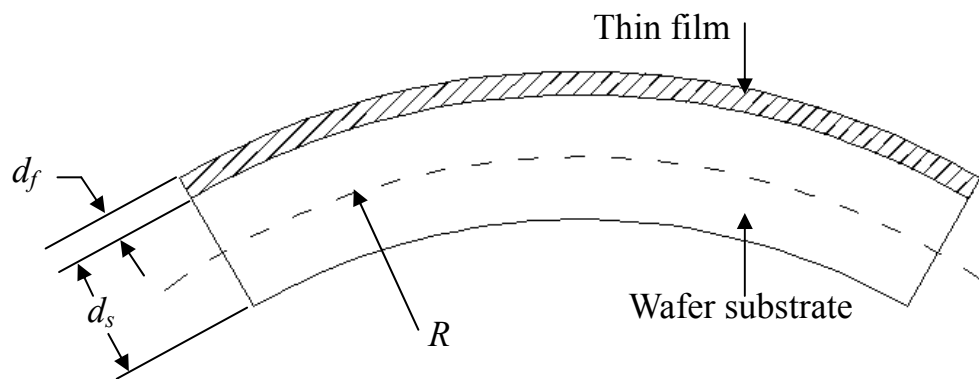


Figure 1: Flexion de la structure film-substrat en raison de la contrainte résiduelle.

$$\sigma = \frac{E_s d_s^2}{6R(1-\nu_s)d_f} \quad (1)$$

Le Tableau 2 présente les valeurs numériques utilisées dans l'Equation 1 pour le calcul et la contrainte résiduelle calculée.

Tableau 2: Les paramètres pour la mesure par méthode de courbure et le résultat.					
$E_s$ (GPa)	$\nu_s$	$d_s$ ( $\mu\text{m}$ )	$d_f$ ( $\mu\text{m}$ )	$R$ (m)	$\sigma$ (MPa)
185	0,28	525	0,5	143,1	165
185	0,28	525	1	55,2	214

La formule de Stoney est basée sur l'hypothèse que  $d_f \ll d_s$ , et le résultat calculé est une valeur moyenne de la contrainte à l'intérieur du wafer entier. La méthode de poutre en rotation est une autre technique couramment utilisée pour mesurer la contrainte résiduelle dans le film

mince, et l'avantage de cette méthode est que la contrainte peut être mesurée localement.

Les détails de la structure de poutre en rotation sont présentés dans la Figure 2. Avec les paramètres de conception énumérés dans le Tableau 3, l'équation de calcul de la contrainte résiduelle est

$$\sigma = \frac{E\delta}{6490} (MPa), \quad (2)$$

où  $E$  est le module d'Young du matériau de la poutre et  $\delta$  est la distance traversée de la poutre en rotation sous la contrainte. Le défaut principal de cette méthode est que, sauf si nous savons exactement le module d'Young du matériau de la poutre, la valeur de la contrainte résiduelle calculée n'est pas exacte. Les traversées de rotation sont  $5,5\mu\text{m}$  et  $4\mu\text{m}$  et les contraintes résiduelles correspondantes sont  $175\text{MPa}$  et  $128\text{MPa}$  pour le matériau LS-SiN ayant une épaisseur de  $1\mu\text{m}$  et  $0,5\mu\text{m}$ , respectivement. Les valeurs de contrainte résiduelle mesurées par la méthode de poutre en rotation est d'environ 20% de moins que les valeurs mesurées par la méthode de courbure.

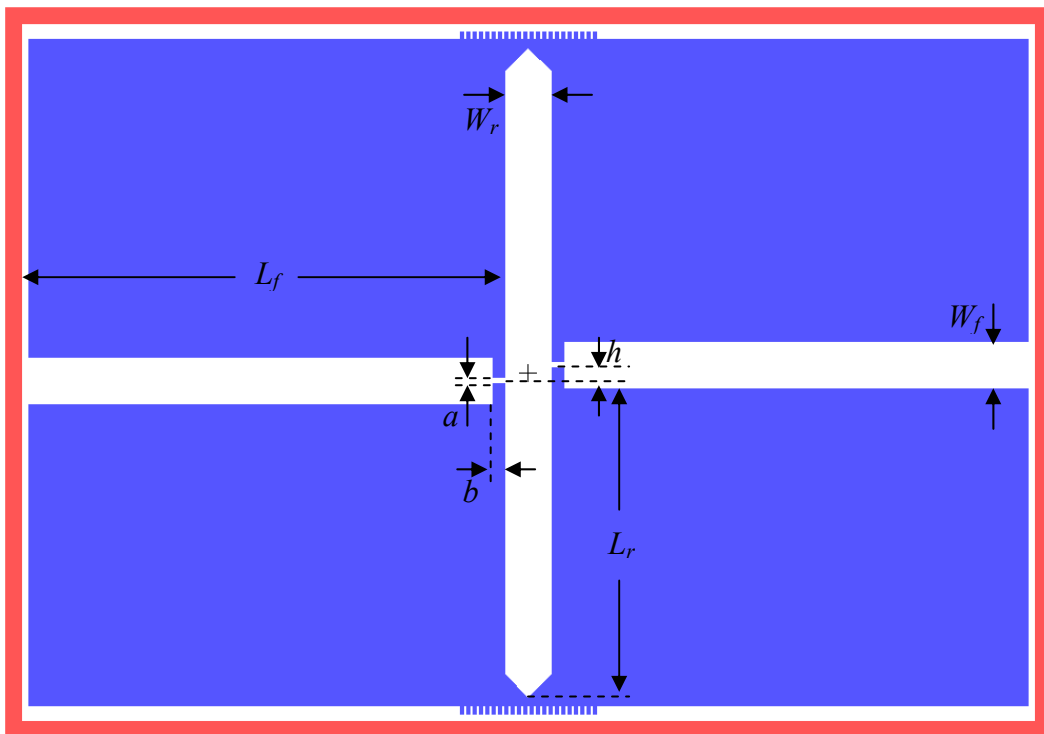


Figure 2: Layout de la structure de poutre en rotation.

Tableau 3: Paramètres dimensionnelles de la poutre en rotation.			
$W_r$ ( $\mu\text{m}$ ):	30	$W_f$ ( $\mu\text{m}$ ):	30
$L_f$ ( $\mu\text{m}$ ):	300	$L_r$ ( $\mu\text{m}$ ):	200
$a$ ( $\mu\text{m}$ ):	4	$b$ ( $\mu\text{m}$ ):	7,5
$h$ ( $\mu\text{m}$ ):	10		

La densité du matériau du diaphragme et le module d'Young sont également importants pour l'estimation de la performance des vibrations mécaniques. La densité détermine la masse totale du diaphragme et le module d'Young détermine la constante de raideur du ressort. Toutes ces deux valeurs sont les résultats des calculs indirects de la fréquence du premier mode de résonance des structures de poutre encastree-encastree avec des longueurs différentes.

L'Équation 3 est utilisée pour calculer la fréquence du premier mode de résonance d'une structure de poutre encastree-encastree basé sur la méthode de Rayleigh-Ritz, où  $\omega$  est la fréquence de résonance en rad / s,  $t$  et  $L$  sont respectivement l'épaisseur et la longueur de la poutre, et  $E$ ,  $\rho$  et  $\sigma$  sont respectivement le module d'Young, la densité et la contrainte résiduelle du matériau de la poutre. Comme nous connaissons déjà la contrainte résiduelle en utilisant les méthodes décrites dans le paragraphe précédent, en mesurant les fréquences du premier mode de résonance  $\omega_1$  et  $\omega_2$  des poutres encastrees-encastrees avec la même section transversale mais de différentes longueurs  $L_1$  et  $L_2$ , le module d'Young et la densité du matériau de la poutre peuvent être calculés par les Equations 4 et 5.

$$\omega^2 = \frac{4\pi^4 t^2 E}{9L^4 \rho} + \frac{2\pi^2 \sigma}{3L^2 \rho} \quad (3)$$

$$E = \frac{3\sigma \left( \frac{1}{L_2^2} - \frac{1}{L_1^2} \frac{\omega_2^2}{\omega_1^2} \right)}{2t^2 \left( \frac{1}{L_1^4} \frac{\omega_2^2}{\omega_1^2} - \frac{1}{L_2^4} \right)} \quad (4)$$

$$\rho = \frac{2\sigma\pi^2}{3} \frac{L_2^2 - L_1^2}{L_2^4 \omega_2^2 - L_1^4 \omega_1^2} \quad (5)$$



La fréquence de résonance de la poutre encastree-encastree est mesurée par un vibromètre laser Fogale. Le die d'échantillon est collé sur une plaquette piézoélectrique avec silicone (RHODORSIL™), et la plaquette piézoélectrique est collée sur une petite carte PCB avec la colle conductrice d'argent. Cet échantillon préparé est fixé sur un étage sous vide sans vibrations. Pendant la mesure, un signal sinusoïdal est fourni à la plaquette piézoélectrique et la fréquence d'entrée est balayée dans une large bande passante à partir de 10kHz jusqu'à 2 MHz. Le point laser du vibromètre est centré au centre de la poutre et l'amplitude du déplacement de la vibration correspondante est enregistrée. La densité moyenne calculée et le module d'Young du matériau LS-SiN déposé sont respectivement  $3002\text{kg/m}^3$  et  $207\text{GPa}$ .

Pour concevoir un microphone large-bande à la haute fréquence, non seulement les spécifications de performance du composant et les propriétés de matériau doivent être pris en compte, mais aussi la faisabilité du process de fabrication du composant. La conception de la structure physique doit également accompagner la conception du process de fabrication.

Les techniques de micro-usinage de surface et de volume ont leurs différentes capacités et contraintes pour la conception du microphone. En utilisant la technique de micro-usinage de surface, les aspects réalisables sont les suivants: (1) La dimension du diaphragme de détection suspendu peut être indépendante de l'épaisseur de la chambre d'air au-dessous. (2) La structure concave de pyramide inversée est introduite dans le diaphragme de détection pour éviter le problème commun de blocage par adhérence dans le process de fabrication par micro-usinage de surface. Les limites de cette technique sont les suivantes: (1) Les trous / fentes de relaxation seront ouverts sur le diaphragme de détection, ce qui conduit à un court-circuit acoustique entre l'espace ambiant et la cavité en dessous du diaphragme. En raison de ce court-circuit acoustique, la différence de pression est égalisée à basse fréquence, ce qui limite la performance du microphone. (2) A cause de l'attaque éventuelle du métal de la face supérieure par les solutions de gravure, la compatibilité du process doit être prise en compte.

En utilisant la technique de micro-usinage de volume, les avantages sont les suivants: (1) Il

s'agit d'un process relativement simple, et il y a moins de soucis de compatibilité entre la métallisation en face supérieure et les produits chimiques de relaxation. (2) Il y a un diaphragme complet sans trous/fentes, ce qui élimine l'effet de court-circuit acoustique, la propriété à basse fréquence du microphone sera ainsi améliorée. Les contraintes de cette technique sont les suivantes: (1) A cause des caractéristiques de la gravure par côté inférieur, la cavité d'air sous le diaphragme de détection sera très large. Cela signifie que le diaphragme de détection ne sera pas amorti. Un pic de résonance élevé existera dans le spectre fréquentiel de la réponse du microphone. (2) Quel que soit le type de technique de micro-usinage de volume utilisé, la longueur de gravure latérale sera proportionnelle au temps de gravure verticale. Cela signifie que la non-uniformité de l'épaisseur du substrat conduira à une variation de dimension du diaphragme.

Un diaphragme carré entièrement encastré est réalisé par la technique de micro-usinage de volume. Pour modéliser ses caractéristiques vibratoires, la méthode d'éléments finis (FEA) est la plus appropriée. Pour un diaphragme carré avec une longueur de 210µm, à l'aide des paramètres de modélisation énumérés dans le Tableau 4, la masse ponctuelle de vibration est simulée à  $3,95 \times 10^{-11}$  kg et la fréquence du premier mode de résonance est d'environ 840kHz.

Tableau 4: Paramètres de modélisation du diaphragme carré.			
Longueur du diaphragme (µm)	210	Epaisseur du diaphragme (µm)	0,5
Densité du diaphragme (SiN) (kg/m <sup>3</sup> )	3002	Module d'Young du diaphragme (SiN) (GPa)	207
Coefficient de Poisson	0,27	Contrainte résiduelle (MPa)	165

En utilisant l'équation suivante

$$f_r = \frac{1}{2\pi} \sqrt{\frac{k}{m}}, \quad (6)$$

où  $f_r$  est la fréquence de résonance,  $k$  est la constante effective de ressort du diaphragme et  $m$  est la masse effective du diaphragme, le  $k$  est calculé d'être 1100N/m. La réponse fréquentielle mécanique du diaphragme peut être modélisée par un simple système de

ressort-masse avec un seul degré de liberté. Ensuite, en utilisant l'analogie électro-mécanique, la réponse fréquentielle mécanique du capteur peut être analysée en utilisant la théorie traditionnelle du circuit électrique.

Compte tenu de la technique de micro-usinage de surface, en raison de la fente requise pour la gravure de relaxation, la structure d'un diaphragme carré avec quatre poutres de support est utilisée, et la fente de gravure entoure les poutres de support et le diaphragme (Figure 3). Comme décrit dans la section précédente, en raison de l'effet de court-circuit acoustique introduit par la fente de relaxation, il est difficile de modéliser analytiquement la réponse couplée acoustique-mécanique. Dans cette situation, seule la méthode par éléments finis est applicable à la modélisation de cet effet compliqué. Sous ANSYS, l'élément 3-D acoustique de la fluide FLUID30 est utilisé pour modéliser le milieu fluide, l'air dans notre cas, et l'interface dans les problèmes d'interaction fluide-structure. L'élément infini 3-D acoustique de la fluide FLUID130 est utilisé pour simuler les effets d'absorption d'un domaine de fluide qui s'étend à l'infini au-delà de la limite du domaine constitué des éléments FLUID30. Le 20-noeud élément structurel solide SOLID186 est utilisé pour modéliser la déformation mécanique de la structure et les propriétés de la vibration.

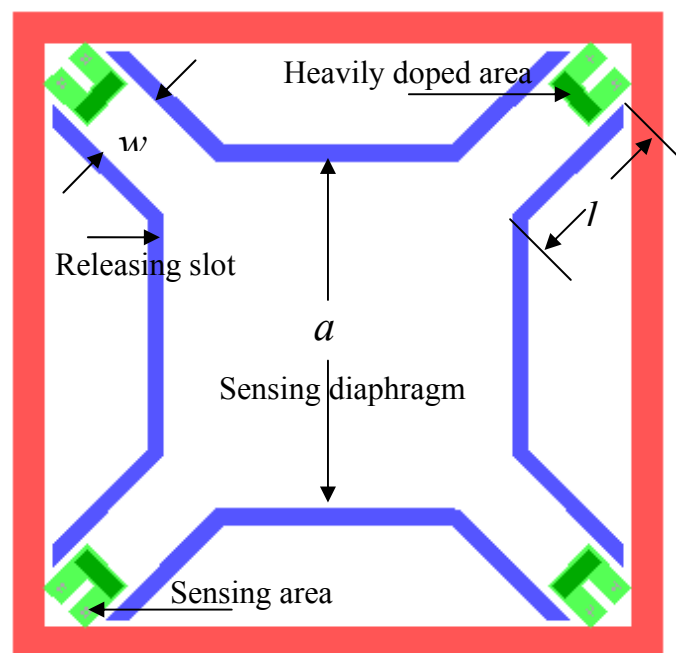


Figure 3: Layout du diaphragme avec les poutres de support (les résistances de référence ne sont pas indiquées).

Les paramètres de modélisation sont énumérés dans le Tableau 5. L'analyse harmonique est appliquée sur le modèle en balayant la fréquence de 10Hz à 1MHz. La simulation de la réponse fréquentielle mécanique montre que la fréquence du premier mode de résonance est 400kHz.

Longueur du diaphragme ( $\mu\text{m}$ )	115	Epaisseur du diaphragme ( $\mu\text{m}$ )	0,5
Longueur du diaphragme de support ( $\mu\text{m}$ )	55	Largeur du diaphragme de support ( $\mu\text{m}$ )	25
Profondeur de la cavité d'air ( $\mu\text{m}$ )	9	Rayon de la plaque d'absorption acoustique ( $\mu\text{m}$ )	345
Longueur de la fente de relaxation ( $\mu\text{m}$ )	700	Largeur de la fente de relaxation ( $\mu\text{m}$ )	5
Densité du diaphragme (SiN) ( $\text{kg}/\text{m}^3$ )	3002	Module d'Young du diaphragme (SiN) (GPa)	207
Coefficient de Poisson	0,27	Contrainte résiduelle (MPa)	165
Vitesse de son (m/s)	340	Densité d'air ( $\text{kg}/\text{m}^3$ )	1,225

Le silicium monocristallin (sc-Si) est un matériau très mature dans l'industrie des semiconducteurs pour les applications piézorésistives. Toutefois, à cause des limitations du matériau et de la technologie, tels que le désaccord de maille, les différents coefficients de dilatation thermique et le rendement de bonding, il est assez difficile et coûteux d'intégrer le matériau sc-Si sur les substrats exotiques comme le verre pour les applications d'affichage sur le panneau plat, ou de l'intégrer dans les circuits intégrés en 3-D, comme dans un process de fabrication du VLSI.

Au lieu de sc-Si, l'*a*-Si, fabriqué par les techniques de dépôt LPCVD ou PECVD, est utilisé pour fabriquer les circuits de pilotage avec les transistors à couche mince (TFT) pour les écrans à cristaux liquides et les cellules photovoltaïques intégrées sur les substrats en verre ou

en plastique. L'inconvénient principal du matériau *a*-Si est sa faible mobilité à effet de champ. Par conséquent, la technique de dépôt du silicium cristallin sur les matériaux amorphes devient de plus en plus importante pour l'industrie des semiconducteurs, et la taille des grains du silicium déposé est une considération particulièrement pertinente pour le process puisque la taille du grain peut dominer les propriétés électriques des matériaux qui ont une faible taille du grain.

Entre *sc*-Si et *a*-Si, le poly-Si est composé de petits cristaux, appelés cristallites. Il est considéré comme un matériau préféré par rapport à *a*-Si en raison de sa mobilité de porteurs bien plus élevée. Le matériau poly-Si peut être directement déposé dans un four LPCVD, sur une plate-forme de PECVD ou cristallisé à l'issue de l'*a*-Si déposé par les mêmes techniques mentionnées ci-dessus. La qualité des films minces de poly-Si cristallisé a un effet important sur la performance des dispositifs de poly-Si. Au cours des deux dernières décennies, de différentes technologies ont été proposées pour la cristallisation de l'*a*-Si sur les substrats exotiques, y compris la cristallisation en phase solide (SPC), la cristallisation par laser à excimère (ELC) et la cristallisation par l'induction latérale métallique (MILC).

Dans le processus de SPC, le recuit thermique fournit l'énergie nécessaire à la nucléation et l'expansion des grains. En général, la cristallisation intrinsèque en phase solide a besoin d'une longue durée pour cristalliser complètement l'*a*-Si en température élevée, et une grande densité de défaut existe toujours dans le poly-Si cristallisé.

La cristallisation par laser est une autre méthode largement utilisée dans l'actualité pour préparer le poly-Si sur les substrats exotiques. En général, le processus ELC est capable de produire les matériaux de haute qualité, mais elle souffre d'un faible rendement et d'un coût élevé des équipements.

Afin de maintenir à la fois un rendement élevé et une grande taille du grain, le procédé de cristallisation assistée par les catalyseurs a été inventé et peut être divisé en deux grandes catégories: ceux utilisant les catalyseurs semiconducteurs comme le germanium, et ceux utilisant les métaux, tels que Al, Au, Ag, Pd, Co et Ni. Les métaux sont d'abord déposés sur

*a*-Si. Puis *a*-Si est cristallisé en polysilicium à une température inférieure à celle du CPS.

Récemment, le Ni MILC a attiré beaucoup d'attention. Le précipité NiSi<sub>2</sub> joue le rôle d'un noyau de silicium, qui présente une structure cristalline semblable au silicium avec un désaccord de maille de 0,4% avec le silicium. La constante de réseau de NiSi<sub>2</sub>, 5,406Å, est presque égale à celle du silicium, 5,430Å.

Le process complet de micro-usinage de surface commence à partir d'un wafer de silicium de type p (100). La première étape consiste à former les moules concaves des pyramides inverses en surface du substrat. La deuxième étape est de déposer et structurer la couche sacrificielle. Après le dépôt des couches sacrificielles, un masque de «tranchée» est utilisé pour faire la photolithographie pour structurer la zone du diaphragme. Ensuite, *a*-Si est gravé par LAM 490. Enfin, l'oxyde humide est gravé par la solution BOE. Après l'enlèvement de la résine, le LS-SiN de 400nm est déposé par LPCVD, suivi d'une couche de silicium à 600nm. Ensuite, un masque de résistances est utilisé pour la photolithographie et *a*-Si est gravé par un plasma à couplage inductif (ICP) à l'aide du gaz HBr. L'étape suivante est de cristalliser *a*-Si en poly-Si en utilisant la technique MILC. Tout d'abord, un oxyde de basse température (LTO) de 300nm est déposé. Ensuite, un masque pour le "trou de contact" est utilisé pour la photolithographie et le BOE est utilisé pour graver le LTO. Après l'enlèvement de la résine et une plongée dans la solution HF (1:100), une couche de nickel de 5 nm est évaporée sur la surface du wafer. A l'issue d'un recuit dans l'atmosphère d'azote à 590°C pendant 24 heures, le matériau amorphe est induit au type polycristallin. Ensuite, le nickel est enlevé par une solution piranha qui est suivi d'un recuit à haute température à 900°C pendant 0,5 heure. Après la cristallisation de *a*-Si, la solution BOE est utilisée pour décaper la couche LTO et le bore est dopé dans le matériau poly-Si par technique d'implantation ionique. Après cela, les échantillons sont mis dans le four à 1000°C pendant 1,5 heure pour activer le dopant. Par la suite, en déposant la deuxième couche de LS-SiN (100nm), les piézorésistances en poly-Si sont bien protégés. Ensuite, un masque de "trou de contact" et la résine FH 6400L sont utilisés pour faire la photolithographie, et le RIE 8110 est effectué pour graver le nitrure de silicium. Un fort dopage au bore est réalisé ici pour réduire la résistance de contact. À la suite de

l'implantation d'impureté, une activation est effectuée à 900°C pendant 30 minutes. Après avoir utilisé la technique de siliciure de titane pour améliorer la résistance de contact, le masque de "trou de gravure" est utilisé pour faire la photolithographie, et le RIE 8110 est effectué pour graver le nitrure de silicium et ouvrir les trous de gravure de relaxation. Le système de métallisation d'une double-couche de chrome et d'or est déposé par un procédé de lift-off. Après le lift-off, les lignes métalliques sont bien définies. La dernière étape consiste à décaper les deux couches sacrificielles (y compris l'oxyde et l' $\alpha$ -Si) et à libérer le diaphragme. La figure 4 présente un microphone large-bande à haute fréquence fabriqué avec succès en utilisant la technique de micro-usinage de surface.

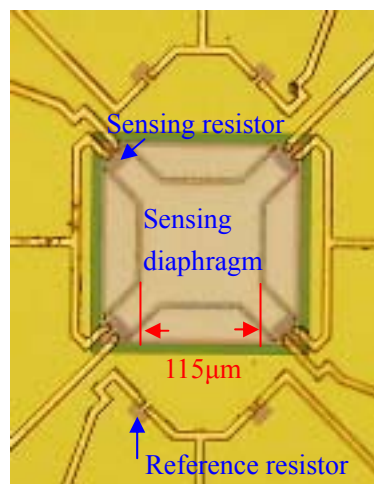


Figure 4: Microphotographie d'un microphone large-bande à haute fréquence fabriqué en utilisant la technique de micro-usinage de surface.

La technique de micro-usinage de volume commence par un wafer poli de type p (100) avec une épaisseur de 300µm. Au début, une couche d'oxyde thermique de 0,5µm, une couche d' $\alpha$ -silicium de 0,1µm et une couche de LS-SiN de 0,4µm en épaisseur sont déposées dans l'ordre. Ensuite, une couche de l' $\alpha$ -Si de 0,56µm en épaisseur est déposée en tant que matériau piézorésistif. Le matériau d' $\alpha$ -silicium en face inférieure est enlevé par une machine de gravure LAM 490 et la face supérieure du silicium est cristallisée en poly-Si en utilisant la technique MILC. Cette couche cristallisée de silicium polycristallin est ensuite structurée pour former la forme des piézorésistances. La piézorésistance est dopée au bore par implantation. Après cela, le wafer est mis dans le four à 1000°C pendant 1,5 heure pour activer le dopant. Après l'activation du dopant, une deuxième couche de LS-SiN de 0,1µm en épaisseur est

déposée, puis une couche de LTO de  $2\mu\text{m}$  d'épaisseur est déposée et le matériau LTO de la face supérieure est enlevé par la solution BOE. Ensuite, le trou de contact est ouvert à l'aide de la résine FH 6400L et la machine à graver à sec RIE 8110. La zone de contact est fortement dopée au bore. À la suite de l'implantation d'impureté, l'activation est effectuée à  $900^\circ\text{C}$  pendant 30 minutes. Après cela, une couche d'Al: Si d'une épaisseur de  $0,5\mu\text{m}$  est pulvérisée et structurée pour former la métallisation. Un recuit dans le gaz d'azote hydrogéné à  $400^\circ\text{C}$  pendant 30 minutes est effectué pour améliorer la résistivité de contact. Ensuite, une résine épaisse de  $3\mu\text{m}$  PR507 est déposée sur la face inférieure du wafer et structurée pour former la zone du diaphragme. Les matériaux déposés en face inférieure comme LTO, LS-SiN,  $\alpha$ -Si et l'oxyde thermique sont enlevés par la technique de gravure sèche. Après cela, le substrat en silicium est gravé à travers par la technique DRIE. Puis l'oxyde et l' $\alpha$ -silicium du côté supérieur sont également éliminés en utilisant la technique de gravure sèche. La figure 5 présente un microphone fabriqué en utilisant la technique de micro-usinage de volume.

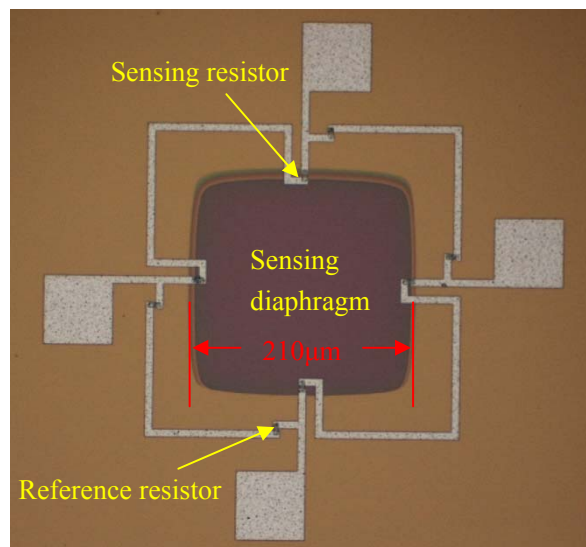


Figure 5: Microphotographie d'un microphone large-bande à haute fréquence fabriqué en utilisant la technique de micro-usinage de volume.

Après la fabrication du dispositif, la résistance carrée du matériau poly-Si MILC dopé est mesurée par une structure en croix grecque. Pour l'échantillon fabriqué par la technique de micro-usinage de surface, les résistances carrées en moyenne mesurées dans la zone de détection et dans la zone de connexion sont respectivement  $411,4 \text{ ohms/carré } (\Omega/\square)$  et  $24,7\Omega/\square$ . Pour l'échantillon fabriqué par la technique de micro-usinage de volume, la



résistance carrée en moyenne mesurée dans la zone de détection est  $446,4\Omega/\square$ . Comme les résistances de détection sont fabriquées en utilisant la même technique MILC avec le même dopage d'impureté et la même condition d'activation pour les deux techniques, leurs résistances carrées sont presque identiques.

La structure de Kelvin est utilisée pour mesurer la résistance de contact  $R_c$  entre le métal et le matériau poly-Si MILC dopé. Pour le système de contact entre Cr/Au et poly-Si MILC, la résistance de contact en moyenne est mesurée à  $46.6\Omega$  et la résistivité spécifique de contact est  $2,91\mu\Omega\cdot\text{cm}^2$  (avec une surface de contact de  $6,25\mu\text{m}^2$ ) et pour le système de contact entre Al: Si et poly-Si MILC, la résistance de contact en moyenne est mesurée à  $58\Omega$  et la résistivité spécifique de contact est  $2,32\mu\Omega\cdot\text{cm}^2$  (avec une surface de contact de  $4\mu\text{m}^2$ ). Avec l'aide de la couche auto-alignée de siliciure de titane, la résistivité spécifique de contact du système Cr/Au et poly-Si MILC est seulement légèrement plus grande que celle du système traditionnel Al: Si et poly-Si MILC.

La configuration de mesure statique est illustrée dans la Figure 6. La puce fabriquée est liée par fil sur une carte PCB. Cette dernière est ensuite collée sur un support métallique et fixé sur une platine exempt de vibrations. Un tribo-indenteur contrôlé par ordinateur est utilisé pour appliquer un point de charge au centre du diaphragme de détection. Un pont de Wheatstone, composé de deux résistances de détection et deux de référence, respectivement sur et hors de la membrane, est utilisé pour mesurer la réponse statique à la force dans le diaphragme. Avec une polarisation DC d'entrée, la tension en sortie est mesurée et enregistrée en utilisant un analyseur de paramètre du semiconducteur HP 4155. Pour le diaphragme de  $115\times 115\mu\text{m}^2$  carré, qui est fabriqué par la technique de micro-usinage de surface, avec une polarisation DC de 2V, une réponse statique d'environ  $0.4\mu\text{V}/\text{V}/\text{Pa}$  est mesurée. Et pour le diaphragme de  $210\times 210\mu\text{m}^2$  carré, qui est fabriqué par la technique de micro-usinage de volume, avec une polarisation DC de 3V, une réponse statique d'environ  $0,28\mu\text{V}/\text{V}/\text{Pa}$  est mesurée.

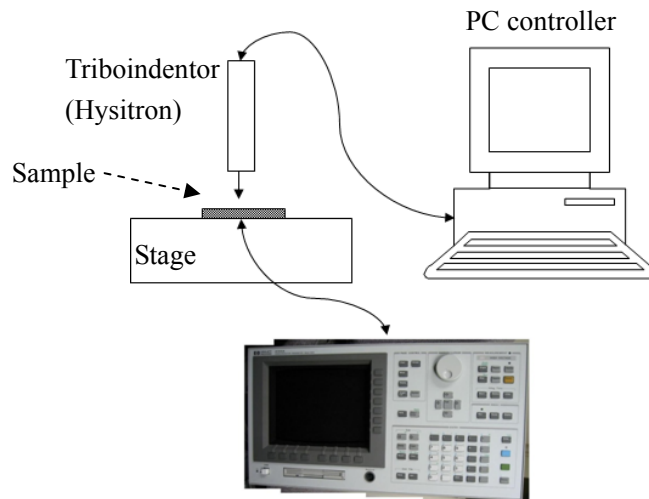


Figure 6: Configuration de la mesure statique.

La réponse dynamique du microphone est mesurée par une source acoustique l'onde N. La méthode la plus courante de génération de l'onde N est la stimulation d'une étincelle électrique à haute tension. Un circuit simple de décharge d'étincelle est illustré dans la Figure 7. Une alimentation à haute tension ( $\sim 14\text{kV}$ ) charge un condensateur de stockage ( $1\text{nF}$ ) à travers une résistance de limitation de courant ( $50\text{M}\Omega$ ), et la décharge du condensateur se produit à travers l'espace de décharge ( $\sim 1,3\text{cm}$ ).

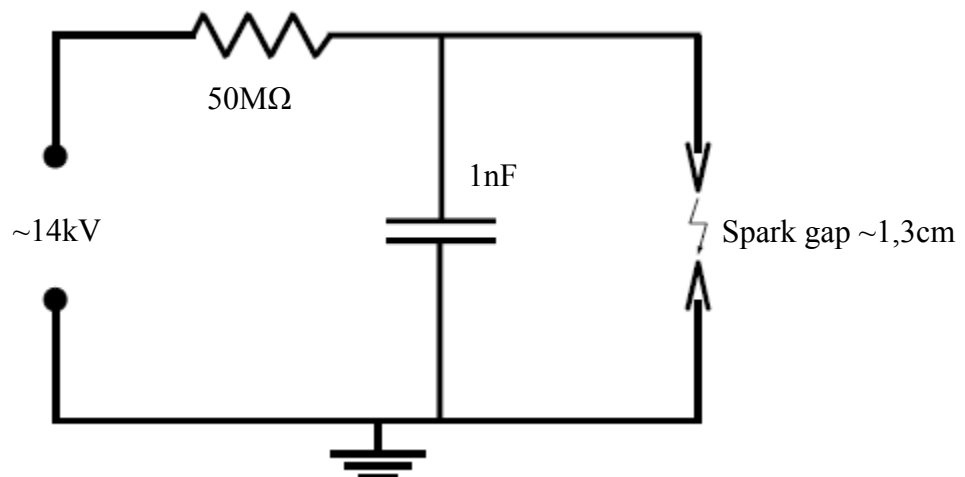


Figure 7: Schéma du condensateur de décharge à haute tension.

Comme nous l'avons trouvé dans la mesure statique de nano-indentation, la sensibilité de l'échantillon est très faible. Ainsi, une carte d'amplification est rajoutée à la sortie du capteur pour augmenter le signal et le rendre suffisamment grand pour être capturé par l'oscilloscope.

Après avoir découvert l'exacte forme de l'onde N à une distance  $r_0$  de la source d'étincelle, nos échantillons à calibrer sont placés à cette même distance. Un signal typique de l'onde N mesuré sur les dispositifs de micro-usinage de surface est présenté dans la Figure 8. Sur la figure, on peut clairement identifier deux signaux consécutifs d'oscillation. La première oscillation correspond à la forte hausse du choc d'avant de l'onde N et la seconde oscillation correspond à la forte hausse du choc d'arrière de l'onde N. Toutefois, les informations de basse fréquence de l'onde N, correspondant à la pente de l'avant vers l'arrière du choc ne sont pas visibles dans la courbe mesurée. Cela permet aussi de vérifier la perte d'information à basse fréquence dû à l'effet de court-circuit acoustique qui est prévu dans la modélisation par éléments finis.

La réponse en fréquence du microphone calibré est présentée dans la Figure 9, qui est également comparée avec le résultat FEA. Le pic de résonance est d'environ 400kHz, qui est égal à la prédiction du résultat FEA. La bande plate est très étroite, à peu près de 100kHz à 200kHz et au-dessous de 100kHz, la réponse en fréquence est rapidement diminuée. La sensibilité dynamique à l'intérieur de la bande plate est  $0,033\mu\text{V/V/Pa}$ , qui est bien plus faible que la valeur statique ( $0,4\mu\text{V/V/Pa}$ ). Ce phénomène peut aussi s'expliquer par l'effet de court-circuit acoustique. Même si on peut trouver exactement la pression incidente  $P_0$  au diaphragme, la différence réelle de pression  $\Delta p$  sur le diaphragme de détection est égale à  $P_0 - P_s$  ( $P_s$  est la pression de fuite dans la cavité d'air à travers les trous / fentes de relaxation), qui est difficile à prévoir.

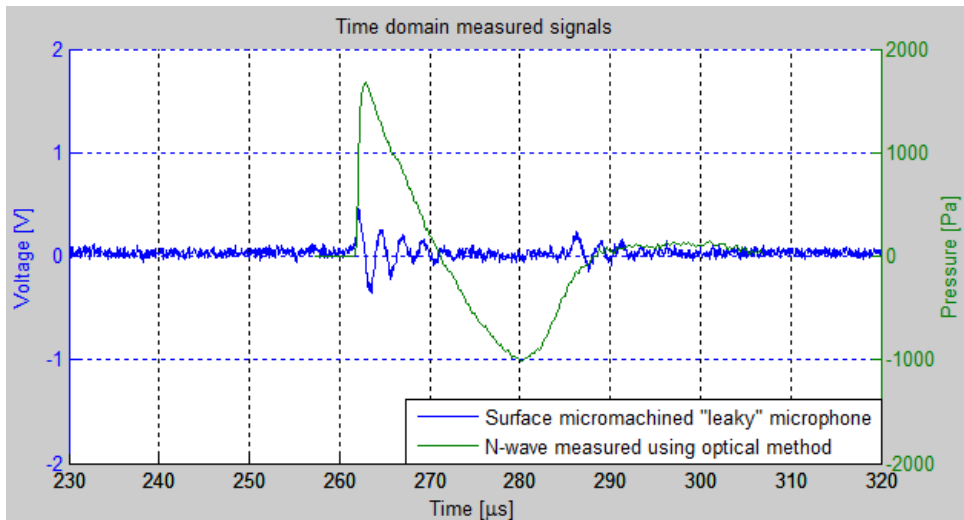


Figure 8: Résultat typique d'une mesure à étincelle d'un échantillon de microphone fabriqué par la technique de micro-usinage de surface (Polarisation DC 3V, avec le gain d'amplification à 1000 et la distance entre la source et le microphone à 10cm).

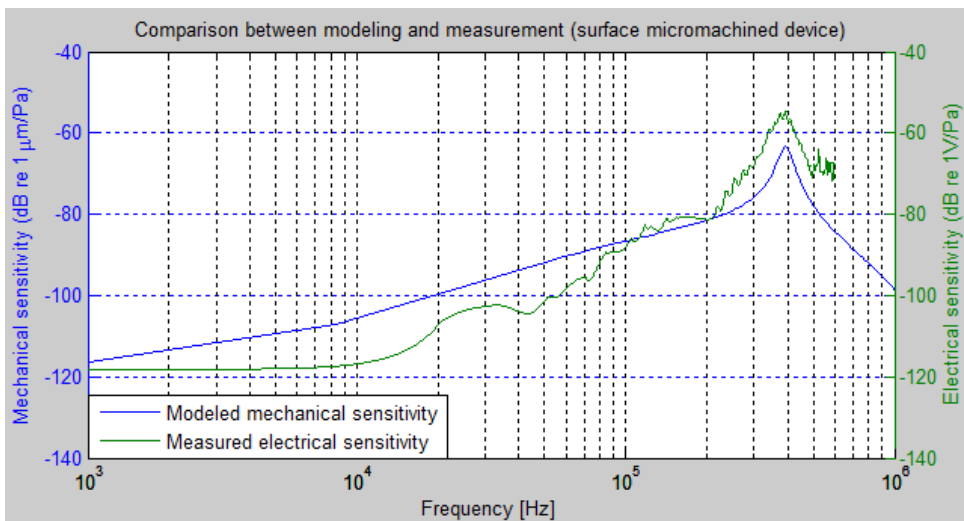


Figure 9: La réponse en fréquence du microphone calibré (Polarisation DC 3V, avec le gain d'amplification à 1000 et le signal en moyenne), en comparaison avec le résultat du FEA.

La Figure 10 montre le signal typique d'onde N mesuré en utilisant les dispositifs de micro-usinage de volume. D'après la Figure 11, il est montré que les dispositifs micro-usinés en volume ont une fréquence de résonance plus haute (715kHz) et dans la Figure 10, on peut voir que non seulement les informations à haute fréquence, mais aussi les informations à basse fréquence peuvent être prises par ce dispositif. En outre, nous pouvons constater qu'il y a une oscillation superposée sur la pente, ce qui signifie que le dispositif microphone n'est pas suffisamment amorti à sa fréquence de résonance.

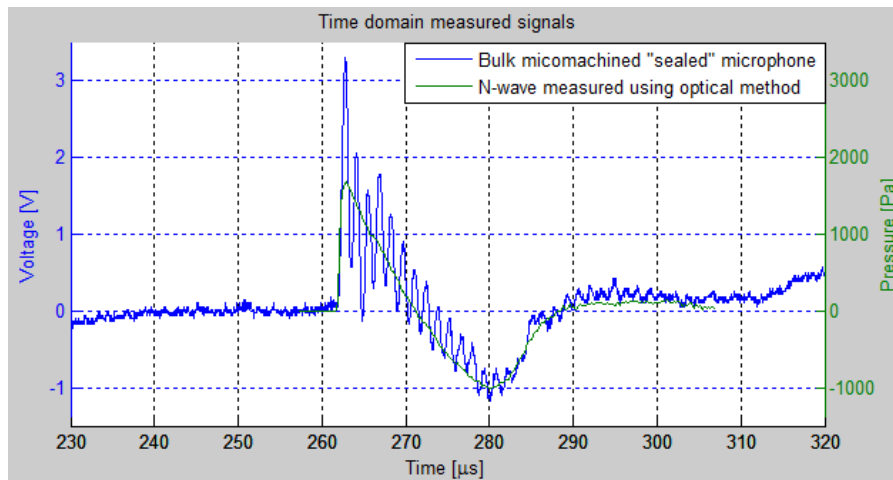


Figure 10: Résultat typique d'une mesure à étincelle d'un échantillon de microphone fabriqué par la technique de micro-usinage de volume (Polarisation DC 3V, avec le gain d'amplification à 1000 et la distance entre la source et le microphone à 10cm).

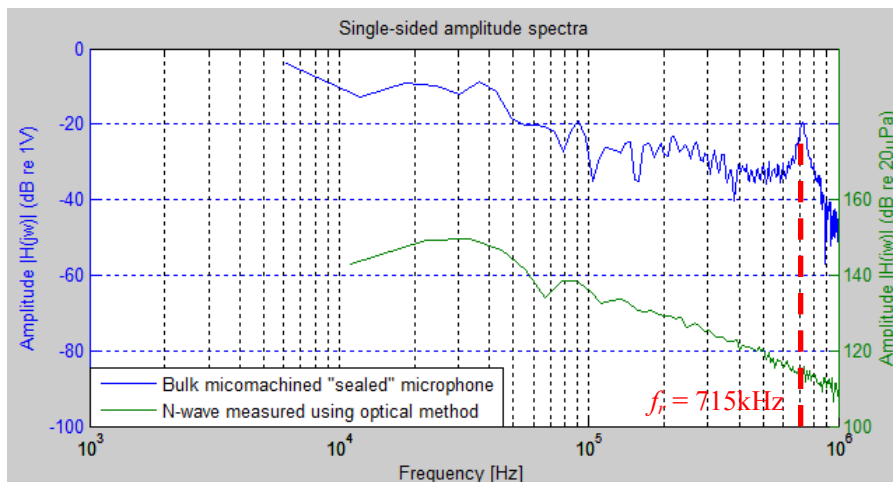


Figure 11: Spectre d'amplitude du FFT unilatéral des signaux mesurés par un microphone micro-usiné en volume et par la méthode optique.

La réponse en fréquence des dispositifs de micro-usinage de volume est présentée dans la Figure 12, qui est comparé avec le résultat de modélisation par éléments concentrés. La sensibilité dynamique est 1mV/Pa (avec un gain d'amplification de 1000 et une polarisation DC de 3V), ce qui signifie que la sensibilité dynamique réelle du microphone est d'environ 0,33μV/V/Pa et similaire à la sensibilité statique calibrée (0,28μV/V/Pa) . En outre, ce microphone présente une bande passante large et plate de 6kHz à 500kHz.

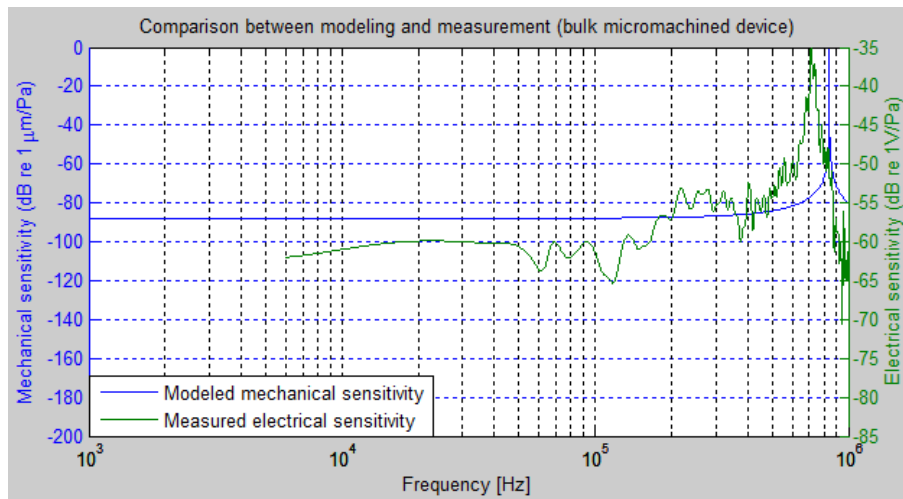


Figure 12: La réponse en fréquence du microphone calibré (Polarisation DC 3V, avec le gain d'amplification de 1000 et le signal en moyenne), en comparaison avec le résultat de modélisation par éléments concentrés.

Enfin, trois capteurs micro-usinés en volume sont placés dans un plan pour former un réseau qui démontre son l'application comme un localisateur sonore (Figure 13). Le premier capteur ( $M_1$ ) présente une coordonnée de  $x_1 = 2,5$ ,  $y_1 = 0$  et  $z_1 = 0$ ; le deuxième capteur ( $M_2$ ) présente une coordonnée de  $x_2 = -2,5$ ,  $y_2 = 0$  et  $z_2 = 0$  et le troisième capteur ( $M_3$ ) présente une coordonnée de  $x_3 = 0$ ,  $y_3 = 4$  et  $z_3 = 0$ , avec toutes les unités en centimètre.

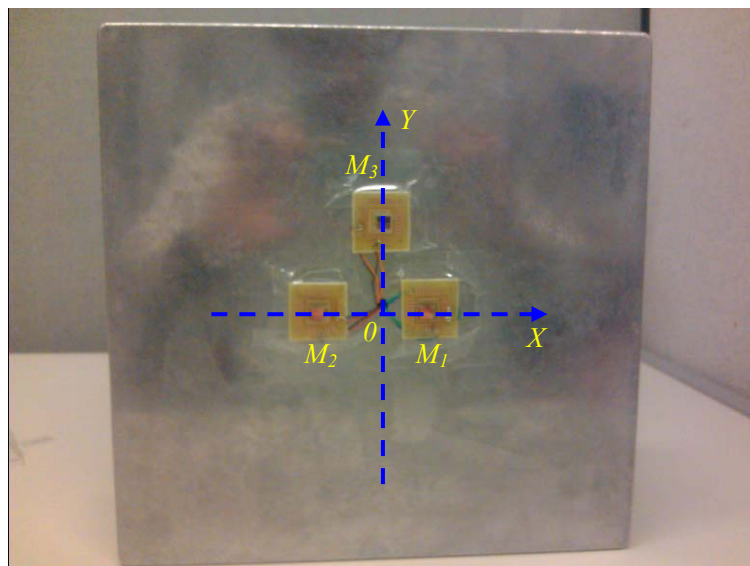


Figure 13: Coordonnées du réseau de capteurs.

La Figure 14 présente la configuration de l'application de localisation de la source sonore. Le générateur d'étincelles émet l'onde acoustique, qui est détectée par le réseau de capteurs. Les signaux détectés sont capturés par un oscilloscope (Tektronix TDS 2024C), puis les signaux

capturés sont transférés à un ordinateur portable via un câble USB en utilisant le MATLAB Instrument Control Toolbox, qui est basé sur le standard NI-VISA de National Instruments. Ensuite les temps de délai et les coordonnées de source acoustique sont calculés par le logiciel MATLAB. Toutes ces fonctions sont réalisées par une interface utilisateur graphique (GUI) personnalisée sous MATLAB.

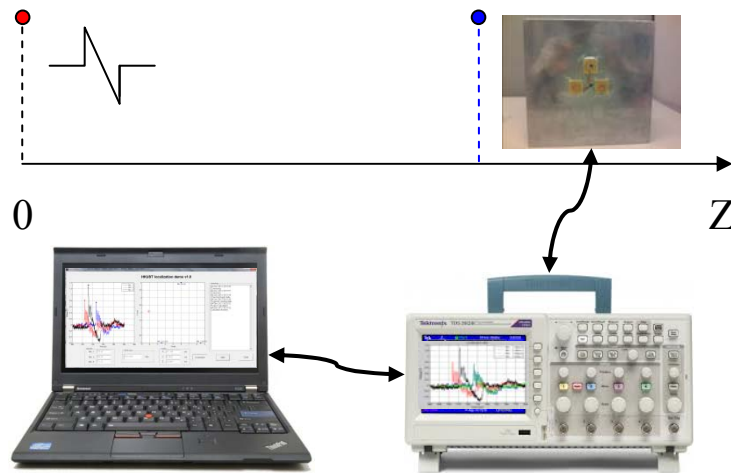


Figure 14: La configuration du système de localisation de la source acoustique.

La source sonore d'étincelle est préréglée aux coordonnées ( $x_s = 0\text{cm}$ ,  $y_s = 4\text{cm}$ ) dans le plan  $XY$ . Etant donné que les deux aiguilles d'étincelle ont un écart de 1,3 cm entre eux, la position médiane entre les aiguilles est supposée être la position de la source (Figure 15). La distance entre la source sonore et le réseau de capteurs en coordonnée  $Z$  varie de 10cm à 105cm (la distance est mesurée par une règle). À chaque position, 20 mesures sont effectuées. En utilisant les temps de délai mesurés et la vitesse du son calibré, les coordonnées de la source sonore sont calculées et comparées avec les valeurs qui ont été mesurées au préalable par la règle (Figure 16).

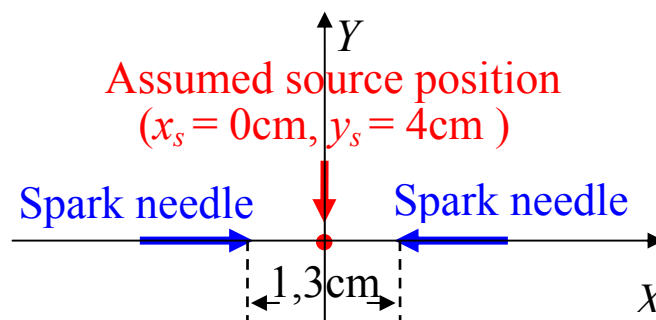
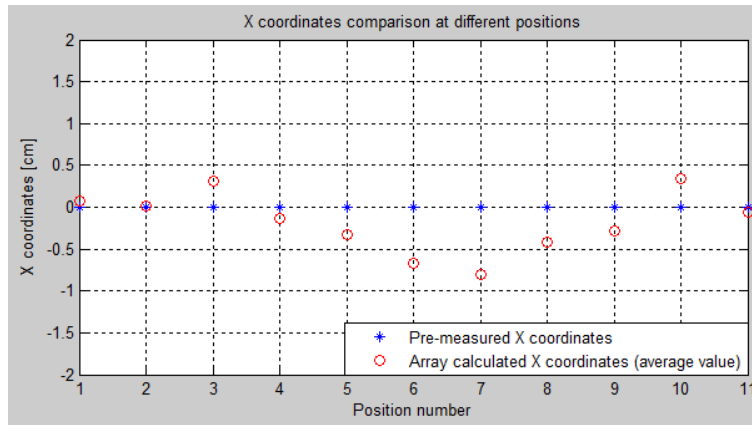
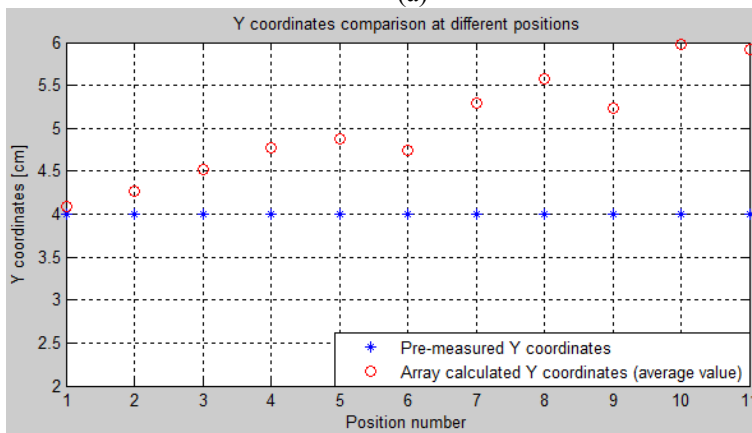


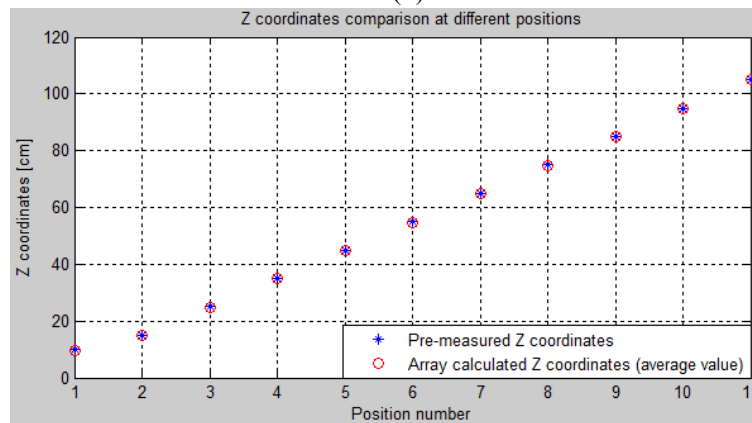
Figure 15: Définition de la position de la source sonore.



(a)



(b)



(c)

Figure 16: Les comparaisons de coordonnées entre les valeurs pré-mesurées et les valeurs calculées sur (a) les coordonnées  $X$  ; (b) les coordonnées  $Y$  ; (c) les coordonnées  $Z$ .

D'après la Figure 16, il est montré que les valeurs pré-mesurées et les valeurs calculées des coordonnées  $Z$  correspondent très bien, contrairement aux coordonnées  $X$  et  $Y$ . Pour les coordonnées  $X$  (Figure 16 (a)), les valeurs calculées fluctuent autour des valeurs pré-mesurées. Ce phénomène peut être expliqué par le fait que le point réel de génération d'étincelle n'est



pas toujours au milieu des deux aiguilles. Au contraire, ce point oscille au cours de l'expérience aux différentes positions. Pour vérifier cette hypothèse, une caméra à haute vitesse est nécessaire pour capturer les images d'étincelle lors des mesures pour l'analyse de position, ce qui n'est pas applicable au stade actuel.

Pour les coordonnées  $Y$  (Figure 16 (b)), les différences entre les valeurs pré-mesurées et les valeurs calculées augmentent linéairement jusqu'à 2cm lorsque la position de mesure passe de 1 à 11 (dans la figure 16 (c), cela signifie que la coordonnée  $Z$  varie de 10cm à 105cm). Les différences entre les valeurs pré-mesurées et les valeurs calculées des coordonnées  $Y$  peuvent s'expliquer par la dénivellation de la surface du sol. L'angle  $\theta$  entre la surface du sol et le niveau est calculé à  $1,1^\circ$ .

Bien que les deux prototypes de microphone large-bande à haute fréquence sont fabriqués avec succès et calibrés, il y a plusieurs sujets à résoudre en avenir. Tout d'abord, les modèles de ces deux microphones sont tous basés sur la méthode FEA. Un modèle analytique, qui n'est pas très précis mais pourrait estimer rapidement la performance des différentes structures, est bien nécessaire. D'autre part, concernant le microphone fabriqué par la technique de micro-usinage de volume, en raison de la grande cavité sous le diaphragme de détection, il n'y a pas d'amortissement suffisant pour amortir le critique pic de résonance. Dans le futur, une nouvelle structure avec un amortisseur intégré utilisant le l'effet d'amortissement du film de compression doit être explorée. Troisièmement, lors de nos tests, l'amplificateur est réalisé par les composant discrets sur le PCB et relié au capteur par wire bonding. Afin d'atténuer le bruit et d'améliorer la performance d'amplification, l'amplificateur doit être fabriqué sur la même puce que le capteur, et, éventuellement, le capteur et l'amplificateur peuvent être fabriqués sur le même substrat.



---

## **Titre**

# **Microcapteurs de Hautes Fréquences pour des Mesures en Aéroacoustique**

## **Résumé**

L'aéroacoustique est une filière de l'acoustique qui étudie la génération de bruit par un mouvement fluide turbulent ou par les forces aérodynamiques qui interagissent avec les surfaces. Ce secteur en pleine croissance a attiré des intérêts récents en raison de l'évolution de la transportation aérienne, terrestre et spatiale. Les microphones avec une bande passante de plusieurs centaines de kHz et une plage dynamique couvrant de 40Pa à 4 kPa sont nécessaires pour les mesures aéroacoustiques. Dans cette thèse, deux microphones MEMS de type piézorésistif à base de silicium polycristallin (poly-Si) latéralement cristallisé par l'induction métallique (MILC) sont conçus et fabriqués en utilisant respectivement les techniques de microfabrication de surface et de volume. Ces microphones sont calibrés à l'aide d'une source d'onde de choc (N-wave) générée par une étincelle électrique. Pour l'échantillon fabriqué par le micro-usinage de surface, la sensibilité statique mesurée est  $0.4\mu\text{V/V/Pa}$ , la sensibilité dynamique est  $0.033\mu\text{V/V/Pa}$  et la plage fréquentielle couvre à partir de 100 kHz avec une fréquence du premier mode de résonance à 400kHz. Pour l'échantillon fabriqué par le micro-usinage de volume, la sensibilité statique mesurée est  $0.28\mu\text{V/V/Pa}$ , la sensibilité dynamique est  $0.33\mu\text{V/V/Pa}$  et la plage fréquentielle couvre à partir de 6 kHz avec une fréquence du premier mode de résonance à 715kHz.

## **Mots-Clés:**

Aero-acoustic, Bulk micro-machining, DRIE, MEMS, Microphone, MILC, Wide-band.

---

## **Title**

# **High Frequency MEMS Sensor for Aero-acoustic Measurements**

## **Abstract**

Aero-acoustics, a branch of acoustics which studies noise generation via either turbulent fluid motion or aerodynamic forces interacting with surfaces, is a growing area and has received fresh emphasis due to advances in air, ground and space transportation. Microphones with a bandwidth of several hundreds of kHz and a dynamic range covering 40Pa to 4kPa are needed for aero-acoustic measurements. In this thesis, two metal-induced-lateral-crystallized (MILC) polycrystalline silicon (poly-Si) based piezoresistive type MEMS microphones are designed and fabricated using surface micromachining and bulk micromachining techniques, respectively. These microphones are calibrated using an electrical spark generated shockwave (N-wave) source. For the surface micromachined sample, the measured static sensitivity is  $0.4\mu\text{V/V/Pa}$ , dynamic sensitivity is  $0.033\mu\text{V/V/Pa}$  and the frequency range starts from 100kHz with a first mode resonant frequency of 400kHz. For the bulk micromachined sample, the measured static sensitivity is  $0.28\mu\text{V/V/Pa}$ , dynamic sensitivity is  $0.33\mu\text{V/V/Pa}$  and the frequency range starts from 6kHz with a first mode resonant frequency of 715kHz.

## **Keywords:**

Aero-acoustic, Bulk micro-machining, DRIE, MEMS, Microphone, MILC, Wide-band.

---

**Laboratoire TIMA – 46 avenue Félix Viallet 38000 Grenoble, France**

**ISBN: 978-2-11-129173-7**

---